# Effects of Doping in Photovoltaic Organic Semiconductor Films

2015

Yusuke Shinmura

# Contents

# Chapter 1:

# General Introduction

## 1.1. Background

Impurity doping is an indispensable technique for present inorganic semiconductor devices.[1)] With this technique the position of the Fermi level and the conduction type of the semiconductor can be controlled. Semiconductors that have higher hole than electron concentration are described as *p*-type semiconductors. Conversely, semiconductors which have higher electron concentration are described as *n*-type semiconductors. By bringing *p*- and *n*-type semiconductors into contact with each other various electronic devices can be created. Solar cells, which generate electrical power, operate by separating the carriers in a pn-junction.[2-6)] Light emitting diodes, which rely on carrier recombination in a *pn*-junction, can emit light of various wavelengths depending on the type of semiconductor.[7-9)] Bipolar field-effect transistors used as electronic switches consist of *npn* or *pnp* junctions.[2)]

The fabrication techniques for these devices were well established during the 20th century. These devices are widely prevalent and are an essential part of our everyday lives. Thus, impurity doping currently plays a significant role in the electronics industry.

On the other hand, organic electronic devices, i.e., devices consisting of organic semiconductors, have attracted much attention during the 21st century. Compared to inorganic semiconductors, organic semiconductors have some advantages in that the device fabrication is easy, the production costs low, and they are flexible, lightweight and easy to design.

Since Inokuchi et al. reported on the high conductivity of the perylene-bromine complex in 1954[10], studies on organic semiconductor have advanced. However, organic semiconductors have fallen far behind inorganic semiconductors in terms of device applications. In groundbreaking work in the late 1980s, Tang reported on organic solar cells (OSCs)[11] and organic light emitting diodes (OLEDs).[12] While the practical use of OLEDs for display and lighting panels has been extensive, OSCs are still in the research phase. As is the case for inorganic semiconductors, further development of organic electronics requires precise *pn*-control in organic semiconductors. In particular, *pn*-control in OSCs has the potential to obtain high photo-conversion efficiencies comparable to inorganic solar cells. Thus, the author has focused on the effects of doping in organic semiconductors for solar cell application.

## 1.2. Impurity Doping

### *1.2.1. Doping of Inorganic Semiconductors*

Impurity doping of inorganic semiconductors is a well-established technique. Impurities are introduced into the lattice of an inorganic semiconductor by diffusion or ion implantation. The mechanisms for doping Si are shown in Fig. 1.1. Doping Si, which has four valence electrons, with boron (B), which has three valence electrons, induces the B atom to accept an electron from Si lattice creating a hole that orbits the ionized acceptor ($B^-$) via a weak Coulomb attraction, which can dissociate easily and move freely due to the thermal energy at room temperature (Fig. 1.1(a)). Thus, acceptor doping increases the hole concentration and changes the semiconductor to *p*-type. Donor doping can be described similarly (Fig. 1.1(b)). Doping with

phosphorus (P), which has five valence electrons, gives an excess electron that is not required for bonding. This excess electron orbits the ionized donor ($P^+$), but can dissociate easily and move freely. Thus, donor doping increases the electron concentration and changes the semiconductor to *n*-type. This *pn*-control gives flexibility in designing the energy structure of various electronics devices.

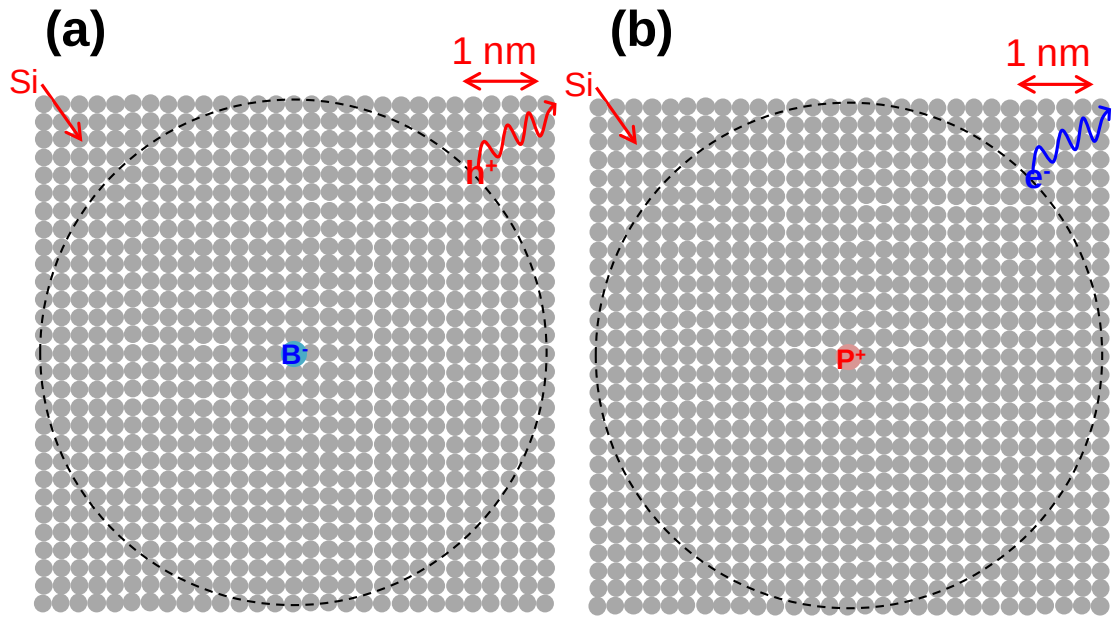


Fig. 1.1 Schematic illustrations of (a) *p*-type and (b) *n*-type silicon. The gray, blue and red circles indicate silicon atoms, a negatively charged boron atom and a positively charged phosphorus atom, respectively.

### *1.2.2. Doping of Organic Semiconductors*

The principle of doping organic semiconductors is shown in Fig. 1.2. The highest occupied molecular orbital (HOMO) of the donor dopant needs to be located at a significantly shallow position, so that the donor dopants can supply electrons to the lowest unoccupied molecular orbital (LUMO) of the host material. In contrast, the

LUMO of the acceptor dopant needs to be located at a deep position, so that the acceptor dopants can extract an electron from the HOMO of the host material. Thus, charge transfer between the host semiconductor and the dopant is induced by the difference in energy levels between them.

The *pn*-control of $C_{60}$ film based on charge transfer has been reported.[13-15] Fig. 1.3 shows an energy diagram of a doped $C_{60}$ film. The Fermi level ($E_F$) of the $C_{60}$ film doped with $Cs_2CO_3$ has shifted toward the LUMO and reached 4.40 eV compared to 4.60 eV for the undoped film, which indicates that the $C_{60}$ has become *n*-type. On the other hand, $E_F$ in the $C_{60}$ film doped with $MoO_3$ has shifted toward the HOMO and reached 5.88 eV, indicating that the $C_{60}$ has become *p*-type. While $C_{60}$ is generally used as *n*-type material, doping can change the conduction type from *n*- to *p*-type. Control of the conduction type offers more flexibility in designing the energy band structure. On the other hand, metal-free phthalocyanine ($H_2Pc$) is a typical *p*-type material. Whether or not it is possible to change the conduction type of $H_2Pc$ is a fascinating question. Thus, the author examined the doping of $H_2Pc$ and reports on the results in this thesis (see chapter 3).

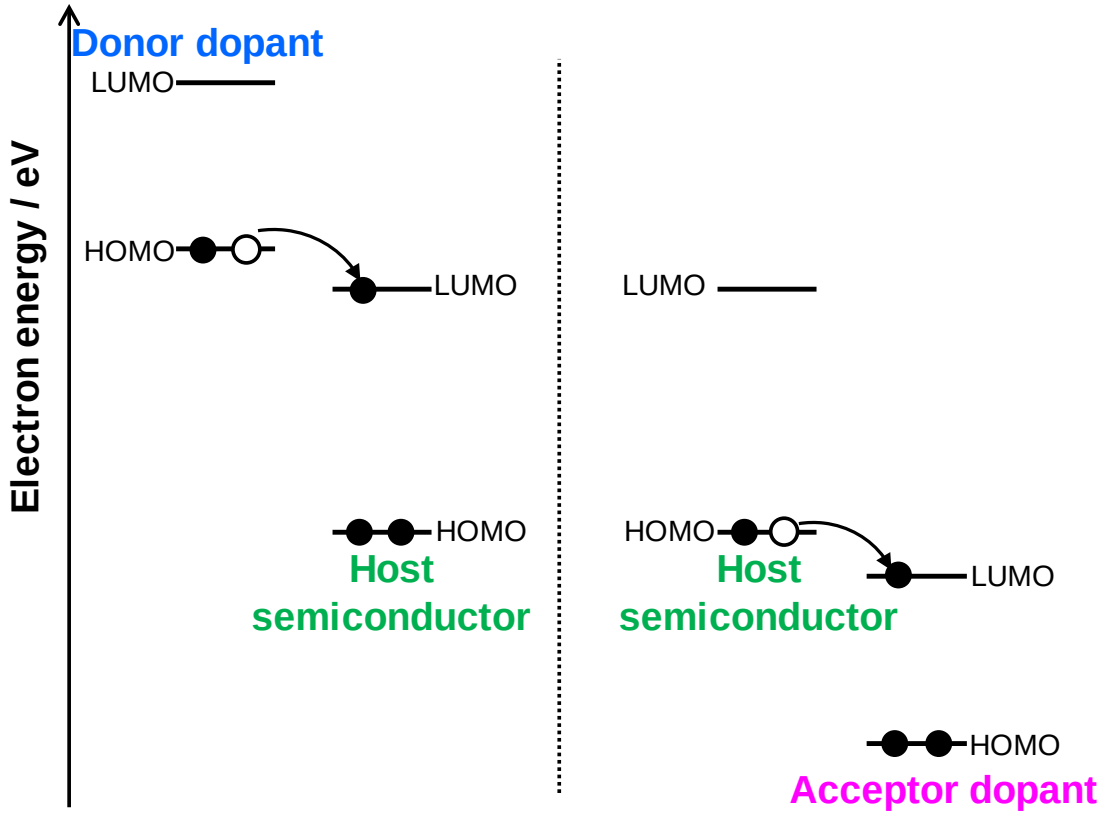


Fig. 1.2 Schematic diagrams of *n*-type (left) and *p*-type (right) doping of organic semiconductors.

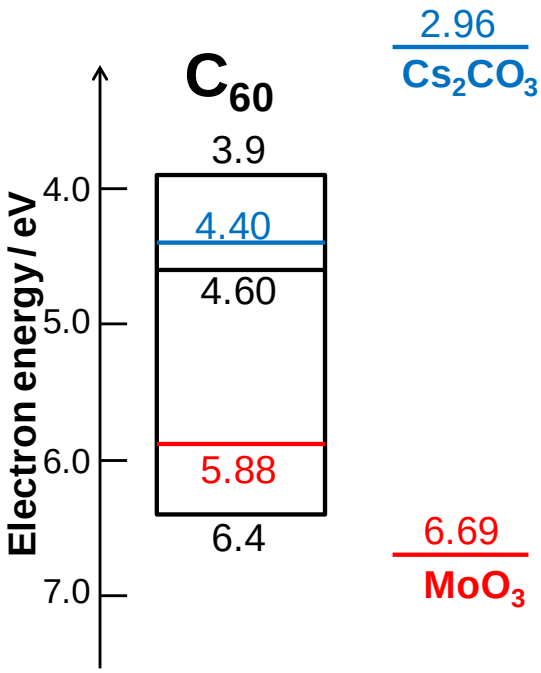


Fig. 1.3 Energy diagram of doped $C_{60}$. The black, red and blue lines indicate the energy levels of $E_F$ for non-doped, $MoO_3$-doped, and $Cs_2CO_3$-doped films, respectively. The work functions of $Cs_2CO_3$ and $MoO_3$ are also shown. The doping concentration is 3,000 ppm.

Host organic semiconductors and dopants form charge-transfer (CT) complexes. Kubo et al. described the formation of some CT complexes, i.e., $C_{60}^{+}$---$MoO_3^{-}$[13] and $C_{60}^{-}$---$Cs_2CO_3^{+}$[14,15] (Fig. 1.4). $MoO_3$ can extract an electron from the valence band of $C_{60}$ owing to its extremely high work function. In contrast, $Cs_2CO_3$ can donate an electron to the conduction band of $C_{60}$ owing to its low work function. A film of $C_{60}$ with mixed dopants changed color and showed CT absorption. Unlike the doping of inorganic semiconductors, dopants are not incorporated into the lattice of the host semiconductor.

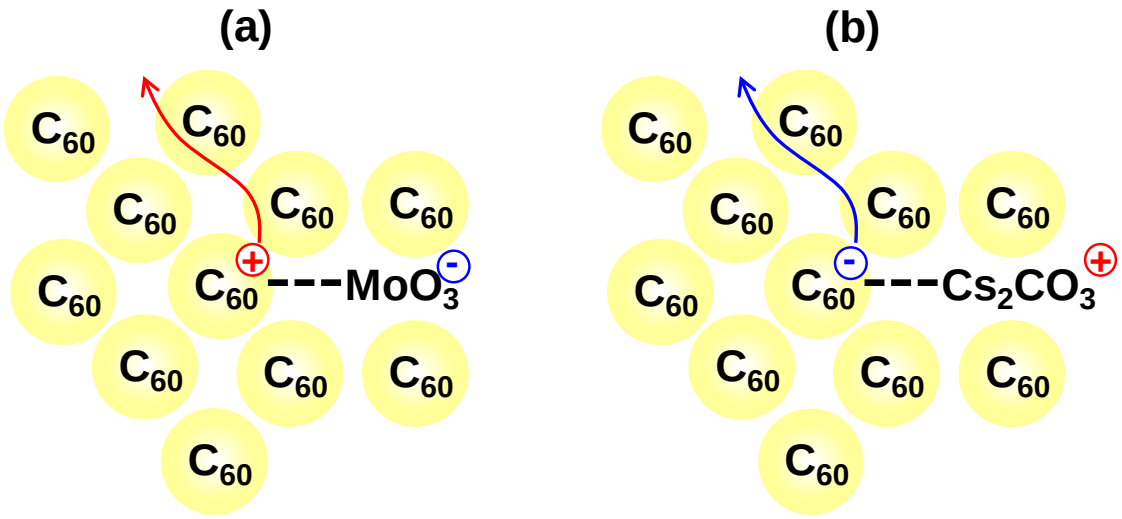


Fig. 1.4 Mechanisms of (a) $MoO_3$ and (b) $Cs_2CO_3$ doping of $C_{60}$.

### *1.2.3. Dopants for Organic Semiconductors*

Fig. 1.5 summarizes the various donor and acceptor dopants for organic semiconductors. The introduction of halogen gases such as bromine[16] and iodine[17,18] into organic semiconductors for *p*-type doping has been performed. However, these small molecule gases diffuse easily in organic semiconductors, making precise control of the doping by halogen gases quite difficult. So, larger molecules are desirable to prevent diffusion. Some acceptor molecules have been reported. In 1960, Kearns et al. reported an increase by a factor of $10^7$ of the dark conductivity in metal-free phthalocyanine by the addition of ortho-chloranil.[19] Maitrot et al. reported a drastic increase in conductivity by *p*-type doping with 2,3-dichloro-5,6-dicyano-1,4-benzoquinone (DDQ) and tetracyanoquinodimethane (TCNQ).[20] Schottky diode fabrication using DDQ doped oligothiophene has also been reported.[21] The Leo group have done systematic studies using

tetrafluoro-tetracyano-quinodimethane ($F_4$-TCNQ) for OSCs and OLEDs.[22,23] Metal oxides, i.e., molybdenum oxide ($MoO_3$)[13,14,24,25] and vanadium oxide ($V_2O_5$),[26] which have been used as hole injection layers for OLEDs are used as acceptor dopants. Antimony pentachloride ($SbCl_5$) and iron (III) chloride ($FeCl_3$)[27] also have strong electron acceptability attributed to their high work function.

On the other hand, *n*-type doping is more difficult because of the instability of donor dopants with respect to oxygen. Exposure to oxygen must be prevented in order to perform *n*-type doping since oxygen works as an acceptor. Conventionally, alkali metals such as sodium, potassium, lithium, cesium, or strontium have been used.[28-30] However, undesirable diffusion into organic films complicates precise fabrication of devices. Moreover, metal atoms work as recombination centers, which can have a considerable detrimental impact on the device characteristics. Doping with electron-donating organic molecules has also been reported. Bis(ethylenedithio)-tetrathiafulvalene (BEDT-TTF) doping of naphthalenetetracarboxylic dianhydride (NTCDA) shows an increase in conductivity and a negative $E_F$ shift.[31] A UPS study of n-type doping with tetrathianaphthacene (TTN) has been reported.[32] Furthermore, various other acceptor dopants such as cationic salts[33-36], and transition metal complexes including Ru[37], Co[38,39], Cr[40], and W[40-42] have also been reported. Air-stable cesium carbonate ($Cs_2CO_3$),[15,43-45] which is often used as an electron extracting layer,[46] is one of the most appealing acceptor dopants.

In this thesis, the author used $MoO_3$, $FeCl_3$ and $Cs_2CO_3$ because of their strong electron acceptor and donor qualities and their ease of handling.

**(a)**

Halogen gases: $Br_2$, $I_2$

Metal oxides: $MoO_3$, $V_2O_5$, $WO_3$

$SbCl_5$, $FeCl_3$

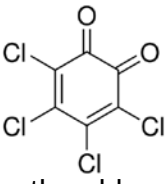

ortho-chloranil

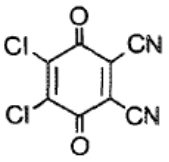

DDQ

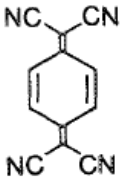

TCNQ

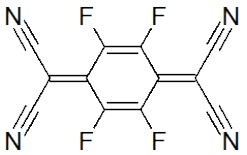

$F_4$-TCNQ

**(b)**

Alkali metals: K, Na, Li, Cs, Sr

$Cs_2CO_3$

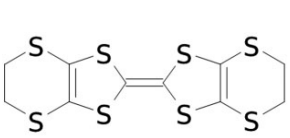

BEDT-TTF

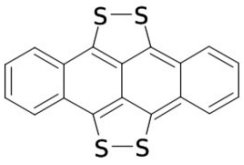

TTN

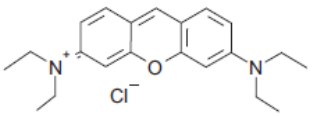

Pyronin B chloride

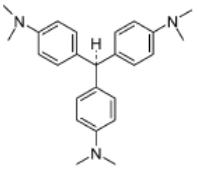

Leuco Crystal Violet

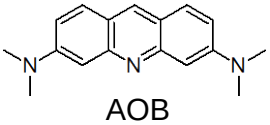

AOB

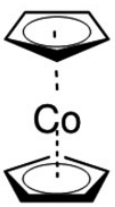

$CoCp_2$

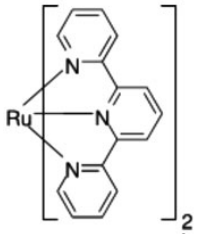

$[Ru(terpy)_2]^0$

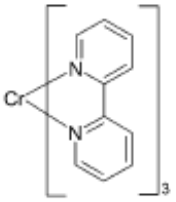

$[Cr(bpy)_3]^0$

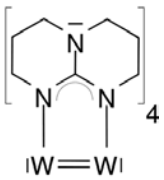

$W_2(hpp)_4$

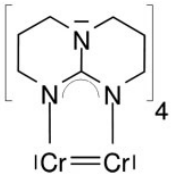

$Cr_2(hpp)_4$

Fig. 1.5 (a) Acceptor and (b) donor dopants for organic semiconductors.

## 1.3. Carrier Concentration in Doped Semiconductors

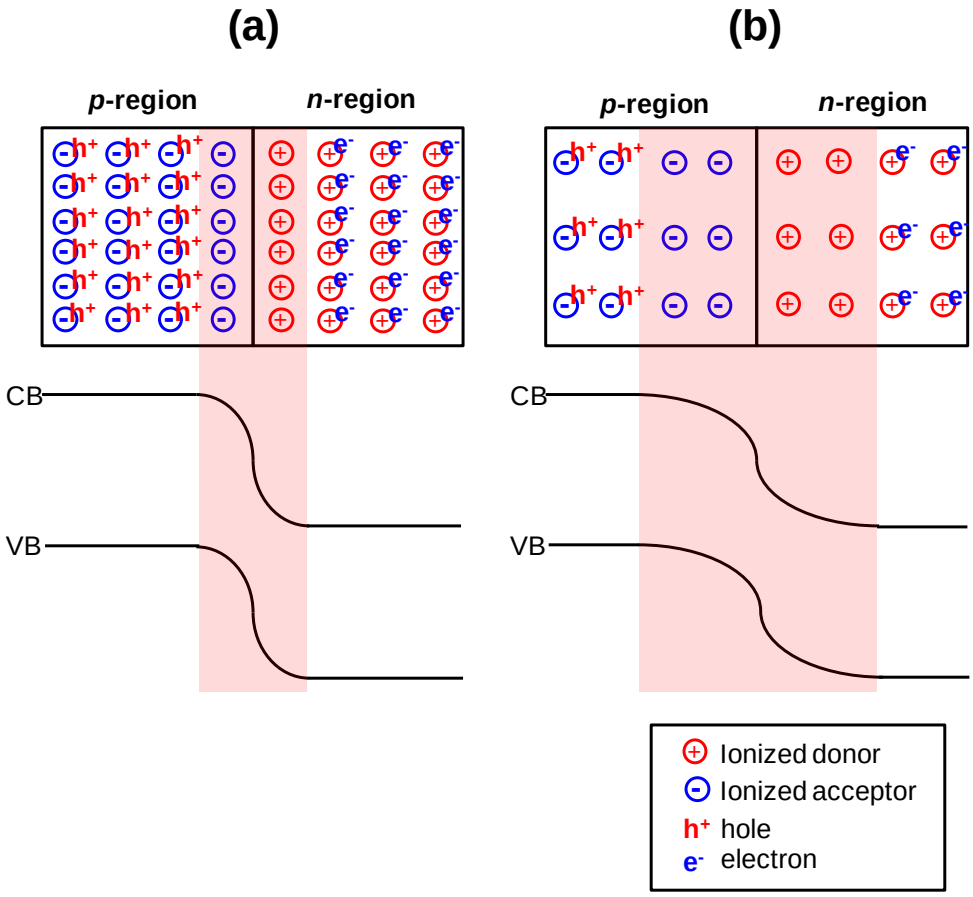


Fig. 1.6 Schematic illustrations of space charge distributions (upper) and energy band structures (bottom) in the case of (a) high and (b) low doping concentrations. The red shaded parts indicate depletion regions.

Understanding the energy structure of doped organic semiconductors is indispensable for designing devices. In particular, the depletion layer width ($W_{dep}$) is an important factor. Schematic illustrations of the space charge distributions and energy band structures in *pn*-junctions are shown in Fig. 1.6. With the *p*- and *n*-layers in contact, holes in the *p*-layer diffuse into the *n*-layer due to the hole density gradient. Conversely, electrons in the *n*-layer diffuse into the p-layer. A depletion layer is

formed by recombination of the diffused holes and electrons at the interface between the *p*- and *n*-layers. $W_{dep}$ is determined by the carrier concentration. In the case of high doping concentration, the change in potential at the *pn*-junction is large due to the combination of a large number of electrons and holes (Fig.1.6(a)). The large electric field formed in a narrow region limits the spread of $W_{dep}$. Conversely, $W_{dep}$ spreads widely in the case of low carrier concentration (Fig.1.6(b)). That is, as the doping concentration increases, $W_{dep}$ becomes narrower. Thus, there is a close relationship between $W_{dep}$ and carrier concentration. The relationship can be found using Poisson's equation.[2] The electrostatic potential ($\Psi$) is obtained from Poisson's equation,

$$\frac{d^2\Psi}{dx^2} \equiv -\frac{dE}{dx} = -\frac{\rho_s}{\varepsilon\varepsilon_0} = -\frac{e}{\varepsilon\varepsilon_0}(N_D - N_A + p - n)$$

where, $\rho_s$, $\varepsilon$, $\varepsilon_0$, $N_D$, $N_A$, p and n are the resistivity and relative permittivity of the semiconductor, the permittivity in vacuum, and the donor, acceptor, free hole and free electron concentrations, respectively.

Since there are no carriers in the depletion region, i.e., p=n=0, this equation reduces to

$$\frac{d^2\Psi}{dx^2} = \frac{e}{\varepsilon\varepsilon_0}(N_D - N_A) \qquad (1.2)$$

The space charge distribution for an abrupt junction is shown in Fig. 1.7. Poisson's equation can be simply expressed as,

$$\frac{d^2\Psi}{dx^2} = \frac{eN_A}{\varepsilon\varepsilon_0} \qquad (-x_p \le x < 0)$$

$$\frac{d^2\Psi}{dx^2} = \frac{eN_D}{\varepsilon\varepsilon_0} \qquad (0 < x \le x_n) \qquad (1.3)$$

Since the space charge of whole semiconductor is neutral, the negative charge in the *p*-region must equal the positive charge in the *n*-region. Thus,

$$N_A x_p = N_D x_n \qquad (1.4)$$

where, $x_p$ and $x_n$ are the widths of the depletion layer in the *p*- and *n*-regions, respectively.

The electric field intensity is obtained by integration of Eq. (1.3),

$$E(x) = \frac{d\Psi}{dx} = \frac{eN_A(x + x_p)}{\varepsilon\varepsilon_0} \qquad (-x_p \le x < 0)$$
$$E(x) = \frac{eN_D(x - x_n)}{\varepsilon\varepsilon_0} \qquad (0 < x \le x_n) \tag{1.5}$$

Integration of the electric field given by Eq (1.5) gives the built-in potential ($V_{bi}$). Thus, the area of the triangle in Fig. 1.7(b) indicates $V_{bi}$.

$$V(x) = -\frac{eN_D}{2\varepsilon\varepsilon_0}x_p^2 + \frac{eN_D}{\varepsilon\varepsilon_0}x_n^2 = \frac{1}{2}E_m W_{dep} \tag{1.6}$$

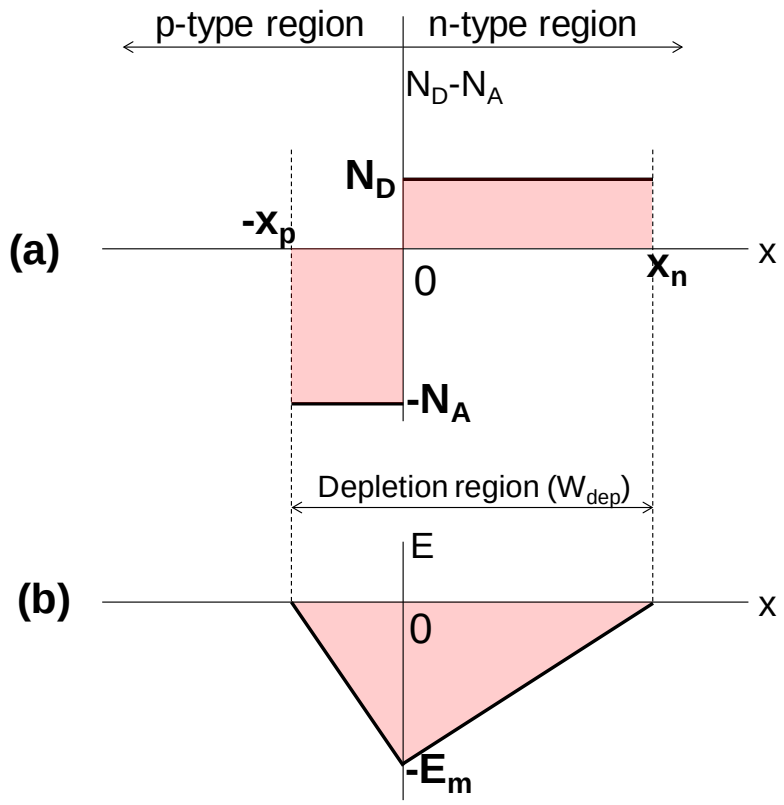


Fig. 1.7 (a) Space charge distribution in the depletion region in thermal equilibrium. (b) Electric field distribution of a *pn*-junction. The area of the red shaded triangle corresponds to $V_{bi}$.

From Eq. (1.4) and (1.6), $W_{dep}$ is obtained as a function of $V_{bi}$.

$$W_{dep} = \sqrt{\frac{2\varepsilon\varepsilon_0}{e}\left(\frac{N_A + N_D}{N_A N_D}\right)V_{bi}} \tag{1.7}$$

A junction in which the carrier concentration on one side is much higher than that on the other is called a one-sided abrupt junction. In the case of a heavily-concentrated *p*/low-concentrated n ($p^+n$) junction, that is, $N_A >> N_D$, $W_{dep}$ in the *p*-region is extremely narrow. Thus, $W_{dep}$ in the *n*-region can simply be expressed as follows.

$$W_{dep} \cong x_n = \sqrt{\frac{2\varepsilon\varepsilon_0 V_{bi}}{eN_D}} \tag{1.8}$$

Conversely, $W_{dep}$ in the *p*-region in the case of an $n^+p$ junction is expressed as

$$W_{dep} \cong x_p = \sqrt{\frac{2\varepsilon\varepsilon_0 V_{bi}}{eN_A}} \tag{1.9}$$

$W_{dep}$ of Schottky junctions can also be represented by Eqs. (1.8) and (1.9). Since $W_{dep}$ and $V_{bi}$ can be determined by band-mapping using a Kelvin probe, the carrier concentration can be calculated using these equations.

## 1.4. Kelvin Probe Measurement

### *1.4.1. Principle of Kelvin Vibrating Capacitor Method*

The $E_F$ in organic semiconductor films was determined using a Kelvin probe.[47-55] Figure 1.8 shows the mechanism of the Kelvin vibrating capacitor method. An organic semiconductor film facing a standard gold plate probe forms a capacitor due to the difference in work function. Varying the distance between them by vibrating the gold plate generates an alternating current (AC). The voltage at which the AC is cancelled corresponds to the contact potential difference (CPD). The $E_F$ of the sample films can be determined from the difference in CPD between the sample and a standard gold plate, the work function of which has been measured by atmospheric photoelectron spectroscopy.

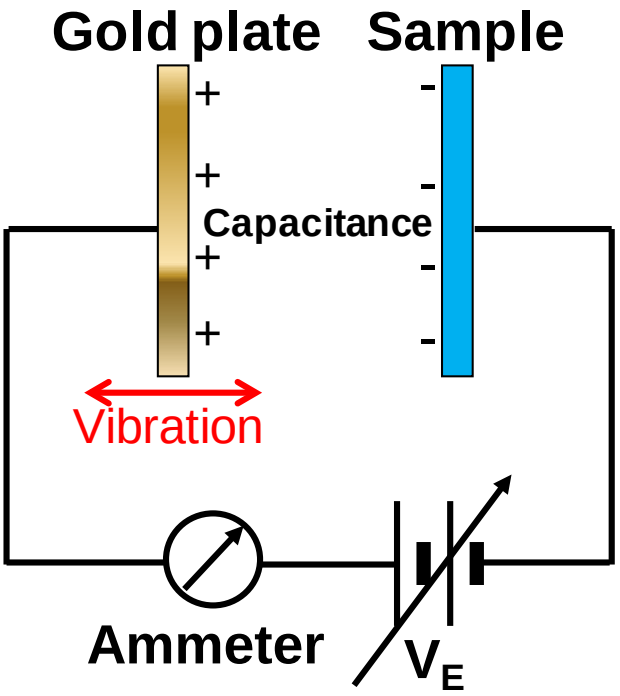


Fig. 1.8. the mechanism of Kelvin vibrating capacitor method

Studies on the energy structure of organic semiconductors have been performed not only by using a Kelvin probe but also by ultra-violet photoelectron spectroscopy (UPS), X-ray photoemission spectroscopy (XPS) and inverse photoelectron spectroscopy (IPES).[56-66] Using these measurements to understand the energy structure is crucial for designing devices and improving the photovoltaic characteristics.

### *1.4.2. Determination of Carrier Concentration*

Band-mapping was performed by ascertaining the film thickness-dependence of the Fermi level measurements.[45,67,68] Figure 1.9 shows the principle of band-mapping of doped organic semiconductors. When a doped organic semiconductor is in contact with an indium tin oxide (ITO) electrode, their $E_F$s are aligned. Accordingly, the vacuum level ($E_{VAC}$) is bent and the value of the work function, which is defined as the difference between $E_{VAC}$ and $E_F$ (Fig. 1.9, red double-headed arrows), changes with the thickness of the film. Thus, the variation in band-bending with the thickness of the doped organic semiconductor film can be directly mapped by measuring the work function with a Kelvin probe. The band-bending gives the depletion layer width ($W_{dep}$) and the built-in potential ($V_{bi}$). The carrier concentration (N) can be calculated using Eqs. (1.8) and (1.9). Furthermore, the doping efficiency, i.e., the ratio of the number of generated carriers to the amount of doped impurity can be determined.

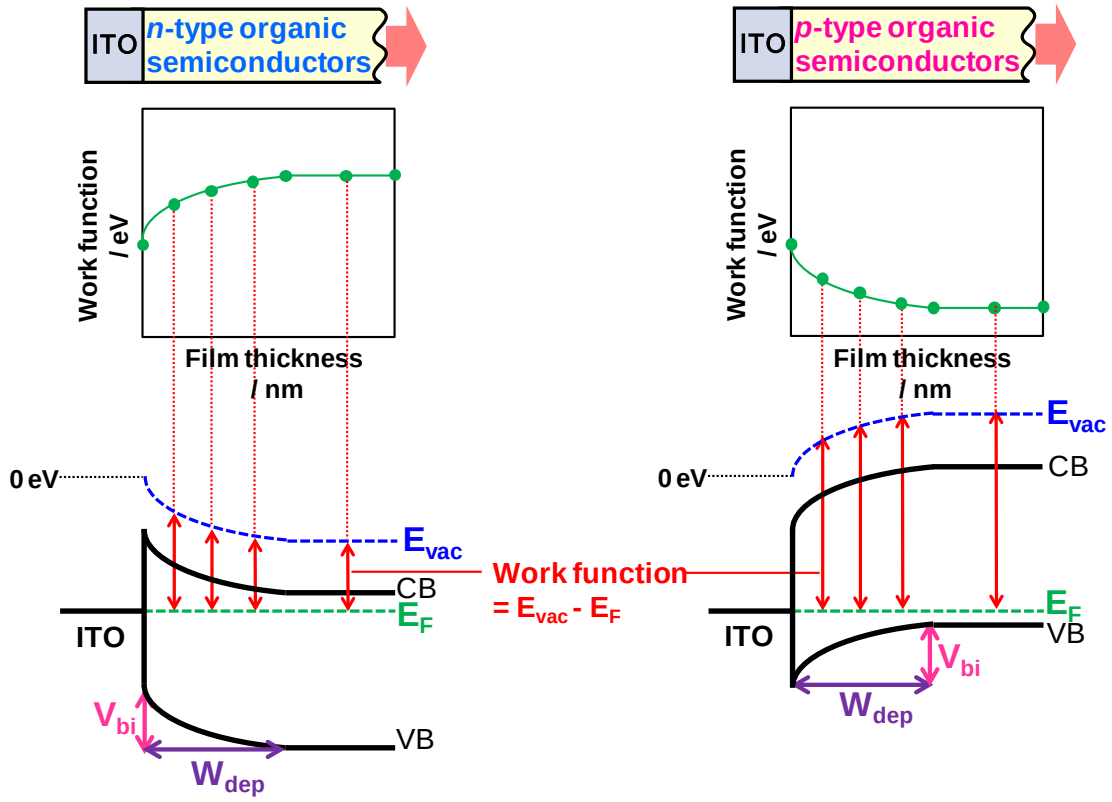


Fig. 1.9 Principle of energy band mapping of *n*-type (left) and *p*-type (right) Schottky junctions. CB and VB denote the conduction and valence bands, respectively.

## 1.5. Donor/Acceptor Sensitization

Organic solar cells have been substantially developed in the last decade.[69-71] Since the pioneering work of Tang[11] in 1986, the photo-conversion efficiency of organic solar cells has gradually increased up to 12%,[72] which is comparable to amorphous silicon. Donor (D)/Acceptor (A) sensitization has been crucial for this development. In order to obtain a photocurrent, the following process is a fundamental requirement; excitons generated by the absorption of light dissociate into free electrons and holes, which then move to the electrodes by carrier transport. That is, the efficient

dissociation of excitons is absolutely vital for generating large photocurrents. However, it is difficult to dissociate excitons in a single organic semiconductor due to the strong attractive forces. The force acting on the positive and negative charges of the exciton (F) are represented by Coulomb's Law (Eq. (1.10)),

$$F = \frac{1}{4\pi\varepsilon\varepsilon_0}\frac{q_1 q_2}{r^2} \qquad (1.10)$$

where ε, $\varepsilon_0$, r, and q are the relative dielectric constant, the dielectric constant in a vacuum, the distance between the charges, and the magnitudes of the charges, respectively. Inorganic semiconductors have relatively large ε (>10). Thus, weakly bound Wannier excitons are formed, which can easily separate into free carriers (Fig. 1.10 (left)). On the other hand, organic semiconductors have relatively small ε (~4).[73,74] Thus, strongly bound Frenkel excitons are formed, which cannot separate into free carriers (Fig. 1.10 (right)). In order to solve this problem, a device structure in which two organic semiconductor materials are in contact is required for OSCs. Electrons excited by light irradiation of a single molecule film relax before dissociation (Fig. 1.11(a)). On the other hand, a combination of a donor molecule (D) and an acceptor molecule (A) can separate the positive and negative charges to the highest occupied molecular orbital (HOMO) of D and the lowest unoccupied molecular orbital (LUMO) of A, respectively (Fig. 1.11(b)). The separated charges form a CT exciton which can dissociate easily. Thus, this D/A system is essential if a large photocurrent is to be obtained.

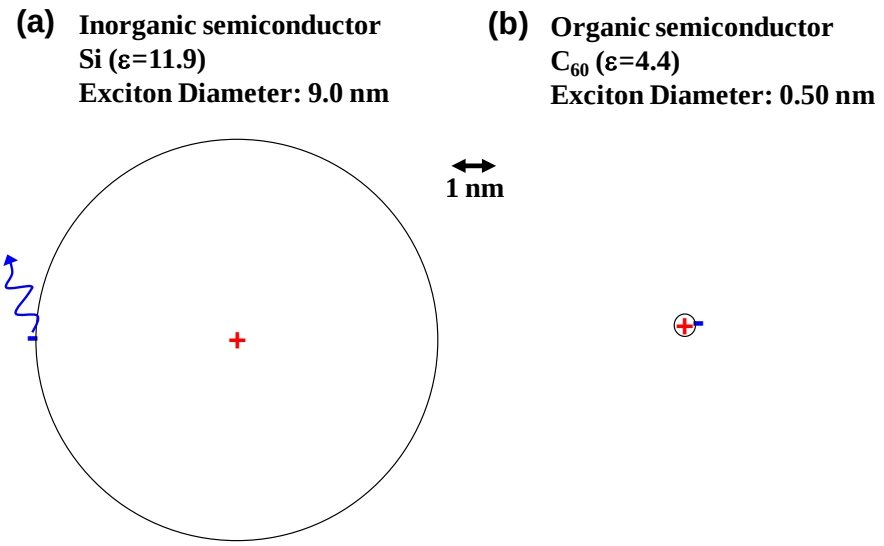


Fig. 1.10 Schematic illustrations of (a) Wannier exciton generated in Si. (b) Frenkel exciton generated in $C_{60}$.

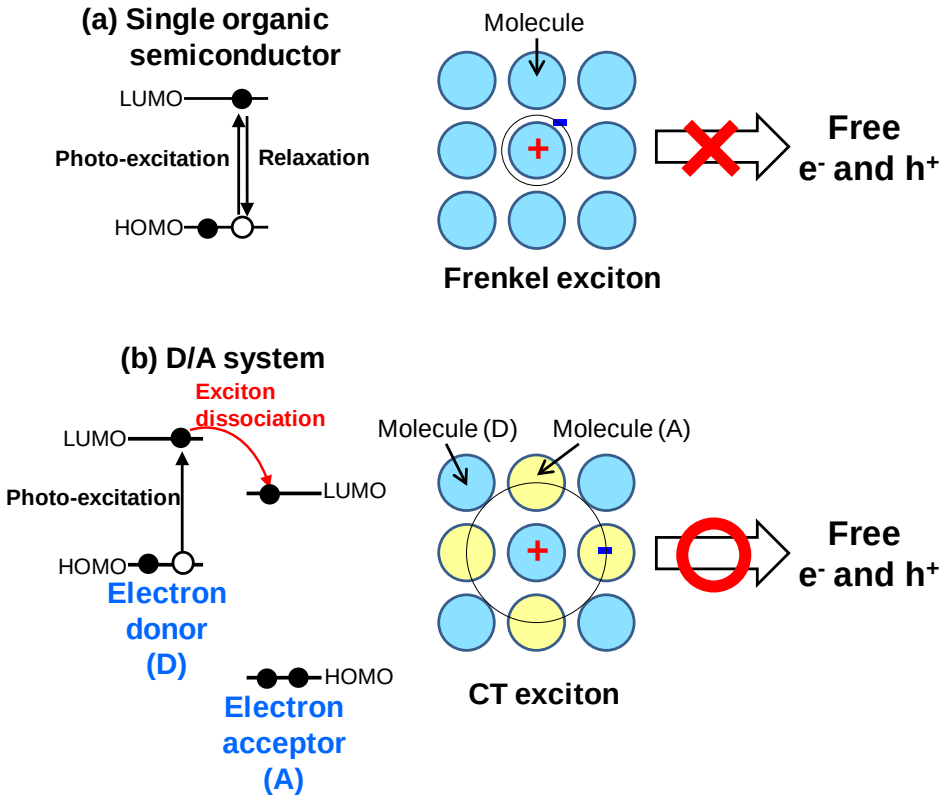


Fig. 1.11 Schematic energy diagrams and models of photo-generated excitons in (a) single organic semiconductor and (b) D/A system.

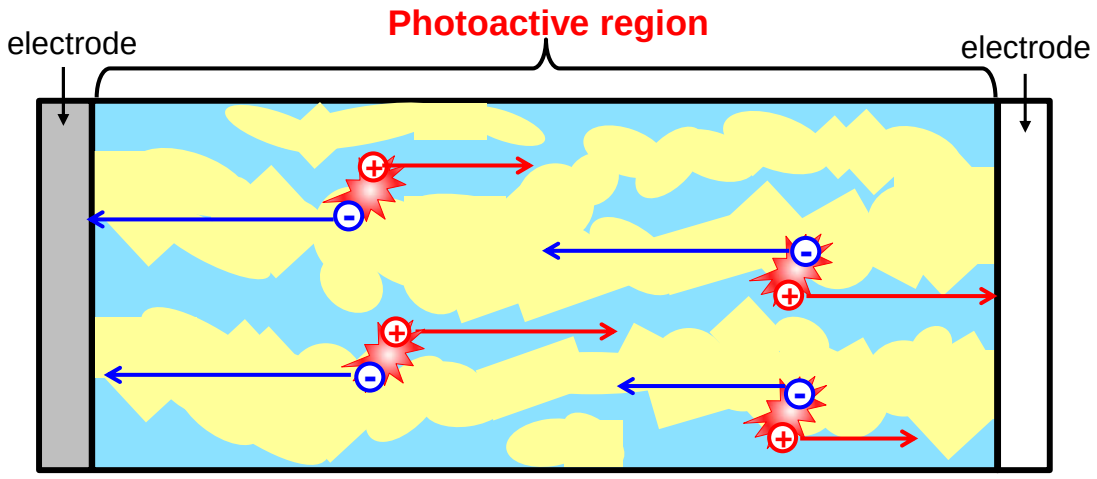


Fig. 1.12. Schematic illustration of co-deposited film.

In order to dissociate all the excitons, a co-deposited film, i.e., a mixed film with donor and acceptor molecules such that there are D/A interfaces throughout the film, is necessary, (Fig. 1.12).[75-77] In order to generate a large number of free carriers the total area of the D/A interfaces must be large. Furthermore, a thick film is needed in order to absorb all of the incoming light. However, thick organic semiconductor films generally have extremely high resistance, so, reducing the resistance by doping is necessary. Doping co-deposited films is a new approach. Only a few studies on doping to photoactive layer have been reported. Ishiyama et al. successfully performed the formation of *pn*-homojunctions in a co-deposited film consisting of $C_{60}$ and α-sexithiophene (6T).[43,44,78] Kubo et al. achieved operation of thick photovoltaic cells incorporating a doped co-deposited film consisting of $C_{60}$ and $H_2Pc$.[79] Doping co-deposited films has the potential for realizing high efficiency photovoltaic cells. Thus, the author investigated the effects of doping on co-deposited films (see Chapter 6).

## 1.6. Purpose of This Thesis

Impurity doping to control the *pn*-junction characteristics is vital in order to improve the photoconversion efficiency in organic solar cells as well as in inorganic solar cells. While *pn*-control of the typical inherently *n*-type $C_{60}$ has been reported previously, it hasn't been shown whether or not the same control can be achieved in the typical inherently *p*-type metal-free phthalocyanine ($H_2Pc$) and hole transport materials (HTMs). The author has attempted to confirm whether or not this *pn*-control can be applied to any organic semiconductor in order to design high-efficiency organic solar cells. Thus, an investigation of the effects of doping on $H_2Pc$ and HTMs was performed.

Moreover, precise device design requires a quantitative evaluation of the carrier concentration in doped organic semiconductors. However, correlation between the carrier concentration and the doping concentration hasn't so far been clarified. In particular, there have scarcely been any reports of studies on the doping of co-deposited films with photoactive D/A interfaces. The author believes that doping of co-deposited films is a key issue for the development of organic solar cells. Thus, in this thesis, the author has attempted to quantify the carrier concentration in doped single and co-deposited organic semiconductor films.

## 1.7. Overview of This Thesis

The effects of doping on typical single semiconductors are clarified.

In chapter 3, control of the conduction type and the formation of *pn*-homojunctions in single $H_2Pc$ films by intentionally doping with cesium carbonate ($Cs_2CO_3$) and $MoO_3$ is described, even though $H_2Pc$ is conventionally regarded as being inherently *p*-type.

In chapter 4, observations showing improvements made in the photovoltaic characteristics by p-type doping of hole-transport materials (HTMs), which offer high open-circuit voltages, are reported. Observation of strong charge transfer (CT) absorption by heavily $MoO_3$ doped HTMs revealed the formation of CT complexes. $MoO_3$-doping of HTMs offered the formation of built-in potentials and a decrease in resistance.

Evaluation of the carrier concentration and energy band structure of doped organic semiconductors is absolutely necessary for precise device fabrication. Thus, carrier concentration of single and co-deposited films was investigated.

In chapter 5, band-mapping of doped $C_{60}$ is demonstrated using a Kelvin probe. The carrier concentrations in $C_{60}$ films doped with $Cs_2CO_3$ and $MoO_3$ were precisely determined. An ionization efficiency of 10% is suggested, which is significantly less than that for Si. The CT complex formed, i.e., $Cs_2CO_3^+$–$C_{60}$, is essentially the same as for the CT exciton. It is assumed that this low ionization efficiency is due to the strong attractive force between the small electron orbital and the positively ionized donor.

In chapter 6, the ionization sensitization of the dopants is revealed using measurements of the carrier concentration in a co-deposited film. $H_2Pc$:$C_{60}$ co-deposited films show a significantly higher ionization efficiency of 97%, which is

comparable to doped silicon. Ionization sensitization was observed with both *p*- and *n*-type doping. A charge separation superlattice model that gives a reasonable explanation of this phenomenon is proposed. Charge separation in a co-deposited film accelerates the liberation of the carriers from the impurity levels. The ionization sensitization is a new knowledge which gives meaning to doping of co-deposited films, and is a unique characteristic of organic semiconductors.

## 1.8. References


1) S. M. Sze, *SEMICONDUCTOR DEVICES, Physics and Technology* (Wiley, New York, 1985).
2) S. M. Sze, *Physics of Semiconductor Devices* (Wiley, New York, 1969).
3) W. E. Spear, and P. E. Lecomber, *Solid State Commun.*, **17**, 1193 (1975).
4) M. A. Green, *Silicon Solar Cells: Advanced Principles and Practice* (Bridge Printery, Sydney, 1995).
5) M. S. Green, "Solar Cells" in S. M. Sze, Ed., *Modern Semiconductor Device Physics*, (Wiley Interscience, New York, 1998).
6) M. Yamaguchi, T. Takamoto, K. Araki, *Sol. Energy. Mater. Sol. Cells*, **90**, 3068 (2006).
7) W. O. Groves, A. H. Herzog, and M. G. Craford, *Appl. Phys. Lett*., **19**, 184 (1971).
8) A. A. Bergh and P. J. Dean, *Light Emitting Diodes* (Clarendon, Oxford, 1976).
9) S. Nakamura and G. Fasol, *The Blue Laser Diode* (Wiley, New York, 1977).
10) H. Akamatu, H. Inokuchi, and Y. Matsunaga, *Nature*, **173**, 168 (1954).
11) C. W. Tang, *Appl. Phys. Lett.*, **48**, 183 (1986).
12) C. W. Tang, S.A. VanSlyke, *Appl. Phys. Lett*., **51**, 913 (1987).
13) M. Kubo, K. Iketaki, T. Kaji, and M. Hiramoto, *Appl. Phys. Lett*., **98**, 073311 (2011).
14) M. Kubo, T. Kaji, and M. Hiramoto, *AIP Adv*., **1**, 032177 (2011).
15) M. Hiramoto, M. Kubo, Y. Shinmura, N. Ishiyama, T. Kaji, K. Sakai, T. Ohno, and M. Izaki, *Electronics*, **3**, 351 (2014).
16) M. Hiramoto, K. Ihara, H. Fukusumi, and M. Yokoyama, *J. Appl. Phys.*, **78**, 7153 (1995).

17) G. D. Sharma, S. G. Sangodkar, and M. S. Roy, *Mater. Sci. Eng. B*, **41**, 222 (1996).

18) A. C. Varghese, C. S. Menon, *J. Mater. Sci*., **41**, 3521 (2006).

19) D. R. Kearns, G. Tollin, and M. Calvin, *J. Chem. Phys.*, **32**, 1020 (1960).

20) M. Maitrot, G. Guillaud, and B. Boudjema, J. J. André, and J. Simon, *J. Appl. Phys*., **60**, 2396 (1986).

21) E. J. Lous, P. W. M. Blom, L. W. Molenkamp, and D. M. de Leeuw, *Phys. Rev. B*, **51**, 17251 (1995).

22) J. Blochwitz, M. Pfeiffer, T. Fritz, and K. Leo, *Appl. Phys. Lett*., **73**, 729 (1998).

23) K. Walzer, B. Maennig, M. Pfeiffer, and K. Leo, *Chem. Rev.*, **107**, 1233 (2007) and references therein.

24) M. Kröger, S. Hamwi, J. Meyer, T. Riedl, W. Kowalsky, and A. Kahn, *Org. Electron*., **10**, 932 (2009).

25) M. Kubo, Y. Shinmura, N. Ishiyama, T. Kaji, and M. Hiramoto, *Appl. Phys. Express*, **5**, 092302 (2012).

26) M. Kubo, Y. Shinmura, N. Ishiyama, T. Kaji, and M. Hiramoto, *Mol. Crsyt. Liq. Cryst*., **581**, 13 (2013).

27) C. Ganzorig, and M. Fujihira, *Appl. Phys. Lett*., **77**, 4211 (2000).

28) D. Ivory, G. Miller, J. Sowa, L. Shacklette, R. Chance, and R. Baughman, *J. Chem. Phys*., **71**, 1506 (1979).

29) G. Parthasarathy, C. Shen, A. Kahn, and S. R. Forrest, *J. Appl. Phys*., **89**, 4986 (2001).

30) J. Kido, and T. Matsumoto, *Appl. Phys. Lett.*, **73**, 2866 (1998).

31) A. Nollau, M. Pfeiffer, T. Fritz, and Karl Leo, *J. Appl. Phys*., **87**, 4340 (2000).

32) S. Tanaka, K. Kanai, E. Kawanabe, T. Iwahashi, T. Nishi, Y. Ouchi, and K. Seki, *Jpn.*

*J. Appl. Phys*., **44**, 3760 (2005).

33) A. G. Werner, F. Li, K. Harada, M. Pfeiffer, T. Fritz, and K. Leo, *Appl. Phys. Lett*., **82**, 4495 (2003).

34) A. Werner, F. Li, K. Harada, M. Pfeiffer, T. Fritz, and K. Leo, *Adv. Funct. Mater.*, **14**, 255 (2004).

35) F. Li, A. Werner, M. Pfeiffer, K. Leo, and X. Liu, *J. Phys. Chem. B*, **108**, 17076 (2004).

36) F. Li, M. Pfeiffer, A Werner, K. Harada, K. Leo, N. Hayashi, K. Seki, X. Liu, and X. D. Dang, *J. Appl. Phys*., **100**, 023716 (2006).

37) C. J. Bloom, C. M. Elliott, P. G. Schroeder, C. B. France, and B. A. Parkinson, *J. Phys. Chem. B*, **107**, 2933 (2003).

38) C. K. Chan, F. Amy, Q. Zhang, S. Barlow, S. Marder, and A. Kahn, *Chem. Phys. Lett*., **431**, 67 (2006).

39) C.K. Chan, W. Zhao, A. Kahn, and I. G. Hill, *Appl. Phys. Lett.*, **94**, 203306 (2009).

40) T. Menke, D. Ray, J. Meiss, K. Leo, and M. Riede, *Appl. Phys. Lett*., **100**, 093304 (2012).

41) M. L. Tietze, F. Wölzl, T. Menke, A. Fischer, M. Riede, K. Leo, and B. Lüssem, *Phys. Status Solidi A*, **210**, 2188 (2013).

42) S. Schubert, Y. H. Kim, T. Menke, A. Fischer, R.Timmreck, L. Müller-Meskamp, and K. Leo, *Sol. Energy Mater. Sol. Cells*, **118**, 165 (2013).

43) N. Ishiyama, M. Kubo, T. Kaji, and M. Hiramoto, *Appl. Phys. Lett*., **101**, 233303 (2012).

44) N. Ishiyama, T. Yoshioka, T. Kaji, and M. Hiramoto, *Appl. Phys. Express*, **6**, 012301 (2013).

45) N. Ishiyama, M. Kubo, T. Kaji, and M. Hiramoto, *Org. Electron.*, **14**, 1793 (2013).

46) H. Liao, L. Chen, Z. Xu, G. Li, and Y. Yang, *Appl. Phys. Lett.*, **92**, 173303 (2008).

47) M. Kotani and H. Akamatu, *Bull. Chem. Soc. Jpn.*, **43**, 30 (1970).

48) M. Kotani and H. Akamatu, *Discuss. Faraday Soc.*, **51**, 94 (1971).

49) S. Saito, T. Soumura, and T. Maeda, *J. Vac. Sci. Technol. A*, **2**, 1389 (1984).

50) M. Iwamoto, A. Fukuda, and E. Itoh, *J. Appl. Phys.*, **75**, 1607 (1994).

51) M. Hiramoto, K. Ihara, and M. Yokoyama, *Jpn. J. Appl. Phys.*, **34**, 3803 (1995).

52) M. Pfeiffer, K. Leo, and N. Karl, *J. Appl. Phys.*, **80**, 6880 (1996).

53) Y. Harima, K. Yamashita, H. Ishii, and K. Seki, *Thin Solid Films*, **366**, 237 (2000).

54) E. Moons, A. Goossens, and T. Savenije, *J. Phys. Chem. B*, **101**, 8492 (1997).

55) N. Hayashi, H. Ishii, Y. Ouchi, and K. Seki, *J. Appl. Phys.*, **92**, 3784 (2002).

56) I. G. Hill and A. Kahn, *J. Appl. Phys.*, **84**, 5583 (1998).

57) R. Schlaf, B. A. Parkinson, P. A. Lee, K. W. Nebesny, and N. R. Armstrong, *Appl. Phys. Lett.*, **73**, 1026 (1998).

58) S. T. Lee, X. Y. Hou, M. G. Mason, and C. W. Tang, *Appl. Phys. Lett.*, **72**, 1593 (1998).

59) H. Ishii, K. Sugiyama, E. Ito, and K. Seki, *Adv. Mater.*, **11**, 605 (1999).

60) J. Blochwitz, T. Fritz, M. Pfeiffer, K. Leo, D.M. Alloway, P.A. Lee, and N.R. Armstrong, *Org. Electron.*, **2**, 97 (2001).

61) W. Gao and Kahn, *Appl. Phys. Lett.*, **79**, 4040 (2001).

62) W. Gao, and A. Kahn, *Org. Electron.*, **3**, 53 (2002).

63) W. Gao and A. Kahn, *Appl. Phys. Lett.*, **82**, 4815 (2003).

64) C. Chan, W. Gao, and A. Kahn, *J. Vac. Sci. Technol. A*, **22**, 1488 (2004).

65) W. Zhao and A. Kahn, *J. Appl. Phys.*, **105**, 123711 (2009).

66) W. Han, H. Yoshida, N. Ueno, and S. Kera, *Appl. Phys. Lett.*, **103**, 123303 (2013).

67) H. Ishii, N. Hayashi, E. Ito, Y. Washizu, K. Sugi, Y. Kimura, M. Niwano, Y. Ouchi, and K. Seki, *Phys. Stat. Sol. (a)*, **201**, 1075 (2004).

68) S. Hamwi, J. Meyer, T. Winkler, T. Riedl, and W. Kowalsky, *Appl. Phys. Lett*., **94**, 253307 (2009).

69) Y. Lin, Y. Li, and X. Zhan, *Chem. Soc. Rev*., **41**, 4245 (2012).

70) H. Spanggaard and F. C. Krebs, *Sol. Energy Mater. Sol. Cells*, **83**, 125 (2004).

71) H. Hoppe and N. S. Sariciftci, *J. Mater. Res*., **19**, 1924 (2004).

72) The efficiency chart published by National Renewable Energy Laboratory (NREL).

73) M. A. Abkowitz and A. I. Lakatos, *J. Chem. Phys*., **57**, 5033 (1972).

74) A. F. Hebard, R. C. Hadon, R. M. Fleming, and A. R. Kortan, *Appl. Phys. Lett*., **59**, 2109 (1991).

75) M. Hiramoto, H. Fujiwara, and M. Yokoyama, *Appl. Phys. Lett*., **58**, 1062 (1991).

76) M. Hiramoto, H. Fujiwara, and M. Yokoyama, *J. Appl. Phys*., **72**, 3781 (1992).

77) G. Yu, J. Gao, J. C. Hummelen, F. Wudl, and A. J. Heeger, *Science*, **270**, 1789 (1995).

78) N. Ishiyama, M. Kubo, T. Kaji, and M. Hiramoto, *Appl. Phys. Lett*., **99**, 133301 (2011).

79) M. Kubo, T. Kaji, and M. Hiramoto, *Appl. Phys. Lett*., **103**, 263303 (2013).

# Chapter 2:

# Experimental Equipment and Methods

## *2.1. Purification of Organic Semiconductors*

$C_{60}$ (Frontier Carbon Co., Ltd., nanom purple TL), $C_{70}$ (Frontier Carbon Co., Ltd., nanom orange STH), metal-free phthalocyanine ($H_2Pc$) (Dainippon Ink & Chemicals, Inc., Fastogen Blue EP-101), and *N*,*N*'-dimethyl-3,4,9,10-perylene tetracarboxylic diimide (Me-PTC) were purified to 7N (99.99999%) purity by temperature gradient sublimation in a quartz furnace comprising three sections at different temperatures (Fig. 2.1).[1,2] Crude samples of the organic semiconductors, each weighing 4g, were placed in the high temperature section, and highly purified millimeter-scale single crystals were grown by sublimation in the middle temperature section under $N_2$ flow after pre-heating. (Fig. 2.2). Impurities from the crude sample were expelled to the low temperature section. In order to obtain highly purified single crystals, the proper conditions with respect to each material are required. The detailed sublimation conditions are shown in Table 2.1. The hole transport material and donor dopant, cesium carbonate ($Cs_2CO_3$; Aldrich, 99.995%), and the acceptor dopants, molybdenum trioxide ($MoO_3$; Alfa Aeser, 99.9995%) and iron (III) chloride ($FeCl_3$; Aldrich, 99.99%), were used without further purification.

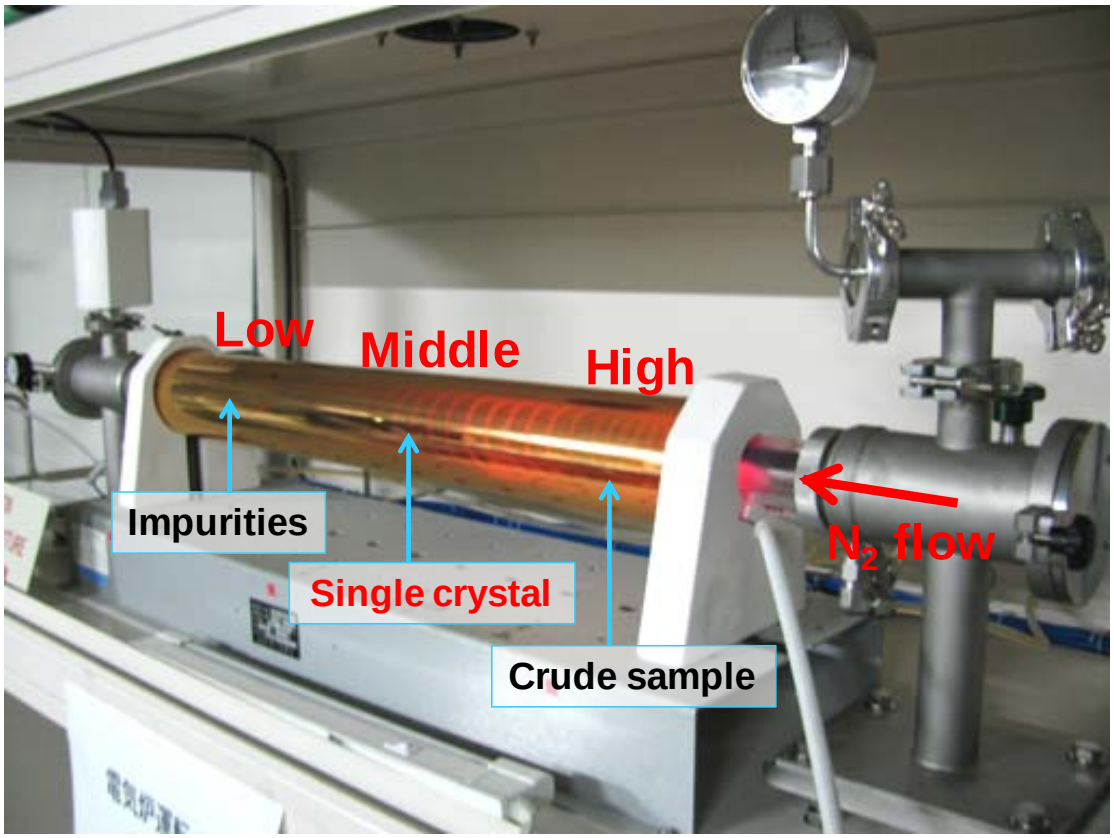


Fig. 2.1 Quartz furnace for growing highly purified single crystals of organic semiconductor.

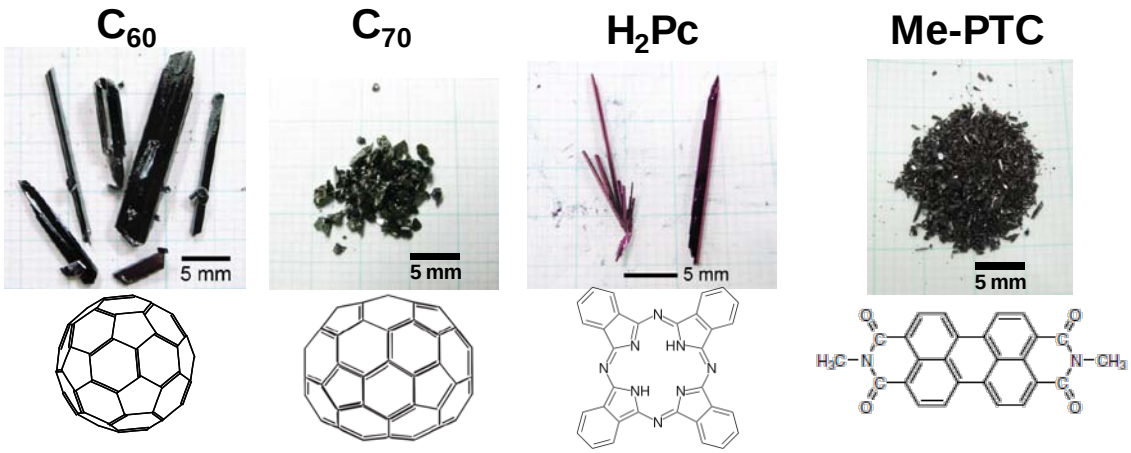


Fig. 2.2 Purified single crystals of organic semiconductors and their chemical structures.

Table 2.1 Sublimation conditions for the organic semiconductors

| | **Temperature / °C** | | | **$N_2$ flow Pressure / atm** | **Heating Time / h** |
|---|---|---|---|---|---|
| | **Low** | **Middle** | **High** | | |
| **Pre-heating** | 150 | 150 | 150 | Under vacuum | 1 |
| **$C_{60}$** | 310 | 580 | 745 | 1 | 36 |
| **$C_{70}$** | 365 | 635 | 800 | 1 | 36 |
| **$H_2Pc$** | 270 | 290 | 480 | 0.1 | 5 |
| **Me-PTC** | 270 | 300 | 500 | 0.1 | 5 |

## 2.2. Experimental Environment

The semiconductors were evaporated in an oil-free vacuum evaporation chamber (EpiTech Inc., ET300-6EHK) built into a glove box (UNICO, UL-1400ATW) ($H_2O$ < 0.7 ppm, $O_2$ < 0.2 ppm) (Fig.2.3). The samples were not exposed to air at any time during either film fabrication or measurement in order to avoid effects due to moisture and oxygen.

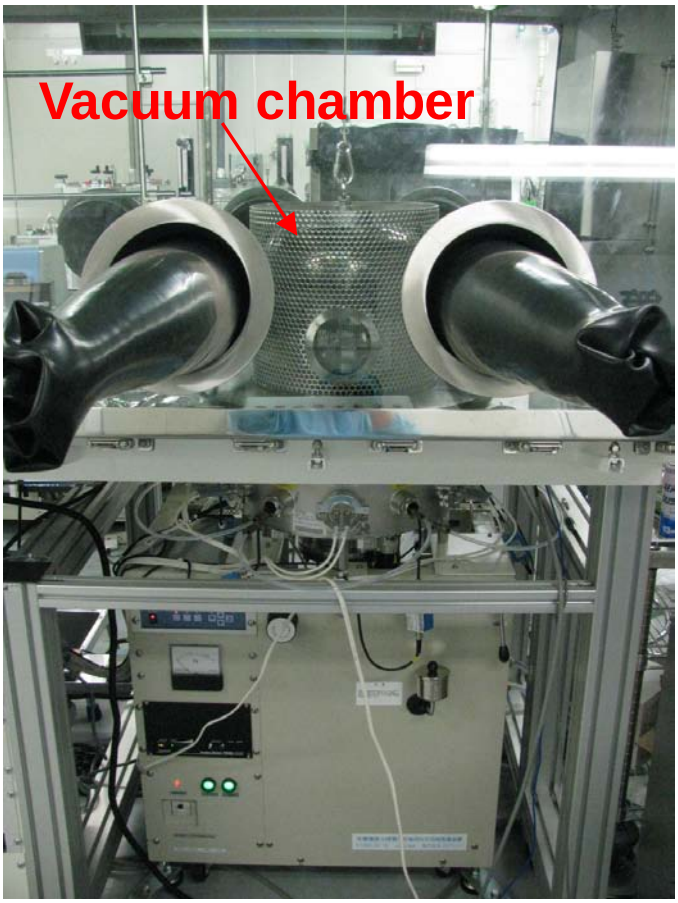


Fig.2.3 Vacuum chamber contained within a glove box.

## 2.3. Finely Controlled Doping

Doping of the organic semiconductors was performed by co-evaporation. Each material was put into individual $Al_2O_3$ melting pots. Evaporation was performed by resistance heating with a tungsten basket *in vacuo*. Evaporation rates of organic semiconductors and dopants were independently monitored by quartz crystal microbalances (QCMs) (Fig. 2.4).

Fine control of the deposition rate of small amounts of doping was performed using the QCM equipped with a computer monitoring system (ULVAC, Depoview).

The film thickness monitored by the QCM was calibrated using a surface profilometer (Dektak) (Fig. 2.5). The dependence of the film thickness of the dopant on evaporation time is shown in Fig. 2.6. The evaporation rate can be determined from the gradient of the baseline (Fig. 2.6, red line). The fluctuations observed in the measurement are attributed to temperature fluctuations in the cooling water flowing through the QCM. An evaporation rate of $10^{-5}$ nm $s^{-1}$ can be estimated from the gradient. When the host organic semiconductor evaporates at 0.2 nm $s^{-1}$, the ratio of the evaporation rate of the dopant to that of the host organic semiconductor gives a doping concentration of 50 ppm in volume. The deposition rate for the organic semiconductors was kept to 0.2 nm $s^{-1}$ and those of the dopants were adjusted from $10^{-5}$ to 2 x $10^{-3}$ nm $s^{-1}$ to give doping concentrations from 50 to 10,000 ppm.

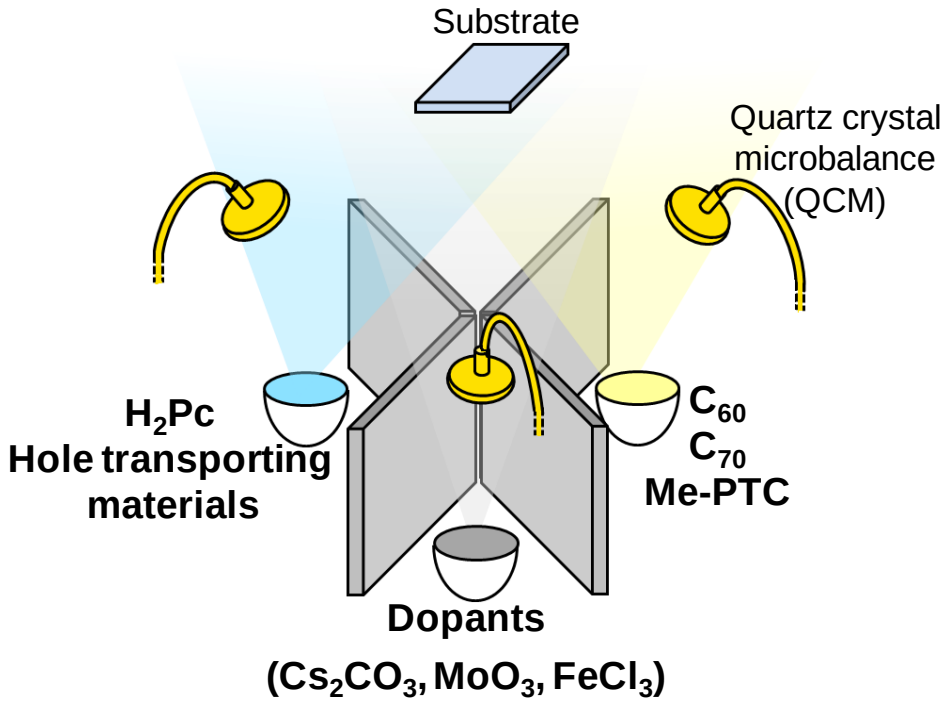


Fig. 2.4 Schematic illustration of coevaporation for doping of organic semiconductors.

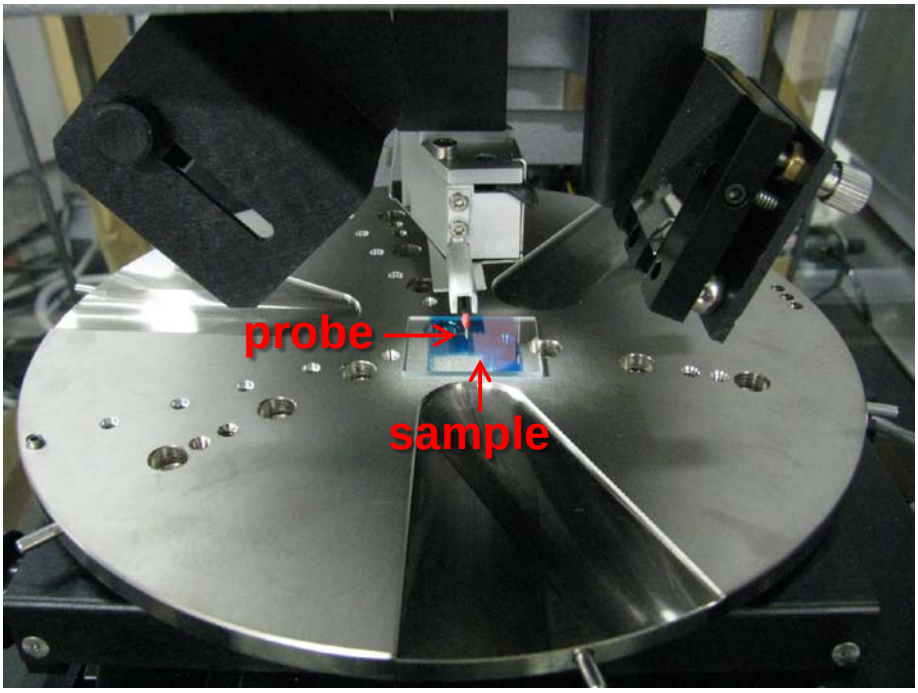


Fig. 2.5 Stylus surface profilometer for calibrating the film thickness.

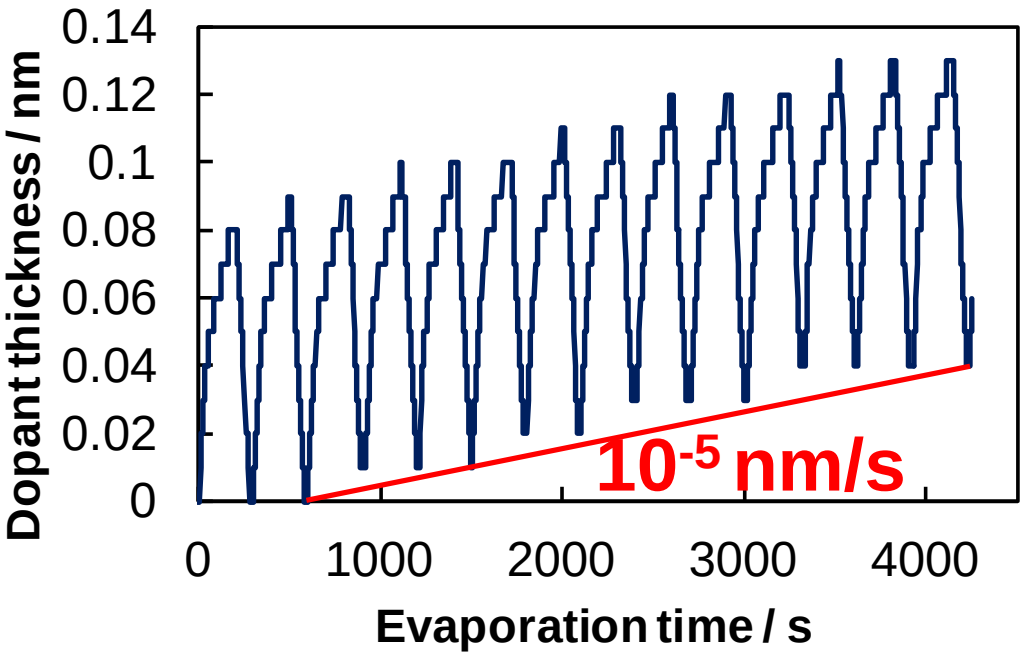


Fig. 2.6 Monitored dopant thickness vs. evaporation time.

## 2.4. Kelvin Probe Measurements

The Fermi levels ($E_F$) in the organic semiconductor films were determined using a Kelvin probe (Riken Keiki, FAC-1) (Fig.2.7).[3-11] The films were deposited on indium tin oxide (ITO) substrates. A gold plate, the work function of which was measured by atmospheric photoelectron spectroscopy, was used as a standard for the work function measurements. All $E_F$ measurements were performed in a $N_2$ atmosphere to avoid the effects of oxygen and moisture.

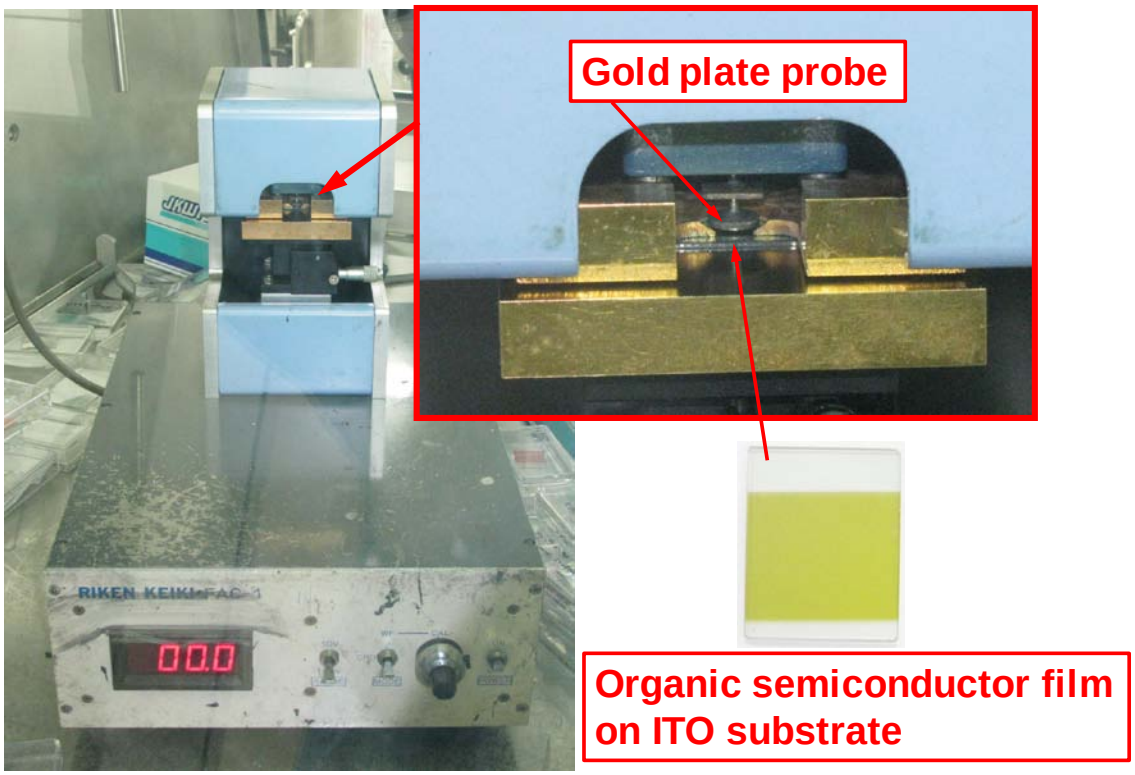


Fig. 2.7 Kelvin Probe for Fermi level measurements.

## 2.5. Capacitance-Voltage Measurements

Capacitance–voltage (C–V) measurements were performed in order to obtain the carrier concentration (N) of doped $C_{60}$ using Schottky junction cells comprising ITO/$MoO_3$ (10 nm)/$MoO_3$-doped $C_{60}$ (1 μm)/bathocuproin (BCP) (15 nm)/Ag (100 nm).[12,13] A periodic triangular bias from a function generator (Hokuto Denko HB-102) was applied to the cell and the dark current hysteresis (Fig. 2.8(a)) was measured using a picoammeter (Keithley 485).

The differential capacitance, $C_d$ (V) was calculated using Eq. (2.1),

$$C_d\ (V) = \Delta I\ (V)/8V_0 f \qquad (2.1)$$

where $\Delta I$ (V), $V_0$, and f are the difference in the dark current due to hysteresis, the amplitude of the scanning voltage, and the frequency of the periodic triangular bias, respectively. Mott-Schottky plots, i.e., $C_d^{-2}$ vs. V plots are shown in Fig. 2.8(b). $C_d^{-2}$ is given by Eq. (2.2)

$$C_d^{-2} = 2(V-V_{bi})/eN\varepsilon_0\varepsilon. \qquad (2.2)$$

The carrier concentration (N) can be determined from the gradient ($2/eN\varepsilon_0\varepsilon$) of the linear part (broken line).

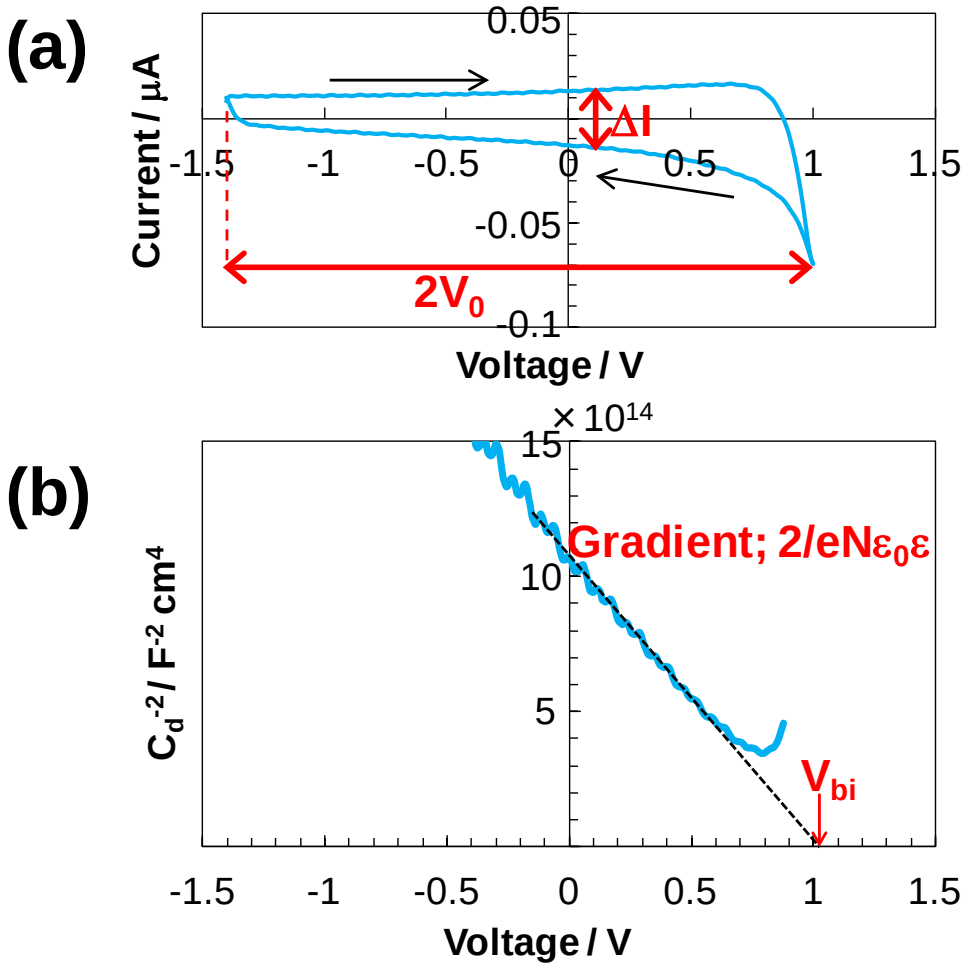


Fig. 2.8 Examples of (a) dark current hysteresis and (b) a Mott-schottky plot.

## 2.6. Fabrication of Organic Solar Cells

Indium tin oxide (ITO) coated glass substrates (Sanyo Vacuum Industries) were washed three times with water (10 min), methanol (10 min), and acetone (10 min), respectively, in an ultrasonic bath. All of the films were deposited by vacuum evaporation onto ITO glass substrates at $10^{-5}$ Pa using an oil-free vacuum evaporator (EpiTech Inc., ET300-6E-HK). The film thicknesses were determined by simultaneous monitoring of the deposition using quartz crystal microbalances (QCM). For doping co-deposited films, the organic semiconductors and dopants were

evaporated from different sources. Ag electrodes were deposited on the organic films through a metal mask with an aperture of 0.06 $cm^2$.

## 2.7. Measurements of Photovoltaic Properties

### *2.7.1. General*

The photovoltaic properties of the cells were measured by setting the cells in a vacuum sample container with a quartz glass window (Epi Tech Inc.) (Fig. 2.9). The container was evacuated to $10^{-3}$ Pa. The area of the photo-irradiated cell was precisely defined using a metal mask with an aperture of 0.04 $cm^2$.

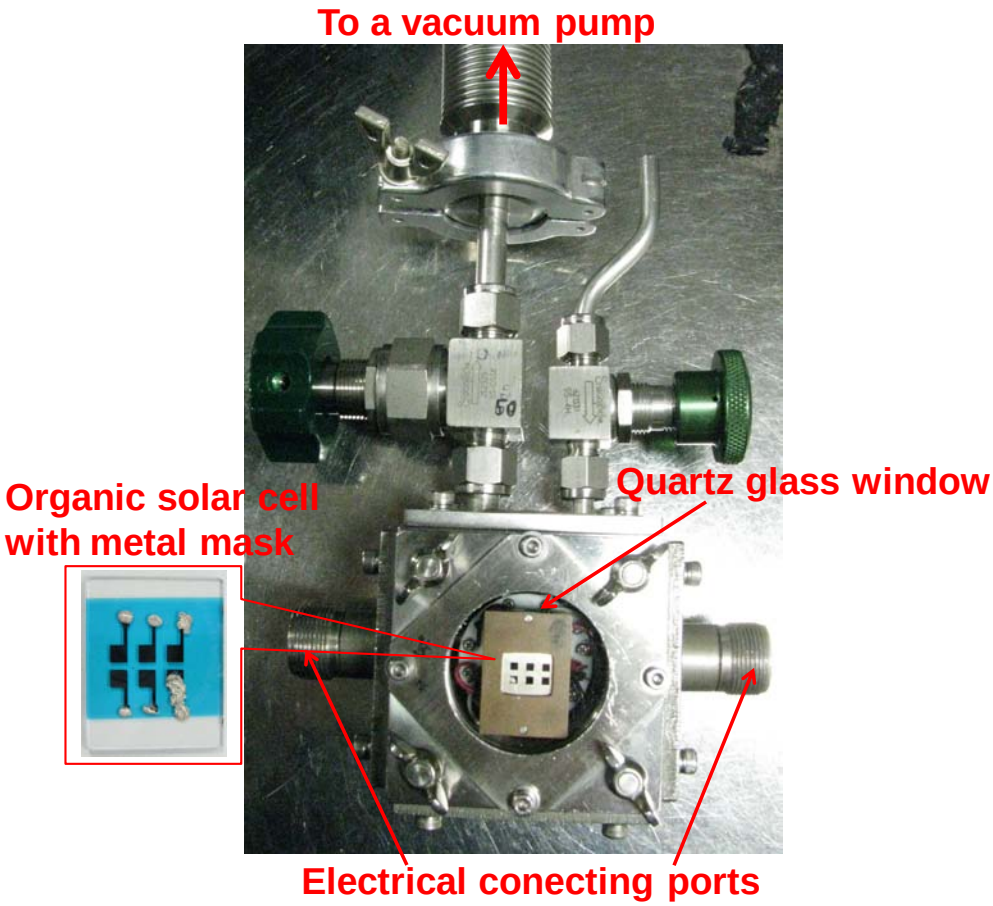


Fig. 2.9 Vacuum sample container with a quartz glass window.

### *2.7.2. Current Density-Voltage (J-V) Characteristics*

The current density-voltage (*J-V*) characteristics were measured by irradiating the cell with simulated solar light (USHIO INC., MS110AAA) (AM1.5, 100 mW $cm^{-2}$) (Fig. 2.10). Fig. 2.11 shows typical current-voltage (*J-V*) characteristics in the dark and under irradiation with the simulated solar light. The voltage was swept from -1.0 to 1.0 V at 0.1 V· $s^{-1}$. The photocurrent density at 0 V and the voltage at 0 $mAcm^{-2}$ are defined as the short-circuit current density ($J_{sc}$) and the open-circuit voltage ($V_{oc}$), respectively. The power conversion efficiency ($\eta_p$), i.e., the ratio of the maximum power that the cell can produce ($P_{max}$) to the incident light intensity ($P_{in}$), is given by the following equation (Eq.2.3).

$$\eta_P = \frac{P_{max}}{P_{in}} = \frac{J_{sc} \cdot V_{oc} \cdot FF}{P_{in}} \qquad (2.3)$$

The fill factor (FF) is the ratio of the maximum power (red shaded rectangle, Fig. 2.11) to the product of $J_{sc}$ and $V_{oc}$ (dashed line rectangle, Fig. 2.10) (Eq. 2.4).

$$FF = \frac{P_{max}}{J_{sc} \cdot V_{oc}} = \frac{J_{max} \cdot V_{max}}{J_{sc} \cdot V_{oc}} \qquad (2.4)$$

$J_{max}$ and $V_{max}$ are the current density and voltage at the maximum power output. FF signifies how close the J-V curve is to a step function. The closer the curve is to a step function, the larger the power that can be extracted.

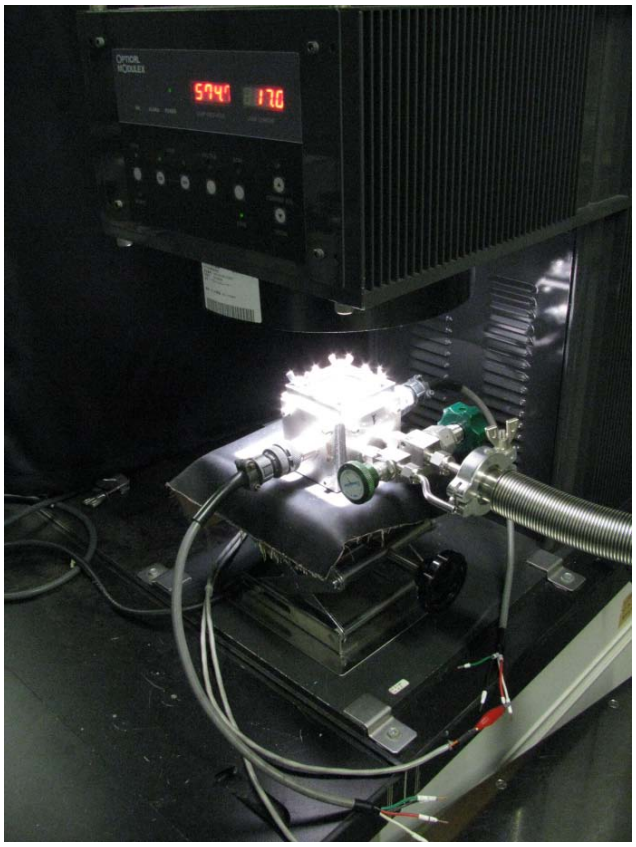

Fig. 2.10 J-V measurement with a solar simulator.

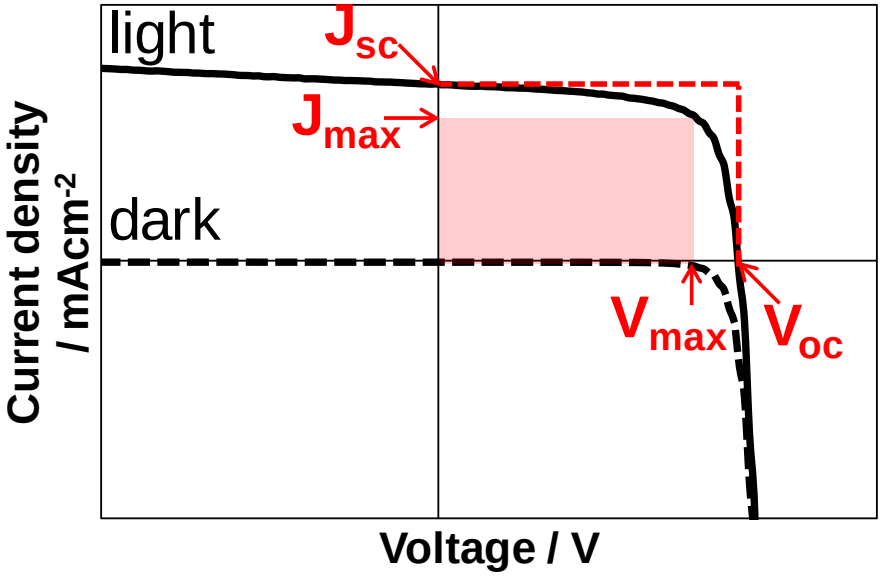


Fig. 2.11 J-V characteristics under light irradiation (black solid curve) and in the dark (black broken curve).

### *2.7.3. Action Spectrum*

The action spectrum is the incident photon to current conversion efficiency versus wavelength. Figure 2.12 shows the system used for measuring the action spectra. Monochromatic light from a Xe-lamp (Shimadzu, SPG-3ST) is passed through a monochromator and used to irradiate the photovoltaic cell. The difference between the photocurrent and the dark current, i.e., the number of carriers collected, was measured from 900 to 300nm in intervals of 20 nm under short-circuit conditions. The number of incident photons was determined by the same measurement using a standard silicon diode (Hamamatsu Photonics, S1337-66BQ). The external quantum efficiency (EQE) was determined from the ratio of the number of carriers collected to the number of incident photons.

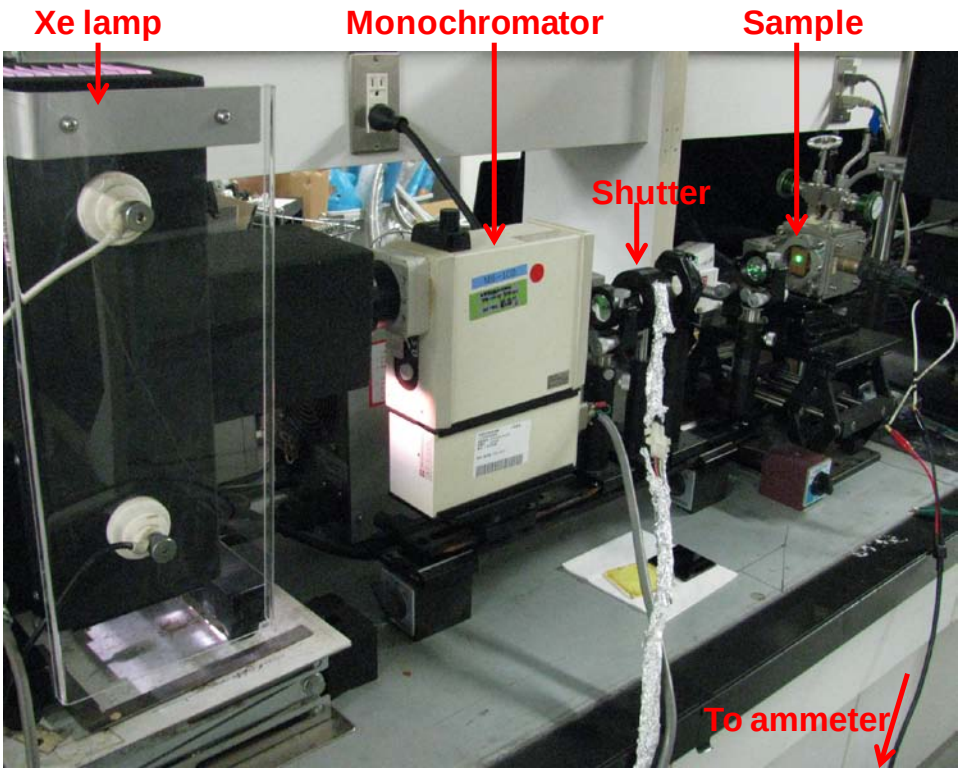


Fig. 2.12 Action spectrum measurement system.

## 2.8. Conductivity Measurements

The conductivity of the organic semiconductor films was measured by the Van der Pauw method using a Hall effect/specific resistance measurement system (TOYO Corporation, ResiTest8300). Fig. 2.13 shows the configuration of the samples used for conductivity measurements. A 400 nm-thick cross-shaped organic semiconductor film was deposited through a metal mask onto a quartz substrate. To make good ohmic contact organic semiconductor layers heavily doped with $MoO_3$ (50,000 ppm) (10 nm thick) were deposited on the arms of the cross, and Ag electrodes (100 nm thick) were deposited on top of these. Thus, the conductivity was obtained by a four-terminal resistance measurement.

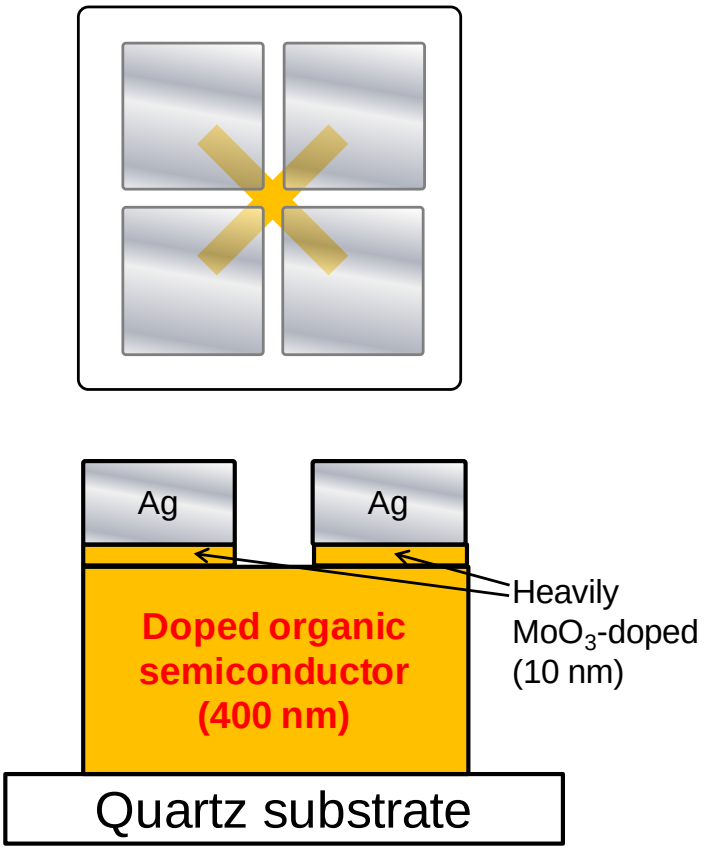


Fig. 2.13 Configuration of sample from the top (upper) and a cross-section (bottom).

## 2.9. References


1) M. Hiramoto and K. Sakai, *Mol. Cryst. Liq. Cryst.*, **491**, 284 (2008).

2) M. Hiramoto, M. Kubo, Y. Shinmura, N. Ishiyama, T. Kaji, K. Sakai, T. Ohno, and M. Izaki, *Electronics*, **3**, 351 (2014).

3) M. Kotani and H. Akamatu, *Bull. Chem. Soc. Jpn*., **43**, 30 (1970).

4) M. Kotani and H. Akamatu, *Discuss. Faraday Soc.*, **51**, 94 (1971).

5) S. Saito, T. Soumura, and T. Maeda, *J. Vac. Sci. Technol. A*, **2**, 1389 (1984).

6) M. Iwamoto, A. Fukuda, and E. Itoh, *J. Appl. Phys*., **75**, 1607 (1994).

7) M. Hiramoto, K. Ihara, and M. Yokoyama, *Jpn. J. Appl. Phys*., **34**, 3803 (1995).

8) M. Pfeiffer, K. Leo, and N. Karl, *J. Appl. Phys*., **80**, 6880 (1996).

9) Y. Harima, K. Yamashita, H. Ishii, and K. Seki, *Thin Solid Films*, **366**, 237 (2000).

10) E. Moons, A. Goossens, and T. Savenije, *J. Phys. Chem. B*, **101**, 8492 (1997).

11) N. Hayashi, H. Ishii, Y. Ouchi, and K. Seki, *J. Appl. Phys*., **92**, 3784 (2002).

12) A. J. Twarowski, and A. C. Albrecht, *J. Chem. Phys*., **70**, 2255 (1975).

13) S. M. Sze, *SEMICONDUCTOR DEVICES, Physics and Technology* (Wiley, New York, 1985).

14) L. J. van der Pauw, *Philips Research Reports*, **13**, 1 (1958).

# Chapter 3:
# *pn*-Control and *pn*-Homojunction Formation of Metal-free Phthalocyanine by Doping

"*pn*-Control and *pn*-Homojunction Formation of Metal-free Phthalocyanine by Doping"

**Yusuke Shinmura**, Masayuki Kubo, Norihiro Ishiyama, Toshihiko Kaji, and Masahiro Hiramoto, , *AIP Advances*, **2**, 032145 (2012).

## Abstract

The Fermi level ($E_F$) of metal-free phthalocyanine ($H_2Pc$), located at the center of the bandgap (4.4 eV), is shifted to 3.8 eV, close to the conduction band (3.5 eV), by cesium carbonate doping and shifted to 4.9 eV, close to the valence band (5.1 eV), by molybdenum oxide doping under oxygen free conditions. Formation of *n*- and *p*-type Schottky junctions and *pn*-homojunctions in single $H_2Pc$ films, confirmed by their photovoltaic properties, clearly demonstrates the formation of *n*- and *p*-type $H_2Pc$.

## 3.1 Introduction

Phthalocyanines and fullerene ($C_{60}$) are typical components in small-molecular-type organic photovoltaic cells.[1-8] Based on experience with inorganic solar cells, to create a built-in potential, *pn*-control of highly purified organic semiconductors by doping[9,10] is required.[11] For single $C_{60}$ films, we have reported complete *pn*-control[12] and *pn*-homojunction formation.[13]

For our next study, we chose metal-free phthalocyanine ($H_2Pc$) which is regarded as being *p*-type, with no reports of it being *n*-type. A few exceptions are *n*-type metal phthalocyanine doped with complexes having central metals like ruthenium,[10,14] although there have been intensive studies on doping[15,16] such as $F_4$-TCNQ acting as typical *p*-type dopants.[17] In this study, we used molybdenum oxide ($MoO_3$) [12,13,18,19] and cesium carbonate ($Cs_2CO_3$)[20,21] as acceptor and donor dopants, respectively. Since $H_2Pc$ is known to be *p*-type due to its unintentional doping with oxygen, the $H_2Pc$ films were not exposed to air at any time during fabrication and measurement.

For this letter, *pn*-control and *pn*-homojunction formation in $H_2Pc$ using $Cs_2CO_3$ and $MoO_3$ doping were reported. *n*-type $H_2Pc$ was fabricated under oxygen free condition.

## 3.2 Experimental

The $H_2Pc$ (Dainippon Ink & Chemicals) was purified once by single-crystal formed sublimation.[7,22] The acceptor and donor materials, $MoO_3$ (Alfa Aeser, 99.9995%) and $Cs_2CO_3$ (Aldrich, 99.995%), were used without further purification. Doped $H_2Pc$ films were fabricated by co-evaporation on indium tin oxide (ITO) glass substrates at a chamber pressure of $10^{-5}$ Pa using an oil–free vacuum evaporator (EpiTech Inc., ET300-6E-HK). The evaporation rate of $H_2Pc$ was kept to 0.2 nm $s^{-1}$. The evaporation rate of the dopants was 0.001 nm $s^{-1}$ to give doping concentrations of 5000 ppm.

The Fermi level ($E_F$) of 100 nm-thick $H_2Pc$ films was measured by Kelvin vibrating capacitor apparatus (Riken-Keiki, FAC-1). Both the evaporation chamber and the Kelvin probe were built into a glove-box (Miwa, DBO-1.5) purged with $N_2$ gas ($H_2O$ < 0.5 ppm, $O_2$ < 0.2 ppm). During film deposition and $E_F$ measurements, the $H_2Pc$ films were not exposed to air at any time. The current-voltage (J-V) characteristics and action spectra were measured at $10^{-5}$ Pa. The cells were protected from air by setting them in a sample container with a quartz window (EpiTech Inc.) inside the glove-box.

## 3.3 Results and Discussion

### *3.3.1. Control of Fermi Level in a Single $H_2Pc$ Film by $MoO_3$ and $Cs_2CO_3$ doping*

Since the $E_F$ of $Cs_2CO_3$ film[23] is located at 3.0 eV (Fig. 3.1), which is considerably more negative than the lower-edge of the conduction band of $H_2Pc$, 3.5 eV, it is reasonable that $Cs_2CO_3$ donates an electron to $H_2Pc$ and forms a charge transfer (CT) complex, i.e., $H_2Pc^-$---$Cs_2CO_3^+$. Here, the positive charge on the $Cs_2CO_3^+$ group can be regarded as a spatially fixed ion, i.e., an ionized donor. The negative charge on $H_2Pc^-$ can be liberated by thermal energy and acts as a free electron in the conduction band of $H_2Pc$, making it *n*-type. The opposite mechanism occurs for $MoO_3$ doping. Since the $E_F$ of $MoO_3$ film is located at 6.7 eV (Fig. 3.1), which is considerably more positive than the upper-edge of the valence band of $H_2Pc$, 5.1 eV, $MoO_3$ extracts an electron from $H_2Pc$ and forms a CT complex, i.e., $H_2Pc^+$---$MoO_3^-$.[24] Positive charge liberated from $H_2Pc^+$ makes $H_2Pc$ *p*-type.

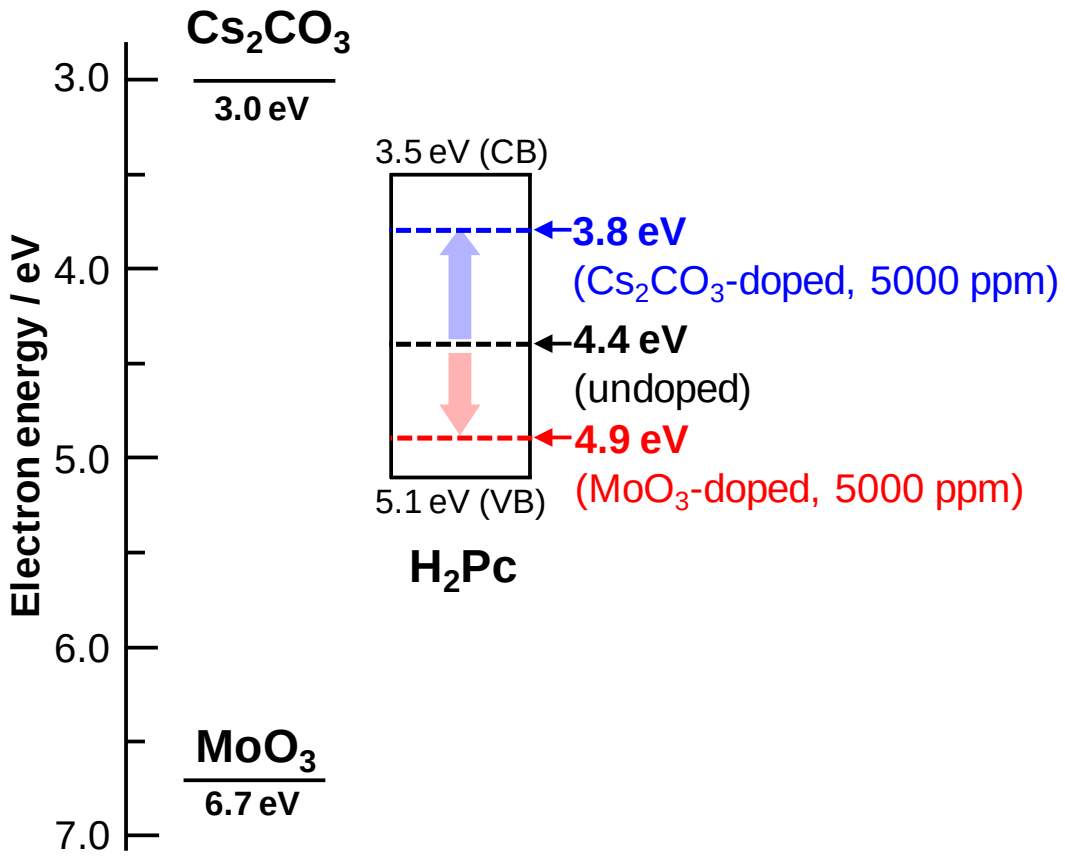


Fig. 3.1. Energy diagram of a $H_2Pc$ film. The broken lines show the energy levels of $E_F$ for undoped (black), $MoO_3$-doped (5000 ppm in volume concentration) (red) and $Cs_2CO_3$-doped (5000 ppm)(blue) $H_2Pc$ films. $E_F$ for $MoO_3$ (100 nm) and $Cs_2CO_3$ (100 nm) films are also shown. The energy levels of the upper edge of the valence band and the lower edge of the conduction band of a $H_2Pc$ film were determined by atmospheric photoelectron spectroscopy and the optical bandgap, respectively.

### *3.3.2. Formation of p- and n-Schottky Junctions and pn-Homojunction*

In order to confirm the formation of *n*- and *p*-type $H_2Pc$, the photovoltaic properties of $Cs_2CO_3$-doped and $MoO_3$-doped $H_2Pc$ single cells (Fig. 3.2(a)) were measured. Both cells showed photovoltages indicating that ITO/$MoO_3$ is positive and bathocuproine (BCP)/Ag is negative (Fig. 3.3(b)(d)). Differences appear in the action spectra of the external quantum efficiency (EQE) (Fig. 3.3(a)(c)). For the $Cs_2CO_3$-doped cell (Fig. 3.3(a)), under irradiation on the ITO side (hν(ITO), red curve), the action spectrum appears in the same region as the $H_2Pc$ absorption spectrum (black curve). On the other hand, under irradiation on the Ag side (hν(Ag), blue curve), the EQE values are very small and the action spectrum has peaks around the edges of the absorption spectrum. This is the so-called "masking effect" and proves that the photoactive junction is located at the $MoO_3$/$H_2Pc$ interface. Judging from the positive photovoltage on the $MoO_3$ side (Fig. 3.3(b)) and the photoactive junction at the $MoO_3$/$H_2Pc$ interface, the $Cs_2CO_3$-doped $H_2Pc$ film exhibits *n*-type behavior and a downwardly-bent Schottky junction can be drawn at the $MoO_3$/*n*-type $H_2Pc$ interface (Fig. 3.4(a)). Thus, the formation of *n*-type $H_2Pc$ by $Cs_2CO_3$ doping was confirmed by photovoltaic observations.

For the $MoO_3$-doped cell (Fig. 3.3(c)), under irradiation on the ITO side (hν(ITO), red curve), a strong masking effect is observed. Conversely, under irradiation on the Ag side (hν(Ag), blue curve), the action spectrum agrees well with the absorption spectrum (black curve). Obviously, the photoactive interface is located on the opposite side to that in the $Cs_2CO_3$-doped cell, i.e., at the $H_2Pc$/Ag interface. Judging from the negative photovoltage of the Ag electrode (Fig. 3.3(d)) and the photoactive junction at the $H_2Pc$/Ag interface, the $H_2Pc$ film exhibits *p*-type behavior

and a upwardly-bent Schottky junction can be drawn at the *p*-type $H_2Pc$/Ag interface (Fig. 3.4(b)). Thus, the formation of *p*-type $H_2Pc$ by $MoO_3$ doping was confirmed by photovoltaic observations. [25)]

For the next step, we fabricated a $Cs_2CO_3$-/$MoO_3$-doped homojunction cell (Fig. 3.2(b)). The homojunction was formed at the center of a 500 nm-thick $H_2Pc$ film. Irrespective of whether the ITO side (hν(ITO), Fig. 3.3(c), red curve) or the Ag side (hν(Ag), Fig. 3.3(c), blue curve) was illuminated both action spectra have significant peaks at the edges of the $H_2Pc$ absorption spectrum (black curve). The simultaneous observation of masking effects for light irradiation from both sides confirms that the photoactive zone is located neither at the $MoO_3$/$H_2Pc$ nor the $H_2Pc$/Ag interface, i.e., it is located deep in the bulk of the cell. Judging from the negative photovoltage on the Ag electrode (Fig. 3.3(f)) and the photoactive junction deep in the bulk of the cell, a *pn*-homojunction has been formed at the $Cs_2CO_3$-doped/$MoO_3$-doped junction (Fig. 3.4(c)).

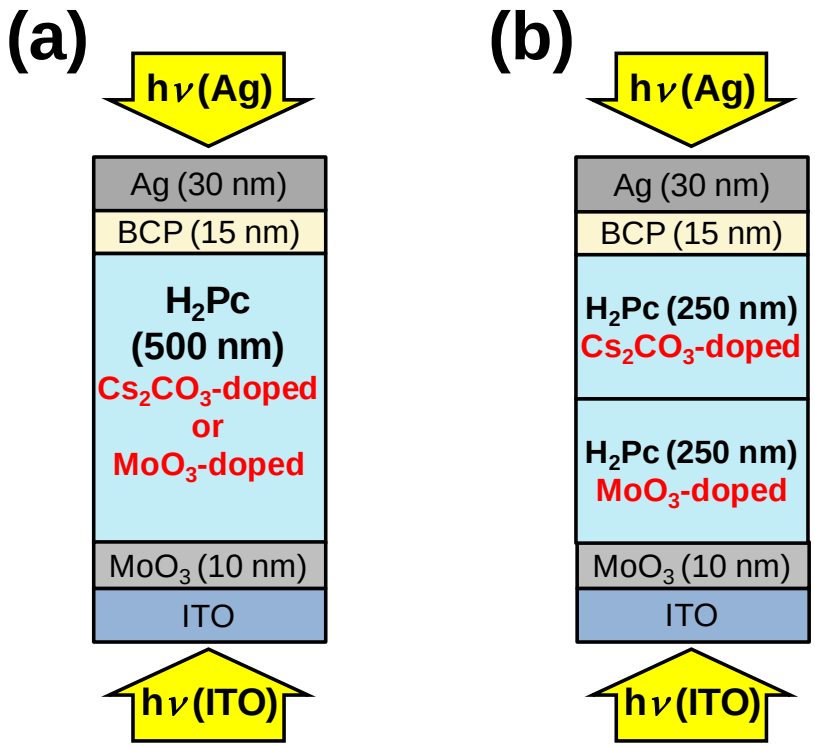


Fig. 3.2. The structure of $H_2Pc$ single film cells sandwiched between ITO/$MoO_3$ and BCP/semitransparent Ag electrodes. (a) The $H_2Pc$ films are doped uniformly with $Cs_2CO_3$ (5500 ppm) or $MoO_3$ (5600 ppm). (b) $Cs_2CO_3$ (5500 ppm)-/$MoO_3$ (5600 ppm)-doped homojunction cell. All cell thicknesses are 500 nm.

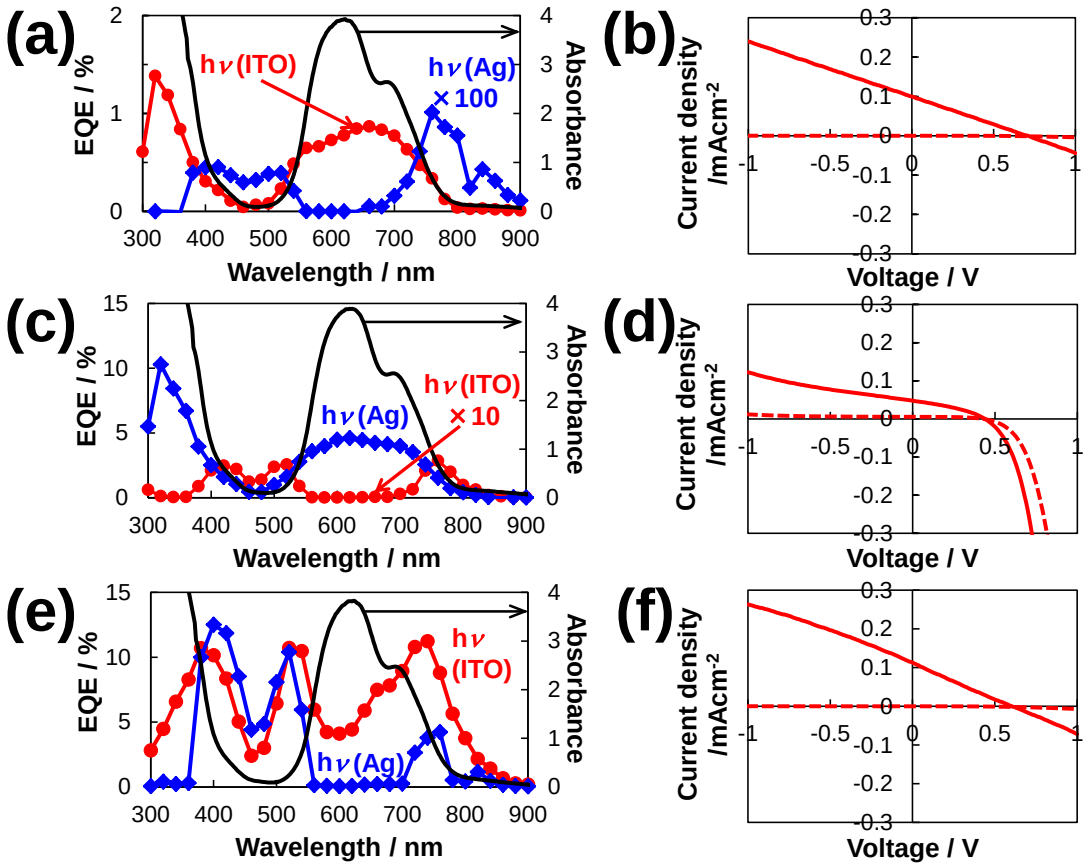


Fig. 3.3. Action spectra of the EQE of the short-circuit photocurrent and current-voltage characteristics for a $Cs_2CO_3$-doped cell (a)(b), a $MoO_3$–doped cell (c)(d), and a $Cs_2CO_3$-/$MoO_3$-doped homojunction cell (e)(f). For action spectra (a)(c)(e), the red and blue curves correspond to irradiation of light on the ITO electrode (hν(ITO)) and Ag electrode (hν(Ag)), respectively. The black curves show the absorption spectrum of the $H_2Pc$ film (500 nm). For current-voltage characteristics (b)(d)(f), photovoltage direction corresponds to that ITO/$MoO_3$ is positive and bathocuproine (BCP)/Ag is negative. Photocurrent under the simulated solar illumination (AM1.5, 100 $mWcm^{-2}$) and dark current are shown by solid and broken curves, respectively.

Based on the energy levels in Fig. 3.1, one can illustrate the energy band structures of an *n*-type Schottky junction at the $MoO_3$/*n*-type $H_2Pc$ interface (Fig. 3.4(a)),[26] a *p*-type Schottky junction at the *p*-type $H_2Pc$/Ag (work function: 4.1 eV) interface (Fig. 3.4(b)), and a *pn*-homojunction at the *p*-type $H_2Pc$/*n*-type $H_2Pc$ interface (Fig. 3.4(c)). On the other hand, the band bending in energy diagrams in Figs. 3.4(a), (b) and (c) can be also mapped in real scale based on the Kelvin probe measurements[18,27] and the widths of depletion regions for *n*-type (Fig 3.4(a)), *p*-type (Fig 3.4(b)) Schottky junctions and *pn*-homojunction (Fig 3.4(c)) were determined to 23, 30, and 35 nm, respectively. These band diagrams are consistent with the observed results.

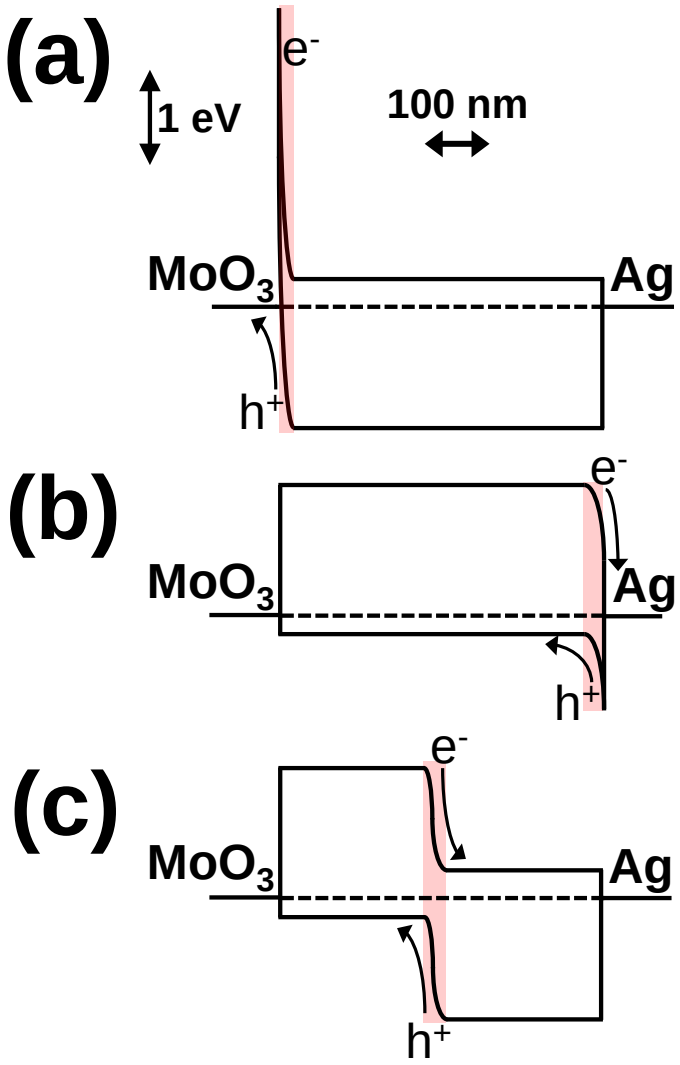


Fig. 3.4. Energy band diagrams for $Cs_2CO_3$-doped (a), $MoO_3$-doped (b), and $Cs_2CO_3$-/$MoO_3$-doped (c) cells. Scales of energy and length are indicated by double-headed arrows. Photocarrier generation occurs in the depletion regions (shaded).

## *3.4. Conclusion*

In conclusion, *n- and p*-type $H_2Pc$ films were fabricated by intentionally doping with $Cs_2CO_3$ and $MoO_3$. In order to make *n*-type $H_2Pc$, exposure to oxygen should be avoided. Conventionally, $H_2Pc$ and $C_{60}$ have been regarded as inherent *p*- and *n*-type semiconductors, respectively. However, *n*-$H_2Pc$ and *p*-$C_{60}$[12,13] can be formed by doping. So, it is reasonable that single organic semiconductors can, in general, be controlled to be *n*- or *p*-type, similar to inorganic semiconductors. Since the single $H_2Pc$ films showed only small photocurrent (Fig. 3.3(b)(d)(f)) and the co-deposited film consisting of $C_{60}$ and $H_2Pc$ showed high photovoltaic performance,[7,8] we are now investigating the direct doping into the photoactive $C_{60}$:$H_2Pc$ films to create designed built-in field in the co-deposited films.

## 3.5 References

1) Organic photovoltaics, Mechanisms, Materials and Devices, edited by S. –S. Sun and N. S. Sariciftci, published by CRC Press, New York, March (2005).

2) H. Spanggaard and F. C. Krebs, *Sol. Energy Mater. Sol. Cells*, **83**, 125 (2004).

3) H. Hoppe and N. S. Sariciftci, *J. Mater. Res*., **19**, 1924 (2004).

4) C. W. Tang, *Appl. Phys. Lett.*, **48**, 183 (1986).

5) M. Hiramoto, H. Fujiwara, and M. Yokoyama, *Appl. Phys. Lett.*, **58**, 1062 (1991).

6) M. Hiramoto, H. Fujiwara, and M. Yokoyama, *J. Appl. Phys.*, **72**, 3781 (1992).

7) M. Hiramoto and K. Sakai, *Mol. Cryst. Liq. Cryst*., **491**, 284 (2008).

8) T. Kaji, M. Zhang, S. Nakao, K. Iketaki, K. Yokoyama, C. W. Tang, and M. Hiramoto, *Adv. Mat.*, **23**, 3320 (2011).

9) M. Hiramoto, K. Ihara, and M. Yokoyama, *Jpn. J. Appl. Phys.*, **34**, 3803 (1995).

10) K. Harada, A. G. Werner, M. Pfeiffer, C. J. Bloom, C. M. Elliott, and K. Leo, *Phys, Rev. Lett.*, **94**, 036601 (2005).

11) W. E. Spear and P. E. Lecomber, *Solid State Commun.*, **17**, 1193 (1975).

12) M. Kubo, K. Iketaki, T. Kaji, and M. Hiramoto, *Appl. Phys. Lett.*, **98**, 073311 (2011).

13) M. Kubo, T. Kaji, and M. Hiramoto, *AIP Adv.*, **1**, 032177 (2011).

14) C. K. Chan, W. Zhao, S. Barlow, S. Marder, and A. Kahn, *Org. Electron.*, **9**, 575 (2008).

15) K. Walzer, B. Maennig, M. Pfeiffer, and K. Leo, *Chem. Rev.*, **107**, 1233 (2007) and references therein.

16) S. Tanaka, K. Kanai, E. Kawabe, T. Iwahashi, T. Nishi, Y. Ouchi, and K. Seki, *Jpn. J. Appl. Phys.*, **44**, 3760 (2005).

17) J. Blochwitz, M. Pfeiffer, T. Fritz, and K. Leo, *Appl. Phys. Lett.*, **73**, 729 (1998).

18) N. Ishiyama, M. Kubo, T. Kaji, and M. Hiramoto, *Appl. Phys. Lett.*, **99**, 133301 (2011).

19) T. Matsushima, Y. Kinoshita, and H. Murata, *Appl. Phys. Lett.*, **91**, 253504 (2007).

20) H. –H. Liao, L. –M. Chen, Z. Xu, G. Li, and Y. Yang, *Appl. Phys. Lett.*, **92** 173303 (2008).

21) T. Hasegawa, S. Miura, T. Moriyama, T. Kimura, I. Takaya, Y. Osato, and H. Mizutani, SID Int. Symp. Digest Tech. Papersl, **35**, 154 (2004)

22) R. A. Laudise, Ch. Kloc, P. G. Simpkins, and T. Siegrist, *J. Cyrstal Growth*, **187**, 449 (1998).

23) Since the $Cs_2CO_3$ film is transparent, metallic Cs is not formed during vacuum evaporation.

24) Codeposited films of $H_2Pc$:$Cs_2CO_3$ and $H_2Pc$:$MoO_3$ with a ratio of 1:1 showed new absorption bands which can be attributed to CT absorption.

25) For an undoped $H_2Pc$ cell, a photocurrent appeared throughout the visible region (400-800 nm) irrespective of which side was irradiated, though the magnitudes of the EQE values were only about 1% compared to the doped cells. This means that the photocurrent was generated uniformly in the $H_2Pc$ film bulk due to the intrinsic nature of undoped $H_2Pc$. Detailed examination suggests that the undoped $H_2Pc$ tends to have a slightly *n*-type nature.

26) Though there is a small barrier at the $Cs_2CO_3$-doped $H_2Pc$/Ag interface based on the measured work function of Ag (4.13 eV), it is not shown in Figs. 3.4(b) and (c) for simplification since its barrier height (0.37 eV) is far smaller than that of the $Cs_2CO_3$-doped $H_2Pc$/$MoO_3$ interface (2.93 eV).

27) N. Ishiyama, M. Kubo, T. Kaji, M. Hiramoto, *Appl. Phys. Lett.*, **101**, 233303 (2012).

# Chapter 4:
# Improved Photovoltaic Characteristics by $MoO_3$ Doping of Thick Hole-Transporting Films

"Improved Photovoltaic Characteristics by $MoO_3$-doping to Thick Hole Transporting Films", Yusuke Shinmura, Masayuki Kubo, Toshihiko Kaji, and Masahiro Hiramoto, , J*pn. J. Appl. Phys*., **52**, 04CR12 (2013).

## Abstract

Thick heterojunction cells composed of fullerene and p-type hole-transporting materials (HTMs) doped with molybdenum oxide ($MoO_3$) were fabricated. The Fermi level ($E_F$) of HTMs shifted toward the positive direction and close to the upper edge of the valence band following $MoO_3$ doping. These $E_F$ shifts indicate that intrinsic HTMs changed to be of the p-type. The introduction of p-type HTMs to the cells increased photocurrent density and fill factor. The increase in photocurrent density can be explained by the formation of built-in potential at the interface between p-type HTMs and $C_{60}$. On the other hand, the increase in fill factor can be explained by the drastic decrease in the resistance of 300-nm-thick HTM films, which reached a very small value of 2 Ω.

# 4.1 Introduction

Recently, the power conversion efficiency of organic solar cells has increased rapidly.[1-3] High open-circuit voltage ($V_{oc}$) is an essential factor for achieving high efficiency.[4-8] In the case of organic pn-junction cells, $V_{oc}$ depends on the gap between the highest occupied molecular orbital (HOMO) of the donor and the lowest unoccupied molecular orbital (LUMO) of the acceptor[9]. Namely, the wide gap results in a high $V_{oc}$. Therefore, the donors having a deep-lying HOMO are promising. One candidate for achieving this is the use of hole-transporting materials (HTMs) having a deep-lying HOMO.[10-12] Actually, heterojunction cells composed of HTMs and fullerene ($C_{60}$), which show a high $V_{oc}$, have been reported.[13]

On the other hand, another way to achieve high efficiency is the utilization of thick films in photovoltaic cells.[14] Films of more than 300 nm thickness can sufficiently absorb irradiated solar light, which provides a high photocurrent. Decreasing the cell resistance is essential for preventing cell performance degradation through the use of thick organic films which normally exhibit high resistance.

An effective way to decrease the resistance of organic semiconductors is impurity doping as in inorganic semiconductors.[15] Recently, we have reported the pn-control of $C_{60}$[16,17] and metal-free phthalocyanine[18] using molybdenum oxide ($MoO_3$) and cesium carbonate ($Cs_2CO_3$) as the acceptor and donor dopants, respectively. Tetrafluorotetracyano-quinodimethane ($F_4$-TCNQ)[19,20] and $MoO_3$[21,22] have been reported as suitable acceptor dopants for HTMs. Therefore, in this study, we adopted $MoO_3$ as the acceptor dopant for HTMs to decrease cell resistance.

In this paper, we report on the improvement of photovoltaic characteristics of heterojunction cells composed of $C_{60}$ and three kinds of thick HTMs doped with $MoO_3$,

as a preliminary step toward the fabrication of cells incorporating thick codeposited films.

## 4.2 Experimental

N,N'-Bis(3-methylphenyl)-N,N'-bis(phenyl)-benzidine (TPD) (Tokyo Chemical Industry, 99.99%), α-naphthylphenylbiphenyl diamine (NPD) (Luminescence Technology, 99.99%), and 4,4',N,N'-diphenylcarbazole (CBP) (Luminescence Technology, 99.99%) were used as the HTMs. The HTMs were used without further purification.

All of the films were deposited by vacuum evaporation onto indium-tin-oxide (ITO) glass substrates under $10^{-5}$ Pa pressure using an oil-free vacuum evaporator (ULVAC VTS-350M/ERH). $MoO_3$ doping was performed by coevaporation with the HTMs. The Fermi level ($E_F$) of HTM films with a thickness of 100 nm was measured using a Kelvin vibrating capacitor apparatus (Riken-Keiki FAC-1). Both the evaporation chamber and the Kelvin probe were built into a glovebox (Miwa DBO-1.5) purged with $N_2$ gas. The concentrations of $H_2O$ and $O_2$ were kept below 0.5 and 0.2 ppm, respectively. During film deposition and $E_F$ measurements, the HTM films were not exposed to air at any time. The specific resistance of 1-μm-thick HTM films were measured by the van der Pauw method using a Hall effect/specific resistance measurement system (TOYO ResiTest8300) without exposure to air by setting the sample films into a sample container inside the glovebox. Current voltage (*J*-*V*) characteristics and action spectra were measured by irradiating the films with simulated solar light (AM1.5, 100 mW $cm^{-2}$) and monochromatic light from a Xe lamp through a

monochromator, respectively, under vacuum at $10^{-3}$ Pa.

## 4.3 Results and Discussion

### *4.3.1. Fermi Level Shifts by Doping with $MoO_3$*

Figure 4.1 shows the energy diagrams of the HTMs, $C_{60}$, and $MoO_3$ films. The broken lines show the energetic positions of the Fermi levels ($E_F$) that were observed for the HTMs. The values of $E_F$ for undoped TPD, NPD, and CBP are 4.0, 4.5, and 4.9 eV, respectively, i.e., around the center of the band gap. This suggests that HTM films are intrinsic in nature. When doped with $MoO_3$ at approximately 4000 ppm, the values of $E_F$ for TPD, NPD, and CBP shifted toward the positive direction and reached 4.9, 5.0, and 5.7 eV, which is close to the upper edge of the valence band, signifying that the intrinsic HTMs changed to be of the p-type by $MoO_3$ doping.

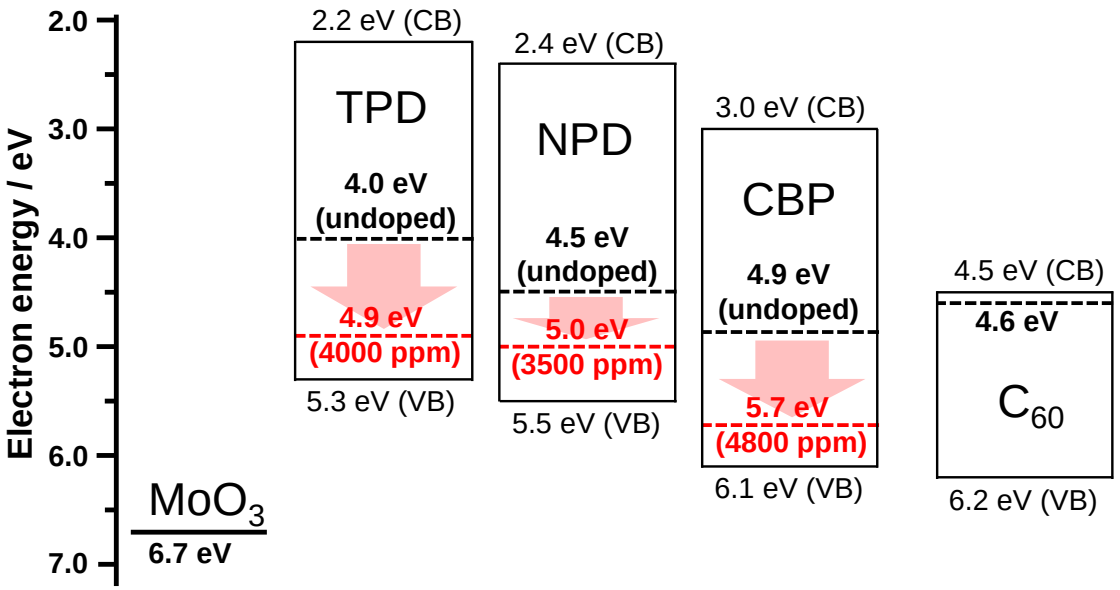


Fig. 4.1. Energy diagram of hole-transporting materials (TPD, NPD, CBP) and $C_{60}$. $E_F$ values of undoped and $MoO_3$-doped HTMs are shown by the black and red broken lines, respectively. $E_F$ of $MoO_3$ is also shown. VB and CB denote the valence band and the conduction band, respectively.

### *4.3.2. Formation of CT Complexes*

Figure 4.2 shows the absorption spectra for heavily $MoO_3$-doped (HTM:$MoO_3$ = 1:1 in volume) (red curves) and undoped HTMs (black curves). Both the undoped HTMs and $MoO_3$ are colorless. However, when $MoO_3$ was heavily doped, the colors of the HTM films changed to deep green (see photographs), and new broad absorption bands spreading from the visible to the near-infrared region appeared.

On the basis of the above observations, the doping mechanism can be illustrated in Fig. 4.3. $MoO_3$ can extract an electron from an HTM molecule, since it has a remarkably positive $E_F$ at 6.7 eV, which is more positive than the upper edge of the valence bands of all of the three HTMs. Therefore, the strong green absorption can

be attributed to the formation of CT complexes, i.e., $HTM^+$---$MoO_3^-$. The change to the p-type characteristic of the HTMs is induced by the liberation of positive charges due to thermal energy.

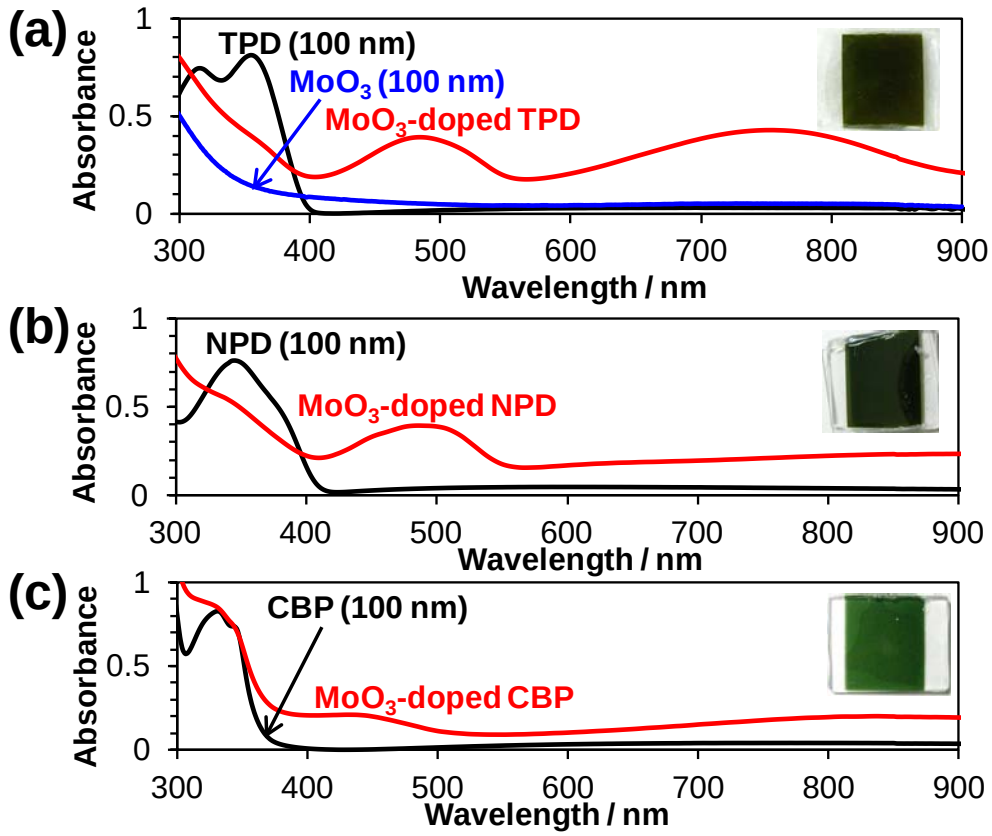


Fig. 4.2. Absorption spectra of (a) TPD, (b) NPD and (c) CBP. The red curves show heavily $MoO_3$-doped HTM films (HTM:$MoO_3$=1:1; total thickness, 200 nm). The black curves show undoped HTM films (thickness, 100 nm). The absorption spectrum of a single $MoO_3$ film is shown by the blue curve in (a). Photographs of heavily $MoO_3$-doped TPD (a), NPD (b), and CBP (c) films (HTM:$MoO_3$=1:1; total thickness, 400 nm) are also shown in the figures.

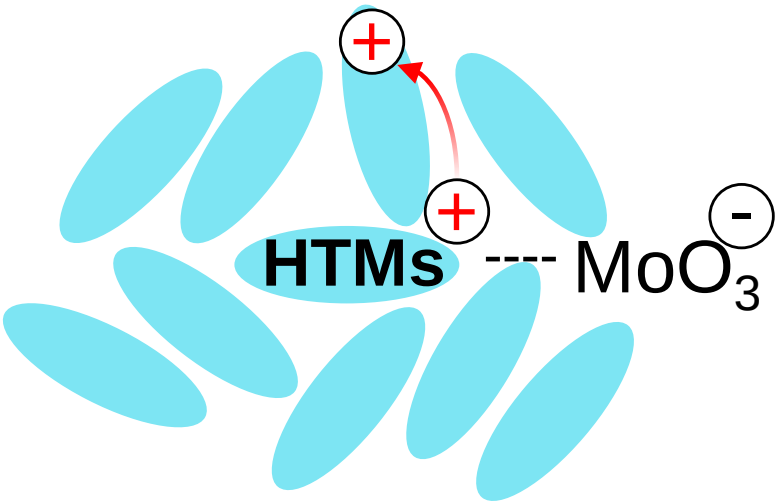


Fig. 4.3 Mechanism of $MoO_3$ doping of HTMs.

### *4.3.3. Decrease in Film Resistances*

Since the increase in the carrier concentration of the positive charges was expected to decrease resistance, we measured the specific resistance of the HTMs by the van der Pauw method. As shown in Fig. 4.4, the specific resistances of the undoped HTMs were extremely high, that is, higher than $10^8$ Ω cm. When the doping concentration of $MoO_3$ increased, the resistance decreased rapidly by four orders of magnitude and reached $6.5 \times 10^4$ Ω cm in the case of CBP. This result clearly proves the formation of p-type HTM.

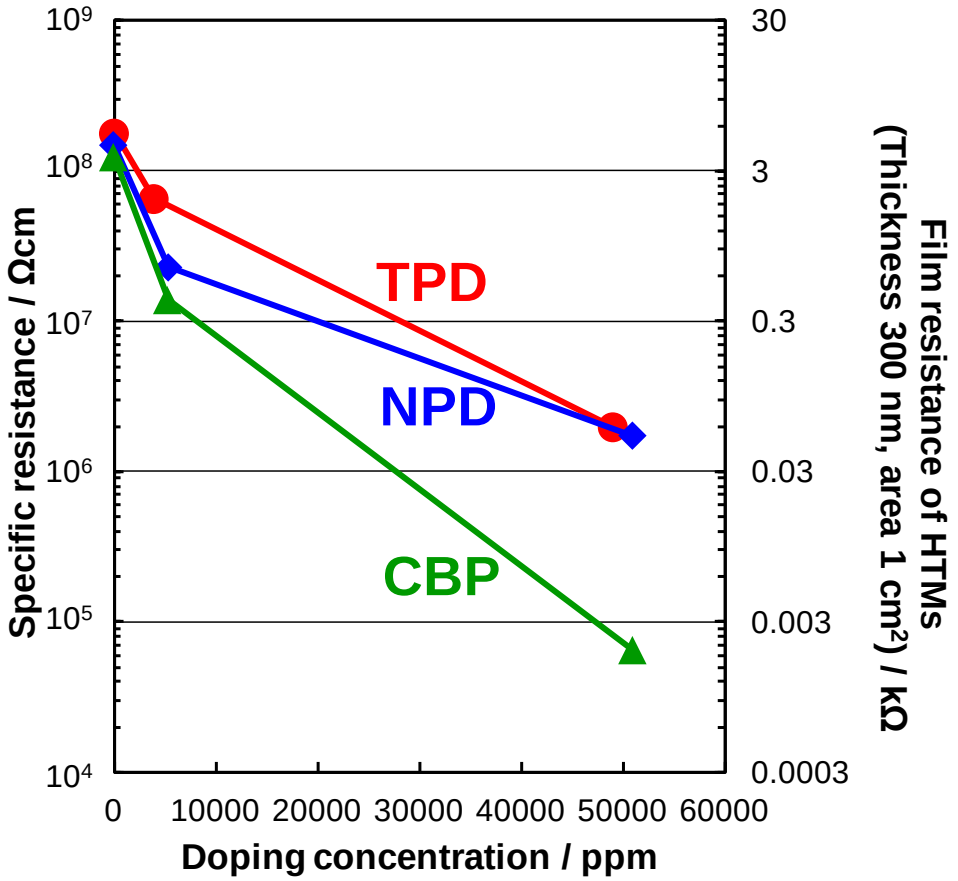


Fig. 4.4. Dependence of specific resistance of HTM films on doping concentration of $MoO_3$. 300-nm-thick and 1 $cm^2$ area film resistance calculated from specific resistance is also shown on the right vertical axis.

### *4.3.4. Improvement of Photocarrier Generation*

Since we have shown that p-type HTMs were fabricated, as a next step, we tried to incorporate the p-type HTMs into photovoltaic cells; thus, a series of HTM/$C_{60}$ heterojunction cells (Fig. 4.5) were fabricated. As shown in Fig. 4.6(a), in the case of TPD, $J_{sc}$ increased 2.7 times from 0.33 to 0.90 mA $cm^{-2}$ and the fill factor (FF) increased 1.5 times from 0.28 to 0.42 following $MoO_3$ doping at a concentration of 50,000 ppm. Similarly, in the cases of NPD and CBP, $J_{sc}$ increased 1.4 and 2.7 times,

and FF increased 1.5 and 2.0 times, respectively. Simultaneously, clear rectification characteristics were observed. As shown in Fig. 4.7, the external quantum efficiency (EQE) under short-circuit conditions was significantly increased by $MoO_3$ doping. Namely, photocarrier generation efficiency increased.

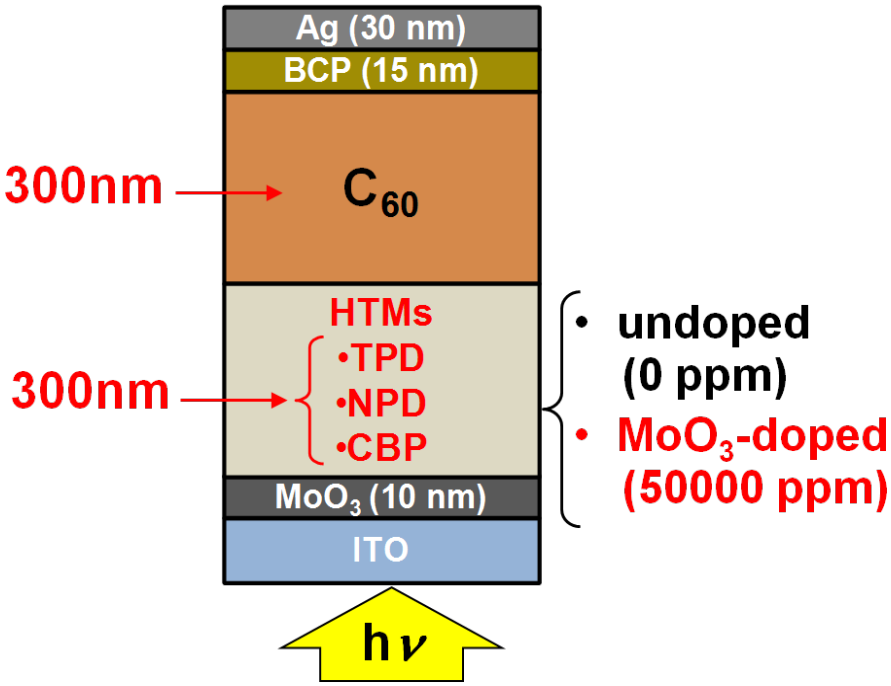


Fig. 4.5. Structure of HTM/$C_{60}$ heterojunction cells.

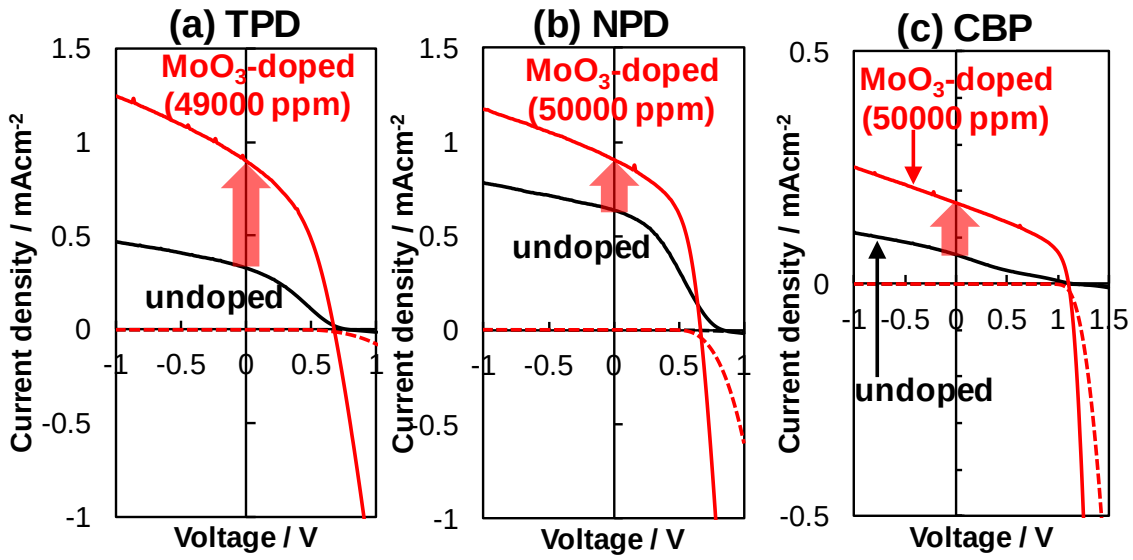


Fig. 4.6. *J-V* curves for heterojunction cells incorporating TPD (a), NPD (b), and CBP (c). The black and red curves correspond to cells incorporating undoped and $MoO_3$-doped HTMs, respectively. Photocurrent and dark current are shown by the solid and broken curves, respectively. Performances of $MoO_3$-doped cells. (a) $J_{sc}$, 0.90 mA $cm^{-2}$; $V_{oc}$, 0.67 V; FF, 0.42; Efficiency, 0.25%. (b) $J_{sc}$, 0.90 mA $cm^{-2}$; $V_{oc}$, 0.67 V; FF, 0.52; Efficiency, 0.31%. (c) $J_{sc}$, 0.17 mA $cm^{-2}$; $V_{oc}$, 1.10 V; FF, 0.43; Efficiency, 0.083%.

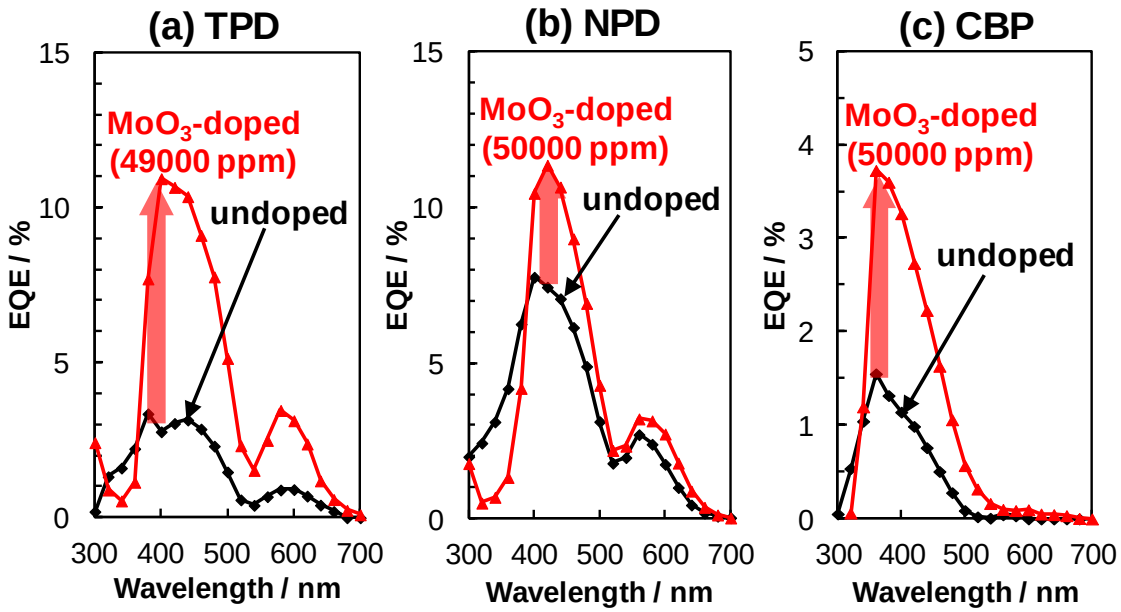


Fig. 4.7. Action spectra for heterojunction cells incorporating TPD (a), NPD (b), and CBP (c). The black and red curves correspond to the cells incorporating undoped and $MoO_3$-doped HTMs, respectively.

The increases in FF can be reasonably explained by the decrease in the resistance of 300-nm-thick HTM films. Actually, the resistance of a 300-nm-thick CBP film in a cell is only 2 Ω in the case of 50,000 ppm $MoO_3$ doping (Fig. 4.4, right vertical axis). The completely reverse relationship between the resistance of HTMs and FF (compare Figs. 4.4 and 4.8) with respect to $MoO_3$-doping concentration strongly supports the idea that a high FF was obtained due to a low HTM resistance.

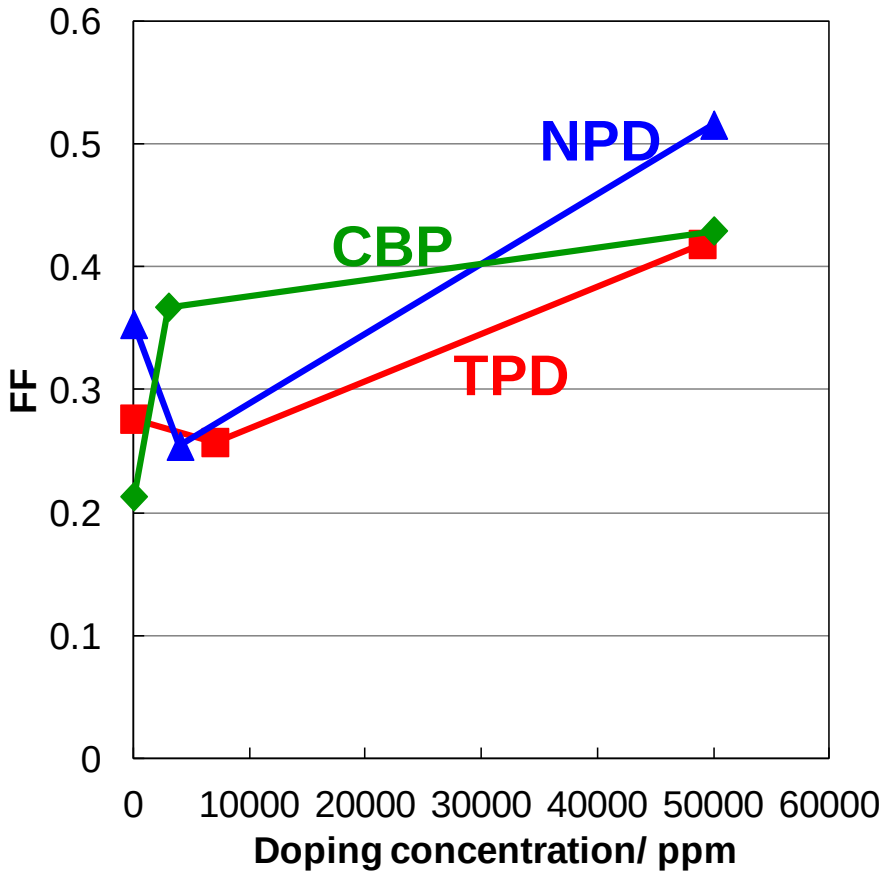


Fig. 4.8. Dependence of FF on doping concentration of $MoO_3$.

The increase in photocarrier generation efficiency can be reasonably explained by the formation of a built-in potential. Figure 4.9 shows the energy structures of heterojunctions of $C_{60}$/undoped TPD (a), and $C_{60}$/$MoO_3$-doped TPD (b), illustrated on the basis of the energy relationship shown in Fig. 4.1. The $E_F$s of TPD and $C_{60}$ are assumed to be aligned. In the case of undoped TPD [Fig. 4.9(a)], a low photocurrent is generated owing to the absence of a built-in potential at the TPD/$C_{60}$ interface. In the case of $MoO_3$-doped TPD [Fig. 4.9(b)], a higher photocurrent is generated owing to the formation of a built-in potential due to the pn-heterojunction at the TPD/$C_{60}$ interface. The cases of NPD and CBP can also be similarly explained. Therefore, we concluded that the observed photovoltaic properties that were attributable to the $MoO_3$ doping could be reasonably explained by a positive shift of $E_F$ and a decrease in the resistance of the HTM.

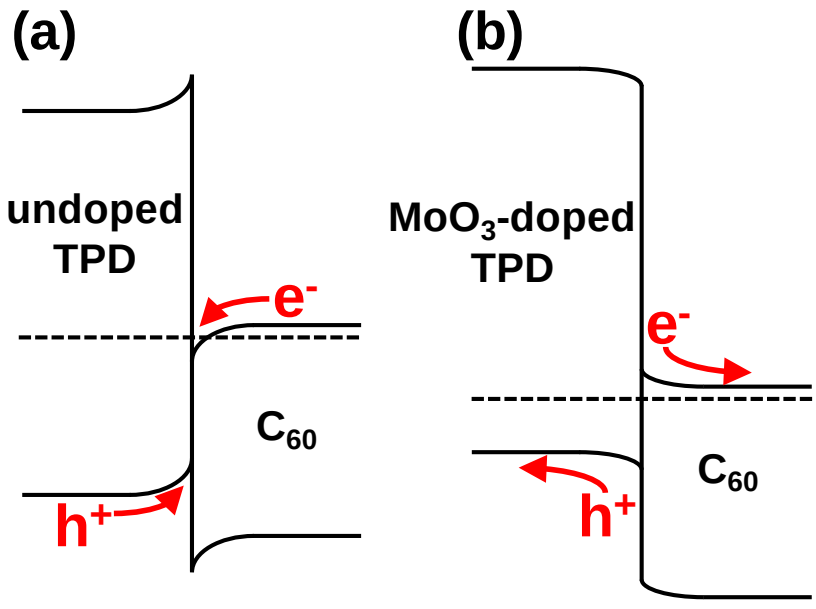


Fig. 4.9. The energy structure of a TPD/$C_{60}$ interface after contact for undoped (a) and $MoO_3$-doped TPD (b).

## 4.4 Conclusion

The photovoltaic characteristics of heterojunction cells incorporating 300-nm-thick hole-transporting films were improved by $MoO_3$ doping owing to the decrease in cell resistance and the formation of built-in potentials. The present doping technique could lead to the development of a new type of photovoltaic cells incorporating thick codeposited films composed of HTM and $C_{60}$ that can absorb the entire incident solar light.

## 4.5 References

1) Y. Lin, Y. Li, and X. Zhan, *Chem. Soc. Rev*., **41**, 4245 (2012).

2) H. Spanggaard and F. C. Krebs, *Sol. Energy Mater. Sol. Cells*, **83**, 125 (2004).

3) H. Hoppe and N. S. Sariciftci, *J. Mater. Res*., **19**, 1924 (2004).

4) K. L. Mutolo, E. I. Mayo, B. P. Rand, S. R. Forrest, and M. E. Thompson, *J. Am. Chem. Soc*., **128**, 8108 (2006).

5) N. M. Kronenberg, M. Deppisch, F. Wurthner, H. W. A. Lademann, K. Deing, and K. Meerholz, *Chem. Commun*., 6489 (2008).

6) J. Sakai, T. Taima, and K. Saito, *Org. Electron*., **9**, 582 (2008).

7) S. Wang, E. I. Mayo, M. D. Perez, L. Griffe, G. Wei, P. I. Djurovich, S. R. Forrest, and M. E. Thompson, *Appl. Phys. Lett*., **94**, 233304 (2009).

8) D. Fujishima, H. Kanno, T. Kinoshita, E. Maruyama, M. Tanaka, M. Shirakawa, and K. Shibata, *Sol. Energy Mater. Sol. Cells*, **93**, 1029 (2009).

9) C. J. Brabec, A. Cravino, D. Meissner, N. S. Sariciftci, T. Fromherz, M. T. Rispens, L. Sanchez, and J. C. Hummelen, *Adv. Funct. Matter*., **11**, 374 (2001).

10) C. Adachi, S. Tokito, T. Tsutsui, and S. Saito, *Jpn. J. Appl. Phys*., **27**, L269 (1988).

11) S. A. Van Slyke, C. H. Chen, and C. W. Tang, *Appl. Phys. Lett*., **69**, 2160 (1996).

12) D. F. O'Brien, M. A. Baldo, M. E. Thompson, and S. R. Forrest, *Appl. Phys. Lett*., **74**, 442 (1999).

13) M. Zhang, H. Wang, and C. W. Tang, *Appl. Phys. Lett*., **97**, 143503 (2010).

14) K. Sakai and M. Hiramoto, *Mol. Cryst. Liq. Cryst*., **491**, 284 (2008).

15) W. E. Spear and P. E. Lecomber, *Solid State Commun*., **17**, 1193 (1975).

16) M. Kubo, K. Iketaki, T. Kaji, and M. Hiramoto, *Appl. Phys. Lett*., **98**, 073311 (2011).

17) M. Kubo, T. Kaji, and M. Hiramoto, *AIP Adv*., **1**, 032177 (2011).

18) Y. Shinmura, M. Kubo, N. Ishiyama, T. Kaji, and M. Hiramoto, *AIP Adv*., **2**, 032145 (2012).

19) J. Blochwitz, M. Pfeiffer, T. Fritz, and K. Leo, *Appl. Phys. Lett*., **73**, 729 (1998).

20) K. Walzer, B. Maennig, M. Pfeiffer, and K. Leo, *Chem. Rev*., **107**, 1233 (2004).

21) M. Kroger, S. Hamwi, J. Meyer, T. Riedl, W. Kowalsky, and A. Kahn, *Org. Electron*., **10**, 932 (2009).

22) M. Zhang, H. Wang, and C. W. Tang, *Appl. Phys. Lett*., **99**, 213506 (2011).

# Chapter 5:
# Mapping of Band-bending for Doped $C_{60}$ Films

"Mapping of Band-Bending for Doped $C_{60}$ Films", Yusuke Shinmura, Tadashi Yoshioka, Toshihiko Kaji, and Masahiro Hiramoto, *Appl. Phys. Express.*, **7**, 071601 (2014).

## Abstract

Mapping of the band-bending that occurs at the interfaces between fullerene ($C_{60}$) films doped with either cesium carbonate ($Cs_2CO_3$) as a donor or molybdenum oxide ($MoO_3$) as an acceptor and indium tin oxide electrodes was performed by using a Kelvin probe. The carrier concentrations determined from the depletion layer widths coincided well with those obtained from the capacitance-voltage characteristics. An ionization efficiency of 10% was determined for the molecularly dispersed dopant ($Cs_2CO_3$) in $C_{60}$, which is significantly less than the 100% for phosphorus in Silicon.

## 5.1 Introduction

Organic photovoltaic cells have been intensively studied and developed.[1-5] Developments similar to that for inorganic photovoltaic cells[6] have included *pn*-control, which is a powerful technique to create a built-in potential and to decrease cell resistance. Suitable dopants for organic semiconductors, such as tetrafluoro-tetracyano-quinodimethane ($F_4$-TCNQ)[7] and molybdenum oxide ($MoO_3$)[8], have been developed. We have recently reported *pn*-control and the fabrication of *pn*-homojunctions in fullerene ($C_{60}$)[9-11] and in metal-free phthalocyanine[12] by doping with cesium carbonate ($Cs_2CO_3$) as a donor and with $MoO_3$ as an acceptor. We have also reported *pn*-control and the fabrication of *pn*-homojunctions and tandem cells simply by doping codeposited films composed of $C_{60}$ and α-sexithiophene.[13,14]

To engineer an energetic structure within the cells requires strict control of the carrier concentration by adjustment of the doping concentration. In this study, a band-mapping method using a Kelvin probe was adopted to evaluate carrier concentration (Fig. 5.1).[11] When doped organic semiconductors are in contact with indium tin oxide (ITO) electrodes, the Fermi level ($E_F$) is aligned. Accordingly, the vacuum level ($E_{VAC}$) is bent and the value of the work function, which is defined as the difference between $E_{VAC}$ and $E_F$ (red double-headed arrows, Fig. 5.1), changes with the thickness of the films. Thus, band-bending with a change in the thickness of doped organic semiconductor films can be directly mapped (Fig. 5.1, lower) by measuring the work function with a Kelvin probe (Fig. 5.1, middle). The band-bending gives the depletion layer width ($W_{dep}$) and built-in potential ($V_{bi}$). The carrier concentration (N) can be obtained using the equation $W_{dep} = (2\varepsilon\varepsilon_0 V_{bi}/eN)^{1/2}$,[15] where ε, $\varepsilon_0$, and e are the relative dielectric constant, the dielectric constant of a vacuum, and the elementary

charge. Band bending for various doped organic semiconductors have been investigated by using ultraviolet and x-ray photoemission spectroscopy and Kelvin probe.[16-21] However, systematic investigation on the relationship between carrier concentration and doping concentration has not been reported. Moreover, systematic investigation on carrier concentration of *p*- and *n*-type doped $C_{60}$ has not been reported because of the absence of *p*-type $C_{60}$ before our work.[9]

In this study, precise determination of the carrier concentration in doped $C_{60}$ films is demonstrated using the Kelvin band-mapping method.

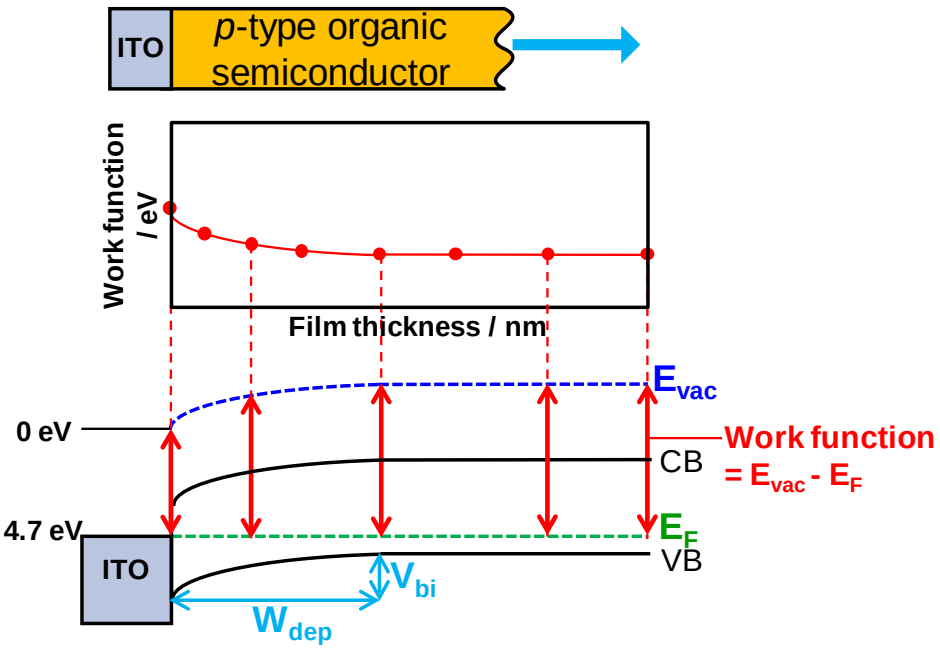


Fig. 5.1 Principle of band-mapping by Kelvin probe. An interface between ITO and *p*-type semiconductor films is shown. The dependence of the work function values (middle figure) corresponding to the red double-headed arrows (lower figure) on the thickness of the organic semiconductor film were measured by Kelvin probe. $E_{vac}$, $E_F$, CB, and VB denote the vacuum level, Fermi level, conduction band, and valence band, respectively.

## 5.2 Experimental

$C_{60}$ (Frontier Carbon Co., Ltd.) was purified to 7N (99.99999%) by sublimation growth of single crystals.[22,23] The acceptor and donor dopants, $MoO_3$ (Alfa Aeser, 99.9995%) and $Cs_2CO_3$ (Aldrich, 99.995%), were used as received without further purification. Doped $C_{60}$ films were deposited by co-evaporation onto ITO glass substrates at a pressure of $10^{-5}$ Pa using an oil–free vacuum evaporator (EpiTech Inc. ET300-6E-HK). Fine tuning of the evaporation rate was performed by computational monitoring (Depoview ULVAC). The evaporation rate of $C_{60}$ was maintained at 0.2 nm $s^{-1}$, and those of the dopants were adjusted from 0.0001 to 0.002 nm $s^{-1}$ to give dopant concentrations of 500 to 10,000 ppm by volume.

The $E_F$ values of $C_{60}$ films on ITO (work function: 4.7 eV) were measured using a Kelvin probe (Riken-Keiki FAC-1). Gold plate whose work function was measured by atmospheric photoelectron spectroscopy (Riken-Keiki, AC-1) was used as a standard for work function measurements by Kelvin probe. Capacitance-voltage (C-V) measurements were performed using Schottky junction cells with the structure of ITO/$MoO_3$ (10 nm)/$MoO_3$-doped $C_{60}$ (1 μm)/bathocuproin (BCP)(15 nm)/Ag (100 nm). A periodical triangular bias was applied to the cell with a function generator (Hokuto Denko HB-102) and the dark current was measured using a picoammeter (Keithley 485). No samples were exposed to air at any time ($H_2O$ < 0.7 ppm, $O_2$ < 0.2 ppm) during film deposition and during the $E_F$ and C-V measurements.

## 5.3 Results and Discussion

### *5.3.1. Mapping of Band-bending for Doped $C_{60}$ Films*

The dependence of the work functions on the thickness of the doped $C_{60}$ films is shown in Fig. 5.2(a). For $Cs_2CO_3$-doping, the work function was shifted toward the negative direction and was close to the lower edge of the conduction band (CB) (3.9 eV). For $MoO_3$-doping, the work function was shifted toward the positive direction and was close to the upper edge of the valence band (VB) (6.4 eV). As the doping concentration increased for both dopants, the film thickness at which the work function shift finished became thinner and the magnitude of the energy shift became larger, i.e., $W_{dep}$ decreased and $V_{bi}$ increased. The *n*- and *p*-type band-bending of $C_{60}$ films doped with $Cs_2CO_3$ (500 ppm) and $MoO_3$ (5,000 ppm), respectively, could be depicted by inverting the observed work function shift (Fig. 5.2(b)). These band-bendings can be fitted by quadratic functions (Fig. 5.2(a)) based on the Poisson equation. $W_{dep}$ values of 24 nm and 21 nm and $V_{bi}$ values of 0.29 V and 0.87 V were obtained, which indicate electron and hole concentrations of $2.5\times10^{17}$ $cm^{-3}$ and $9.6\times10^{17}$ $cm^{-3}$ for 500 ppm-$Cs_2CO_3$ and 5,000 ppm-$MoO_3$, respectively, using the ε value of 4.4 for $C_{60}$.[24)]

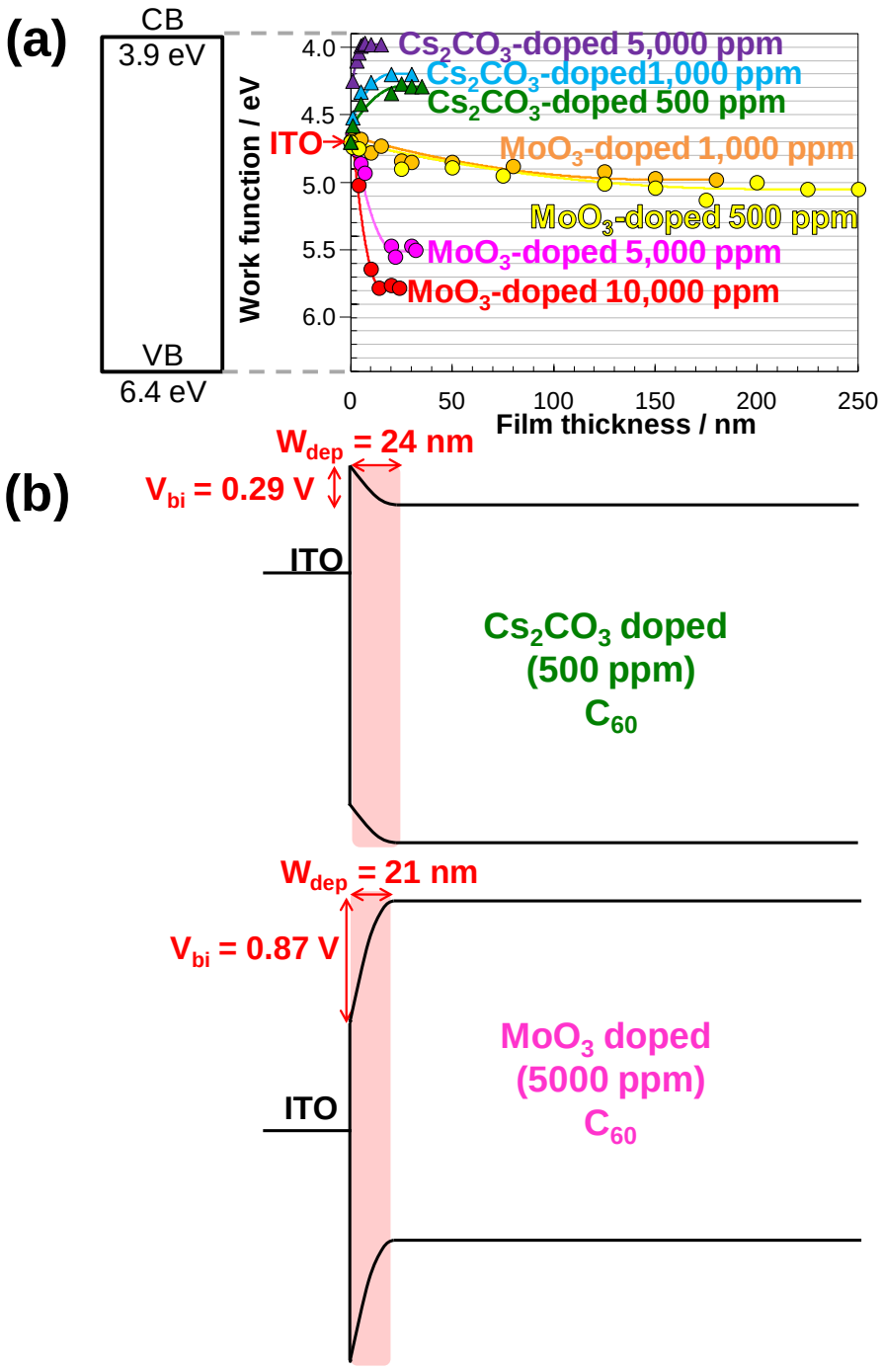


Fig. 5.2 (a) Work function shifts in $C_{60}$ films doped with $Cs_2CO_3$ and $MoO_3$ on ITO substrates. The band-bending can be fitted by quadratic functions (solid lines) based on the Poisson equation. (b) Band-bending for $Cs_2CO_3$-doped (500 ppm) and $MoO_3$-doped (5,000 ppm) $C_{60}$ films.

### *5.3.2. Carrier Concentration and Doping Efficiency*

The accuracy of these carrier concentrations were cross-checked by conventional C-V measurements.[25] The dark current hysteresis of a Schottky junction between 1,000 ppm $MoO_3$-doped $C_{60}$ and a Ag electrode is shown in Fig. 5.3(a).[26] Mott-Schottky plots using differential capacitance ($C_d$) values obtained from the hysteresis $\Delta I$ (V),[27] are shown in Fig. 5.3(b). From the linear part of the plots (broken lines), the carrier concentration for 5,000 ppm-$MoO_3$ doped $C_{60}$ was calculated to be $5\times10^{17}$ $cm^{-3}$, using the equation $C_d^{-2} = 2(V-V_{bi})/eN\varepsilon_0\varepsilon$. This value is relatively consistent with that obtained by the Kelvin method ($9.6\times10^{17}$ $cm^{-3}$). A series of Kelvin probe measurements usually needs time for about 8 hours. Though oxygen and moisture concentration in glove box are extremely low, sensitive surface potential might be affected to during measurements and might cause the difference between Kelvin band-mapping and C-V method.

Figure 5.4(a) shows the dependence of the carrier concentration on the dopant concentration, according to the Kelvin method. The values obtained from the C-V characteristics coincide well with these levels, which supports the accuracy of the carrier concentrations obtained by Kelvin band-mapping. When the $Cs_2CO_3$-doping concentration increased, the carrier (electron) concentration increased rapidly and reached $10^{19}$ $cm^{-3}$ at a doping concentration of 10,000 ppm. In addition, when $MoO_3$ was used as the dopant, the carrier (hole) concentration showed a minimum value of $4.3\times10^{15}$ $cm^{-3}$ at 500 ppm, which increased to $2.7\times10^{18}$ $cm^{-3}$ at 10,000 ppm. The minimum carrier concentration at 500 ppm $MoO_3$-doping indicates that the holes created by $MoO_3$-doping compensate the intrinsic *n*-type nature of $C_{60}$. Similar

phenomenon was observed for doped pentacene.[28] Conductivity change due to the trap filling by doping was also reported.[29]

Figure 5.4(b) shows the doping efficiency, which is defined as the ratio of the induced carrier concentration to the dopant concentration. The doping efficiencies of $Cs_2CO_3$- and $MoO_3$-doping are approximately 10% and 3%, respectively. The doping process can be explained by the formation of a charge-transfer (CT) complex and its subsequent ionization. $Cs_2CO_3$ is a substantial molecule, so that by assuming $Cs_2CO_3$ evaporates molecularly and the rate of CT complex formation with $C_{60}$ is close to unity,[30] the observed doping efficiency of 10% can be regarded as the ionization efficiency, which is significantly less than the value of 100% obtained for the donor dopant Phosphorus (P) in Silicon (Si) at room temperature. The electron orbitals around the positive charge on the ionized donor for P-doping in Si and for $Cs_2CO_3$-doping[31] in $C_{60}$ are shown in Figs. 5.5(a) and (b), respectively. The ε value of Si is 11.9; therefore, the radius of the electron orbital around the positive charge of an ionized donor ($P^+$) is calculated to be 3.3 nm.[32] This is fundamentally the same situation as the Wannier exciton, where the electron is easily liberated from the positive charge by thermal energy at room temperature, and thus the ionization efficiency reaches unity (Fig. 5.5(a)). The only difference to the exciton is that the positive charge is spatially fixed in the crystal lattice. In the case of $Cs_2CO_3$-doping in $C_{60}$, the ε value of $C_{60}$ is 4.4, so that the electron experiences a stronger attractive force from the positive charge. The radius of the Frenkel exciton is only 0.5 nm for $C_{60}$. However, a CT complex is formed by employing $Cs_2CO_3$-doping, i.e., [$Cs_2CO_3^+$-$C_{60}^-$], and the charges are separated on the neighboring molecules (Fig. 5.5(b)). Therefore, this is fundamentally the same situation as the CT exciton, so that the negative charge

on $C_{60}$ can be liberated by thermal energy at room temperature. Thus, significant ionization efficiencies for the electrons of approximately 10% were observed, although they were lower than that for Si. It is assumed that this lower ionization efficiency is due to the stronger attraction force between the smaller electron orbital and the positively ionized donor (Fig. 5.5(b)). In addition, it is probable that ionized donor impurities influence the value of ionization efficiency because the electron orbital is located close to the impurities.

A doping efficiency of 3% was obtained for $MoO_3$ under the assumption that $MoO_3$ forms a trimer ($Mo_3O_9$).[8,33] A similar CT dissociation mechanism to that presented in Fig. 5.5(b) can also be applied in this case; however, the formation of larger $MoO_x$ clusters[34] lowers the efficiency of CT-complex formation, which lowers the total doping efficiency.

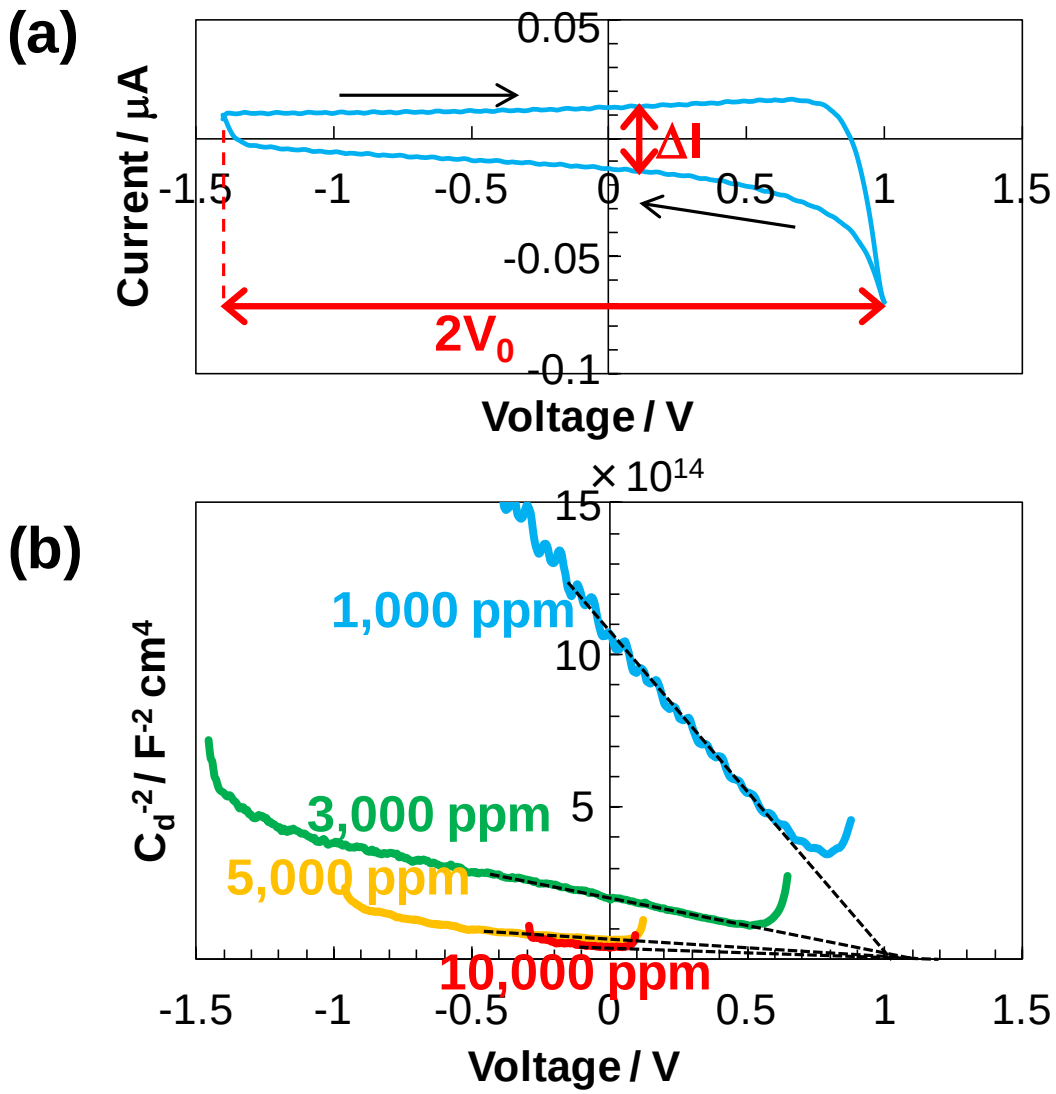


Fig. 5.3 (a) Dark current hysteresis for an ITO/$MoO_3$ (10 nm)/$MoO_3$-doped (1,000 ppm) $C_{60}$ (1 μm)/BCP (15 nm)/Ag cell measured at a scan rate of 3 $Vs^{-1}$. (b) Mott-Schottky plots for cells incorporating $MoO_3$-doped $C_{60}$ films.

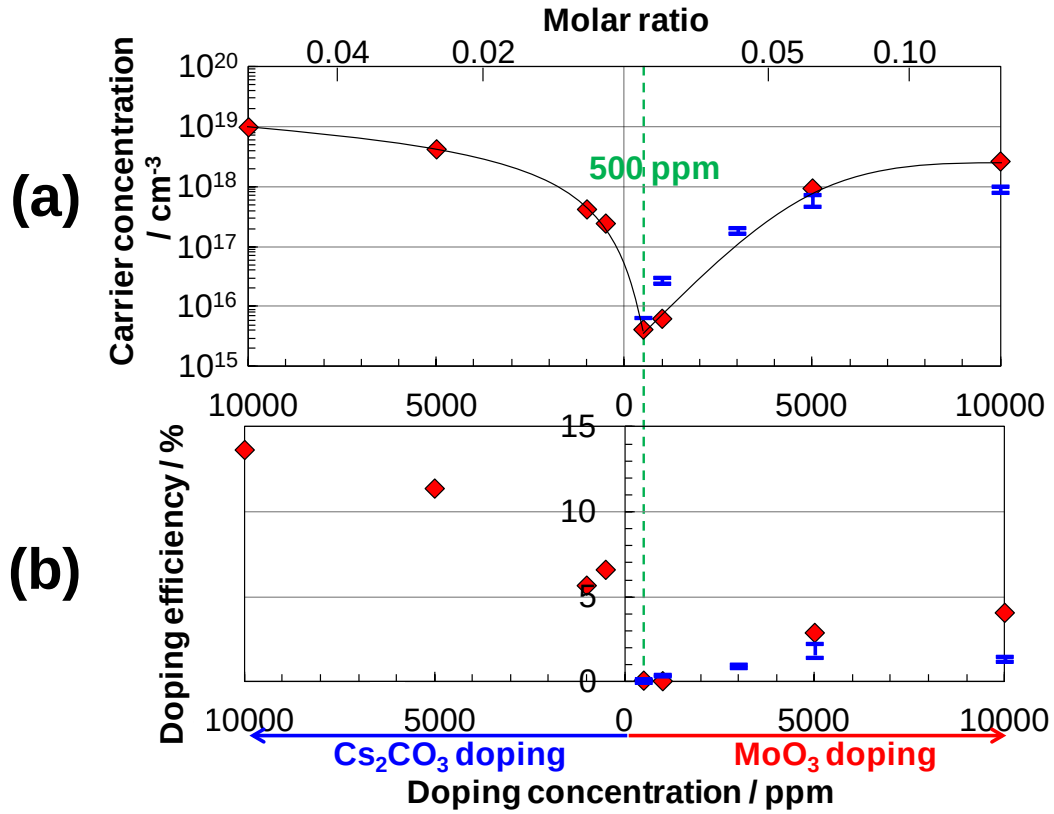


Fig. 5.4 Dependence of (a) carrier concentration and (b) doping efficiency on the doping concentration. The red diamond and blue bars represent the values obtained with the Kelvin probe and from the C-V characteristics, respectively.

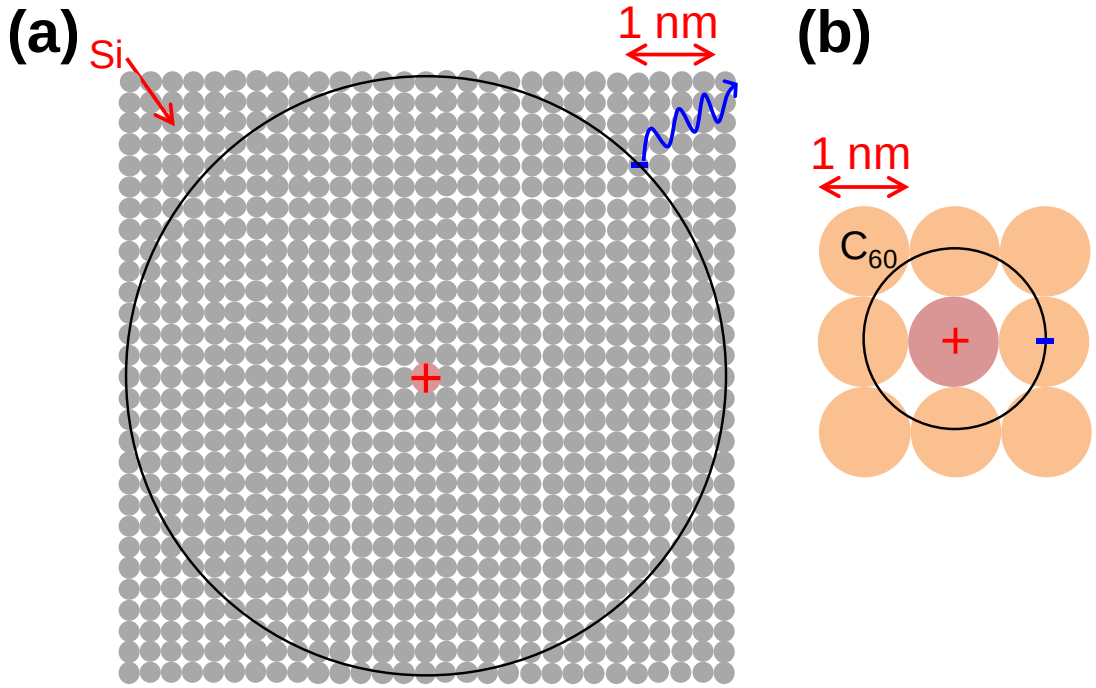


Fig. 5.5 Orbital of an electron around a positive charge on an ionized donor. (a) P-doping in Si. $P^+$ is represented by the red shaded circle. This situation resembles a Wannier exciton. (b) $Cs_2CO_3$-doping in $C_{60}$. $Cs_2CO_3^+$ is represented by the red shaded circle. This situation resembles a CT-exciton.

## 5.4 Conclusion

The carrier concentrations in $C_{60}$ films induced by $Cs_2CO_3$- and $MoO_3$-doping were precisely determined by Kelvin band-mapping. An ionization efficiency of 10% was suggested, which is significantly less than that for Si. Current work is aimed at clarification of the detailed mechanism that determines the ionization efficiency by measurement of the temperature dependence. Kelvin band-mapping is thus demonstrated as an indispensable tool for the design of doped organic photovoltaic cells.

## 5.5 References


1) Y. Lin, Y. Li, and X. Zhan, *Chem. Soc. Rev*., **41**, 4245 (2012).

2) H. Spanggaard and F. C. Krebs, *Sol. Energy Mater. Sol. Cells*, **83**, 125 (2004).

3) H. Hoppe and N. S. Sariciftci, *J. Mater. Res*., **19**, 1924 (2004).

4) C. W. Tang, *Appl. Phys. Lett*., **48**, 183 (1986).

5) M. Hiramoto, H. Fujiwara, and M. Yokoyama, *Appl. Phys. Lett*., **58**, 1062 (1991).

6) W. E. Spear and P. E. Lecomber, *Solid State Commun*., **17**, 1193 (1975).

7) K. Walzer, B. Maennig, M. Pfeiffer, and K. Leo, *Chem. Rev*., **107**, 1233 (2007). and references therein.

8) M. Kröger, S. Hamwi, J. Meyer, T. Riedl, W. Kowalsky, and A. Kahn, *Org. Electron*., **10**, 932 (2009).

9) M. Kubo, K. Iketaki, T. Kaji, and M. Hiramoto, *Appl. Phys. Lett*., **98**, 073311 (2011).

10) M. Kubo, T. Kaji, and M. Hiramoto, *AIP Adv*., **1**, 032177 (2011).

11) N. Ishiyama, M. Kubo, T. Kaji, and M. Hiramoto, *Appl. Phys. Lett*., **101**, 233303 (2012).

12) Y. Shinmura, M. Kubo, N. Ishiyama, T. Kaji, and M. Hiramoto, *AIP Adv*., **2**, 032145 (2012).

13) N. Ishiyama, M. Kubo, T. Kaji, and M. Hiramoto, *Appl. Phys. Lett*., **99**, 133301 (2011).

14) N. Ishiyama, T. Yoshioka, T. Kaji, and M. Hiramoto, *Appl. Phys. Express*, **6**, 012301 (2013).

15) S. M. Sze, Physics of Semiconductor Devices (Wiley, New York, 1969).

16) J. Blochwitz, T. Fritz, M. Pfeiffer, K. Leo, D.M. Alloway, P.A. Lee, and N.R.

Armstrong, *Org. Electron*., **2**, 97 (2001).

17) W. Gao, and A. Kahn, *Org. Electron*., **3**, 53 (2002).

18) C. Chan, W. Gao, and A. Kahn, *J. Vac. Sci. Technol. A*, **22**, 1488 (2004).

19) A. Kahn, W. Zhao, W. Gao, H. Vázquez, and F. Flores, *Chem. Phys*., **325**, 129 (2006).

20) S. Olthof, W. Tress, R. Meerheim, B. Lüssem, and K. Leo, *J. Appl. Phys*., **106**, 103711 (2009).

21) S. Hamwi, J. Meyer, T. Winkler, T. Riedl, and W. Kowalsky, *Appl. Phys. Lett*., **94**, 253307 (2009).

22) M. Hiramoto and K. Sakai, *Mol. Cryst. Liq. Cryst*., **491**, 284 (2008).

23) M. Hiramoto, *Proc. SPIE*, **7052**, 70520H (2008).

24) A. F. Hebard, R. C. Hadon, R. M. Fleming, and A. R. Kortan, *Appl. Phys. Lett*., **59**, 2109 (1991).

25) A. J. Twarowski and A. C. Albrecht, *J. Chem. Phys*., **70**, 2255 (1979).

26) For the ITO/$MoO_3$ (10 nm)/$MoO_3$-doped $C_{60}$ (1 μm)/bathocuproin (BCP) (15 nm)/Ag (100 nm) cell, photovoltaic measurements clearly showed that a Schottky junction was formed at the $C_{60}$/BCP/Ag interface, and an ohmic junction was formed at the ITO/$C_{60}$ interface.

27) Differential capacitance, $C_d$ (V), was calculated using the equation $C_d$ (V) = $\Delta$I (V)/$8V_0$f, where $\Delta$I (V), $V_0$, and f are the difference in the dark current due to hysteresis, the amplitude of the scanning voltage, and the frequency of the periodical triangular bias, respectively.

28) C.K. Chan, and A. Kahn, *Appl. Phys. A*, **95**, 7 (2009).

29) S. Olthof, S. Mehraeen, S. K. Mohapatra, S. Barlow, V. Coropceanu, J. Brédas, S.

R. Marder, and A. Kahn. *Phys. Rev. Lett.*, **109**, 176601 (2012).

30) There is no evidence of $Cs_2CO_3$ dissociation during vacuum evaporation, because a single $Cs_2CO_3$ film is completely transparent.

31) The diameter of a $Cs_2CO_3$ molecule is approximately 1 nm, which is close to that of $C_{60}$ (1 nm).

32) The radius of an electron orbital around a positively ionized donor can be calculated based on the equation expressing the Bohr radius (r), which includes the relative permittivity ($\varepsilon$) and the effective mass of an electron ($m_n^*$), i.e., $r = \varepsilon_0 \varepsilon h^2/\pi m_n^* e^2$.

33) J. Berkowitz, M. G. Inghram, and W. A. Chupka, *J. Chem. Phys*., **26**, 842 (1957).

34) T. H. Lee, B. Lussem, K. Kim, G. Giri, Y. Nishi, and Z. Bao, *ACS Appl. Mater*. *Interfaces*, **5**, 2337 (2013).

# Chapter 6:
# Ionization Sensitization of Doping in Co-deposited Organic Semiconductor Films

"Ionization Sensitization of Doping in Co-deposited Organic Semiconductor Films", Yusuke Shinmura, Yohei Yamashina, Toshihiko Kaji, and Masahiro Hiramoto, *Appl. Phys. Lett.*, **105**, 183306 (2014).

## Abstract

Sensitization of the dopant ionization in co-deposited films of organic semiconductors was found. The ionization rate of cesium carbonate ($Cs_2CO_3$), which acts as a donor dopant in single films of metal-free phthalocyanine ($H_2Pc$) and fullerene ($C_{60}$), was increased from 10% to 97% in a $H_2Pc$:$C_{60}$ co-deposited film. A charge separation superlattice model that includes electron transfer from the conduction band of $H_2Pc$ to that of $C_{60}$, which increases the rate of dopant ionization, is proposed.

## 6.1 Introduction

Controlling the doping in small molecular organic photovoltaic cells[1-5] to create a built-in potential has been developed over the last decade.[6-9] We have reported on the *pn*-control technique and the formation of *pn*-homojunctions using cesium carbonate ($Cs_2CO_3$), which acts as a donor, and molybdenum oxide, which acts as an acceptor for fullerene ($C_{60}$)[10-12] and metal-free phthalocyanine ($H_2Pc$)[13]. A key element for exciton dissociation in organic solar cells is having a co-deposited film comprising two different types of organic semiconductor; therefore, we have also reported on the *pn*-control and formation of *pn*-homojunctions in $C_{60}$:$H_2Pc$ and $C_{60}$:sexithiophene co-deposited films.[14-17]

During the course of these studies, we made accurate estimates of the carrier concentrations generated by impurity doping by means of Kelvin band-mapping,[18] from which we found evidence of higher doping efficiencies for co-deposited films compared to those for the respective single films. Thus, we tried to clarify the reasons for the difference between the doping efficiencies in co-deposited films and single films of organic semiconductors. As a typical case, we chose metal-free phthalocyanine: fullerene ($H_2Pc$:$C_{60}$, $H_2Pc$:$C_{70}$) and metal-free phthalocyanine:perylene pigment ($H_2Pc$:Me-PTC) co-deposited films because of their high capability for exciton dissociation in organic solar cells. Cesium carbonate ($Cs_2CO_3$) and iron chloride ($FeCl_3$) were used as donor and acceptor dopants, respectively.

Here, we report on the notable increases in doping efficiency for *n*-type doped fullerenes:$H_2Pc$ and *p*-type doped Me-PTC:$H_2Pc$ co-deposited films.

## 6.2 Experimental

Fullerenes (Frontier Carbon Co., Ltd.; $C_{60}$: nanom purple TL, $C_{70}$: nanom orange STH), $H_2Pc$ (Dainippon Ink & Chemicals, Inc., Fastogen Blue EP-101), and perylene pigment (Me-PTC, Fig. 6.1) were purified to 7N (99.99999%) by single-crystal sublimation.[6,19,20] The donor dopant, $Cs_2CO_3$ (Aldrich, 99.995%), and the acceptor dopant, $FeCl_3$ (Aldrich, 99.99%), were used without further purification. Doped single and co-deposited films were fabricated by means of co-evaporation from three sources onto indium tin oxide (ITO) glass substrates at a pressure of $10^{-5}$ Pa using an oil–free vacuum evaporator (EpiTech Inc., ET300-6E-HK). Fine tuning of the deposition rate was performed using a quartz crystal microbalance equipped with a computer monitoring system (Depoview, ULVAC). The deposition rate for the organic semiconductors was kept to 0.1 nm $s^{-1}$ and those for the dopants were adjusted from $10^{-5}$ to $2\times10^{-3}$ nm $s^{-1}$ to give doping concentrations from 0.0002 to 0.05 in molar ratio (MR), i.e., 50 to 10,000 ppm in volume.

In order to determine the carrier concentrations created by doping, the band bending at the ITO/semiconductor interface was mapped by measuring the film thickness dependence of the work function using a Kelvin probe (Riken-Keiki, FAC-1). The detailed principle of Kelvin band-mapping is reported in Ref. 21. From the band bending, the depletion layer width ($W_{dep}$) and the built-in potential ($V_{bi}$) can be determined. Carrier concentration (N) can be calculated by Eq. (1).

$$N = 2\varepsilon\varepsilon_0 V_{bi}/eW_{dep}^{2} \quad (1)$$

Here, $\varepsilon$, $\varepsilon_0$, and e are the relative dielectric constant, the dielectric constant in vacuum, and the elementary charge, respectively. The samples were not exposed to air at any time during fabrication and the measurements ($H_2O$ < 0.7 ppm, $O_2$ < 0.2 ppm).

## 6.3 Results and Discussion

### *6.3.1. Sensitization of Doping in Co-deposited Films*

Fig. 6.1 shows an energy band diagram of the organic semiconductors and dopants. $Cs_2CO_3$ can donate an electron to lowest unoccupied molecular orbital (LUMO) of $H_2Pc$ (3.2 eV) and the fullerenes (3.9 eV)[22], which is measured by near ultraviolet inverse photoemission spectroscopy,[23] and thus acts as donor since its work function is located at a shallower position (2.96 eV). In practice, by $Cs_2CO_3$-doping (MR=0.02), the Fermi level ($E_F$) shifted toward the unoccupied density of states (DOS) and reached to 3.97, 4.00, and 3.48 eV for $C_{60}$, $C_{70}$, and $H_2Pc$, respectively. Both fullerenes and $H_2Pc$ became *n*-type. On the other hand, $FeCl_3$ can withdraw an electron from highest occupied molecular orbital (HOMO) of $H_2Pc$ (5.1 eV) and Me-PTC (5.4 eV) and acts as an acceptor since its work function is located at a deeper position (5.52 eV). By $FeCl_3$-doping (MR=0.03), $E_F$ shifted toward the occupied DOS and reached to 4.72 and 5.04 eV for $H_2Pc$ and Me-PTC, respectively. Both $H_2Pc$ and Me-PTC became *p*-type.

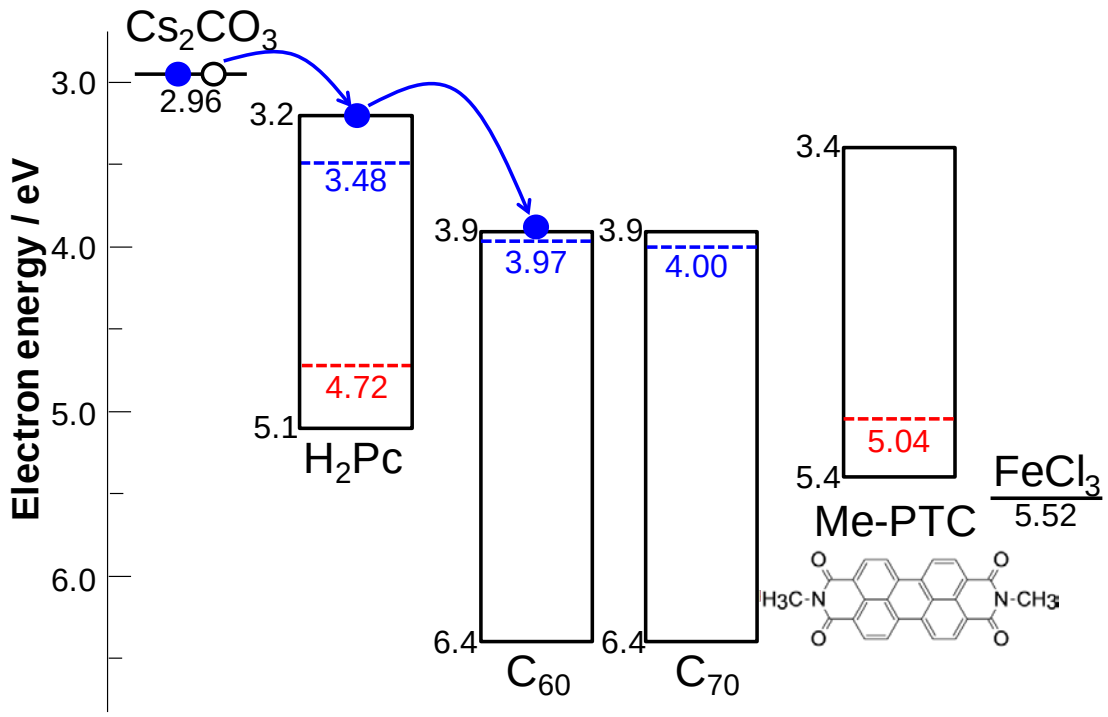


Fig. 6.1 Energy diagrams of organic semiconductors. The work functions with the donor ($Cs_2CO_3$) and acceptor ($FeCl_3$) dopants are also shown. $E_F$s of $C_{60}$, $C_{70}$, and $H_2Pc$ films doped with $Cs_2CO_3$ (MR=0.02) are shown by broken blue lines. $E_F$s of $H_2Pc$ and Me-PTC films doped with $FeCl_3$ (MR=0.03) are shown by broken red lines.

Fig. 6.2(a) shows the film thickness dependence of the work function for $Cs_2CO_3$-doped $H_2Pc$:$C_{60}$ (1:1 in volume) co-deposited films (red circles) and the respective $Cs_2CO_3$-doped single films of $C_{60}$ (orange diamonds) and $H_2Pc$ (blue triangles). The shifts in work function due to the band-bending by doping are fitted by quadratic functions based on the Poisson equation (solid curves), which excludes the effect of a dipole layer of a few nanometers thickness in the vicinity of the ITO electrode[24]. Clearly, the depletion layer width ($W_{dep}$) in the $H_2Pc$:$C_{60}$ co-deposited film has shrunk to 10 nm from 20 and 30 nm in the respective $C_{60}$ and $H_2Pc$ single films (arrows). This observation is a sign of an increase in the carrier concentration. From Eq. (1), concentrations of $3.2\times10^{18}$, $4.3\times10^{17}$, and $4.6\times10^{17}$ $cm^{-3}$ were obtained for the co-deposited film and the $C_{60}$ and $H_2Pc$ films, respectively. By mixing $C_{60}$ and $H_2Pc$, the number of carriers created by $Cs_2CO_3$-doping was increased by a factor of around 10.

Essentially the same result was obtained for the $H_2Pc$:Me-PTC (1:1 in volume) system (Fig. 6.2(b)). $FeCl_3$ acting as an acceptor was introduced into a $H_2Pc$:Me-PTC co-deposited film and its respective Me-PTC and $H_2Pc$ single films. Concentrations of $8.7\times10^{18}$, $5.3\times10^{16}$, and $6.9\times10^{17}$ $cm^{-3}$ were obtained for the co-deposited film and the Me-PTC and $H_2Pc$ films, respectively. By mixing Me-PTC and $H_2Pc$, the number of carriers created by $FeCl_3$-doping was also increased increased by a factor of about 100 for Me-PTC.

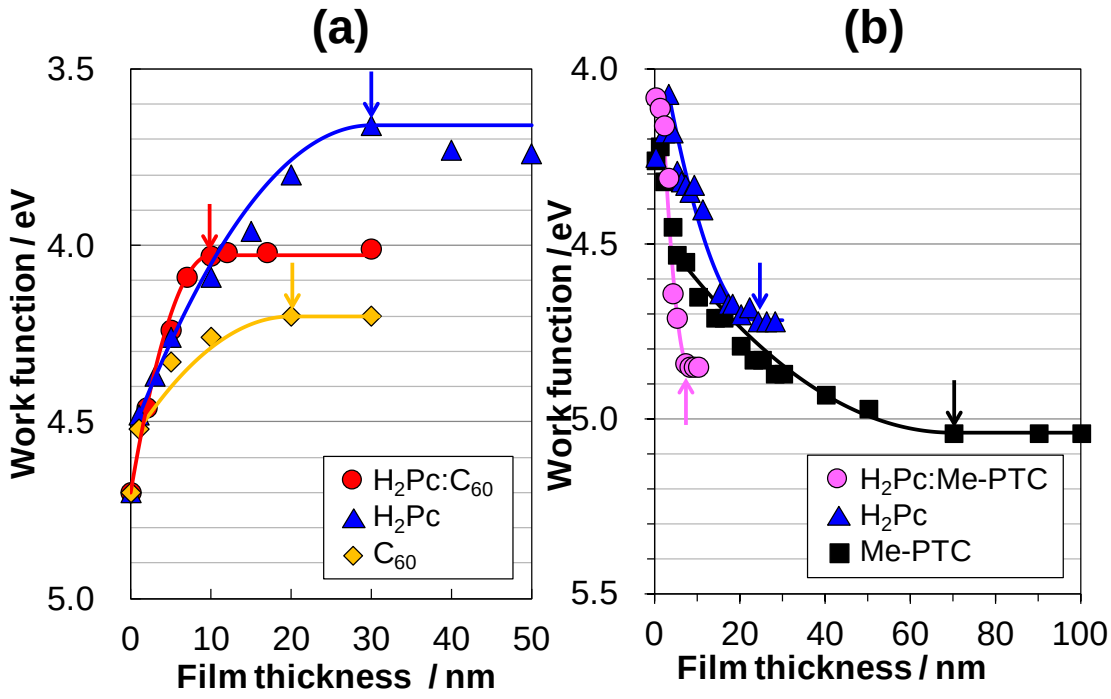


Fig. 6.2. Film thickness dependences of the work function. (a) $H_2Pc$:$C_{60}$ (1:1) co-deposited film (red circles) and its component single $C_{60}$ (orange diamonds) and $H_2Pc$ (blue triangles) films. The $Cs_2CO_3$ doping concentration for all the films was MR=0.005. (b) $H_2Pc$:Me-PTC (1:1) co-deposited film (pink circles) and its component single Me-PTC (black squares) and $H_2Pc$ (blue triangles) films. The $FeCl_3$ doping concentration for all the films was MR=0.03. The depths of the band-bending are indicated by arrows. The solid curves are quadratic fits to the band-bending.

Fig. 6.3 shows the dependence of the carrier concentration and the doping efficiency on the doping concentration for $H_2Pc$:$C_{60}$ (a)(b) and $H_2Pc$:$C_{70}$ (c)(d) co-deposited films and their component films. The doping efficiency is defined by the ratio of the carrier concentration created to the molecular concentration of $Cs_2CO_3$. Obviously, the carrier concentration is an order of magnitude larger for the co-deposited films (Fig. 6.3(a)(c), red and purple curves) compared to the respective component single films (Fig. 6.3(a)(c), orange, green and blue curves). The doping efficiencies of single films of $C_{60}$, $C_{70}$, and $H_2Pc$ are around 10% (Fig. 6.3(b)(d), orange diamonds, green diamonds, blue triangles). In contrast, the doping efficiencies of the co-deposited films of $H_2Pc$:$C_{60}$ and $H_2Pc$:$C_{70}$ are around 50% (Fig. 6.3(b)(d), red and purple circles). Thus, we conclude that the doping efficiency was significantly enhanced in the co-deposited films.

Essentially the same phenomenon was observed for acceptor doping. By combining $H_2Pc$ and Me-PTC, a considerable increase in doping efficiency to 30% was obtained from the 2% and 0.2% efficiencies obtained for $H_2Pc$ and Me-PTC films, respectively (Table 6.I).[25] Thus, we concluded that the increase in doping efficiency is universal and irrespective of whether the doping is donor or acceptor doping.

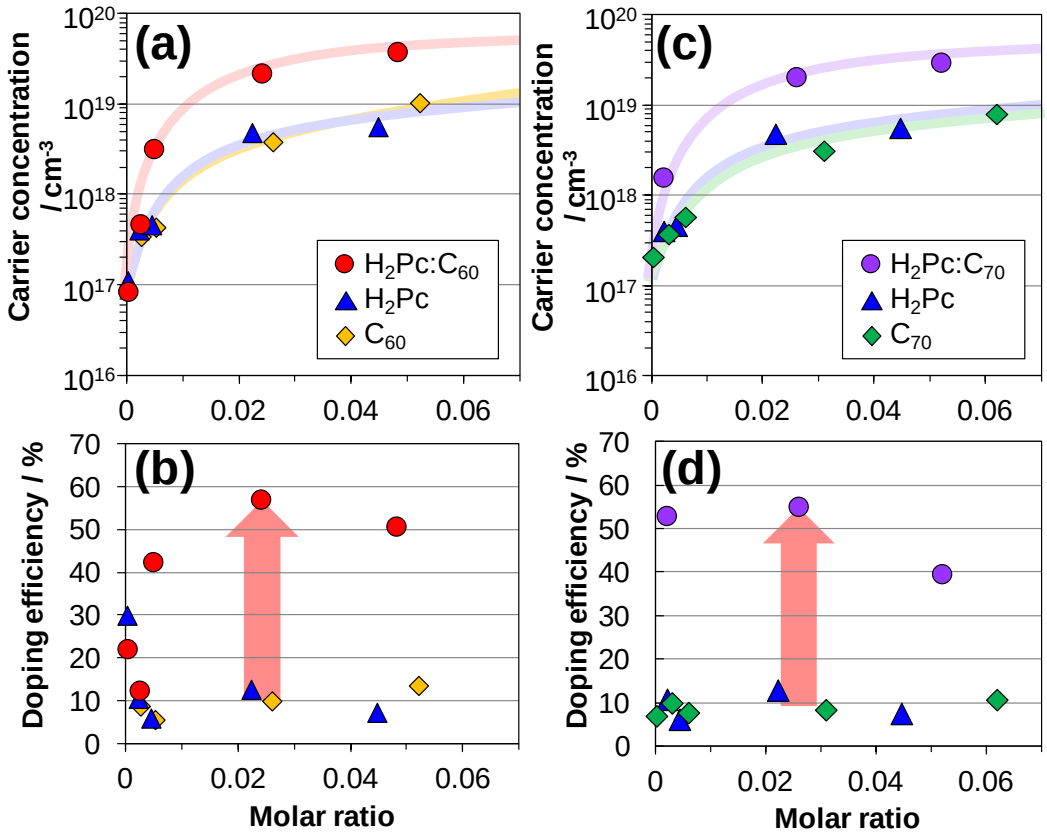


Fig. 6.3. Dependence of carrier concentration and doping efficiency on $Cs_2CO_3$ doping concentration for $H_2Pc$:$C_{60}$ (a)(b) and $H_2Pc$:$C_{70}$ (c)(d) co-deposited films and their component films.

Table 6.I. Ionization rates (doping efficiencies) of co-deposited films and their component single films and the factor by which the doping sensitization has increased for donor-doped $H_2Pc$:$C_{60}$ and acceptor-doped $H_2Pc$:Me-PTC systems

| | Ionization rate (Doping efficiency) / % | | | | Rate of multiplication |
|---|---|---|---|---|---|
| | Co-deposited films | Single films | | | |
| | | $H_2Pc$ | $C_{60}$ | Me-PTC | |
| Donor doping ($H_2Pc$:$C_{60}$ system) | **50** | **10** | **10** | **-** | **10** |
| Acceptor doping ($H_2Pc$:Me-PTC system) | **30** | **2** | **-** | **0.2** | **300** |

### *6.3.2. Mechanisms of the Sensitization*

The doping process for $Cs_2CO_3$ in $H_2Pc$ can be explained by the charge-transfer (CT) complex, i.e., the formation of $H_2Pc^-$---$Cs_2CO_3^+$ and its ionization.[13] Here, the positive charge on the $Cs_2CO_3^+$ is a spatially fixed positive ion, i.e., an ionized donor. The negative charge on the $H_2Pc$ is liberated by thermal energy and acts as a free electron in the conduction band (Fig. 6.4(a)). Thus, the doping efficiency can be expressed by the product of the rates of the CT complex formation and ionization. Since $Cs_2CO_3$ exists as a molecule having a structure of Cs-O-(C=O)-O-Cs, it is reasonable to assume that $Cs_2CO_3$ evaporates molecularly and the rate of the CT complex formation with $H_2Pc$, $C_{60}$ and $C_{60}$:$H_2Pc$ films is close to unity.[26] Thus, we consider that the observed doping efficiency represents the ionization efficiency.

We propose a charge separation superlattice model to explain the enhancement in ionization rate. Fig. 6.4(a) shows the energy structures of $H_2Pc$ and $C_{60}$ single films before contact. The lower edge of the conduction band (CB) was determined by inverse photoelectron spectroscopy.[23] The activation energy ($\Delta E_D$) of 0.12 eV was determined from the ionization rate of 10%.[27] Before contact, 10% of the electrons are excited to the conduction band and the other electrons are captured by donor levels (Fig. 6.4(a)).

By making contact with $C_{60}$, since the electron transfer from the conduction band of $H_2Pc$ to that of $C_{60}$ (Fig. 6.4(a), blue arrow) occurs accompanied with energetic relaxation (0.7 eV), the electron concentration in $H_2Pc$ decreases. Due to the shift in equilibrium, the electron liberation from the donor levels accelerates, i.e., the ionization rate for donors increases only in the $H_2Pc$ region. Taking the molecular ratio of the $H_2Pc$:$C_{60}$ co-deposited film (1:1) into consideration, the ionization rate of the $H_2Pc$

region in the co-deposited film can be estimated to be 100% while that in the $C_{60}$ region is unchanged (10%), since the observed ionization rate of 55% for the $H_2Pc$:$C_{60}$ co-deposited film can be obtained by calculation, i.e., 100%×0.5 + 10%×0.5 = 55%. Thus, we concluded that for the $H_2Pc$ region, the ionization rate increased from 10 to 100%, an increase of a factor of 10 (Table I). The ionization rate of 100% supports the assumption that the rate of formation of the CT complex is unity.

Fig. 6.4(b) and 6.4(c) show the 3-dimensional and cross sectional energy structures of charge separating $H_2Pc/C_{60}$ superlattices after contact, respectively. Due to the faster liberation of electrons from the donors, all the donors in the $H_2Pc$ region of the co-deposited film positively ionize and the energy band of $H_2Pc$ is bent to a depth of 3.3 nm.[28] In this model, the $H_2Pc$ regions act as electron supplying layers to the $C_{60}$ regions. The $C_{60}$ regions act as electron transporting highways. Based on this model, we expect that the total ionization rate in $H_2Pc$:$C_{60}$ co-deposited films would increase further by increasing the $H_2Pc$ ratio.

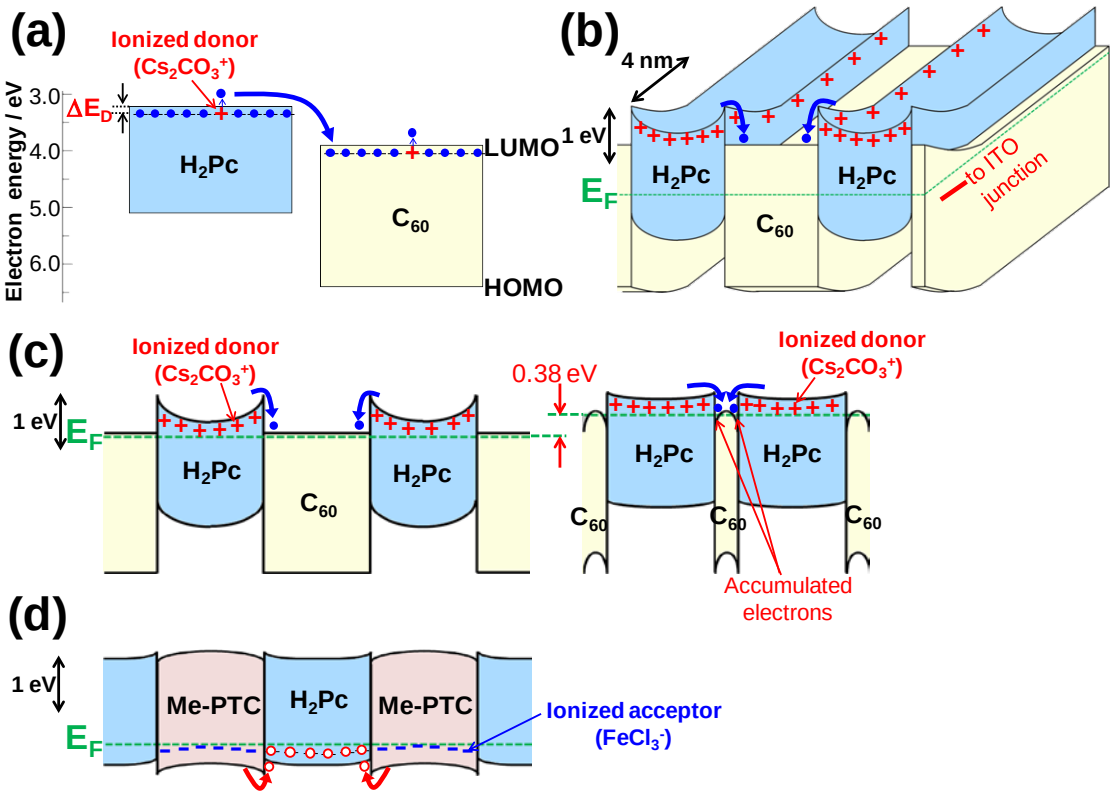


Fig. 6.4 (a) Energy diagrams of $Cs_2CO_3$-doped $H_2Pc$ and $C_{60}$ single films before contact. $\Delta E_D$ denotes the activation energy of the donors. (b) 3-dimensional energy structure for a $Cs_2CO_3$-doped $H_2Pc/C_{60}$ superlattice formed at an ITO interface after contact. (c) Cross sectional energy structure of a $Cs_2CO_3$-doped $H_2Pc/C_{60}$ superlattice after contact, which is cut in parallel to ITO interface at after the end of band-bending by ITO. The $H_2Pc$:$C_{60}$ ratios are 1:1 (left) and 99:1 (right). The grey shaded parts show the accumulated electrons in $C_{60}$. (d) Cross sectional energy structure of a $FeCl_3$-doped Me-PTC/$H_2Pc$ superlattice after contact. The energy relationships are depicted on the same scale in all figures.

Fig. 6.5(a) and 6.5(b) show the Kelvin band-mapping results and observed ionization rates for different ratios of $H_2Pc$ in $H_2Pc$:$C_{60}$ co-deposited films doped with $Cs_2CO_3$. As the $H_2Pc$ ratio increases, the ionization rate increases proportionally, with good agreement to the calculated line (broken red line, Fig. 6.5(b)),[29] and reached 97% at a $H_2Pc$:$C_{60}$ ratio of 99:1.

Interestingly, the positions of $E_F$ after band-bending systematically shift in the negative direction with decreasing $C_{60}$ (Fig. 6.5(a)). This is a sign that there is a more concentrated accumulation of liberated electrons in the thinner $C_{60}$ regions, which lifts $E_F$ by 0.38 eV for $H_2Pc$:$C_{60}$ (99:1) (compare the left and right plots in Fig. 6.4(c)). Since there should be a vast number of free electrons in the $C_{60}$ conduction band under $E_F$, we assume that a confined electron gas exists on the $C_{60}$ sides of the $H_2Pc$/$C_{60}$ interfaces, similar to that reported for inorganic AlGaAs/GaAs superlattices.[30] This systematic observation also supports the proposed charge separation superlattice model.

For acceptor doping, the opposite mechanism occurs (Fig. 6.4(d)). Being in contact with $H_2Pc$, the holes in the valence band of Me-PTC energetically relax (0.3 eV) to the valence band of $H_2Pc$ (red arrows) and their concentration in Me-PTC decreases. As a result, there is faster liberation of holes from the acceptors. For the Me-PTC region, the ionization rate increases from 0.2 to 60%, a 300 fold increase (Table I).

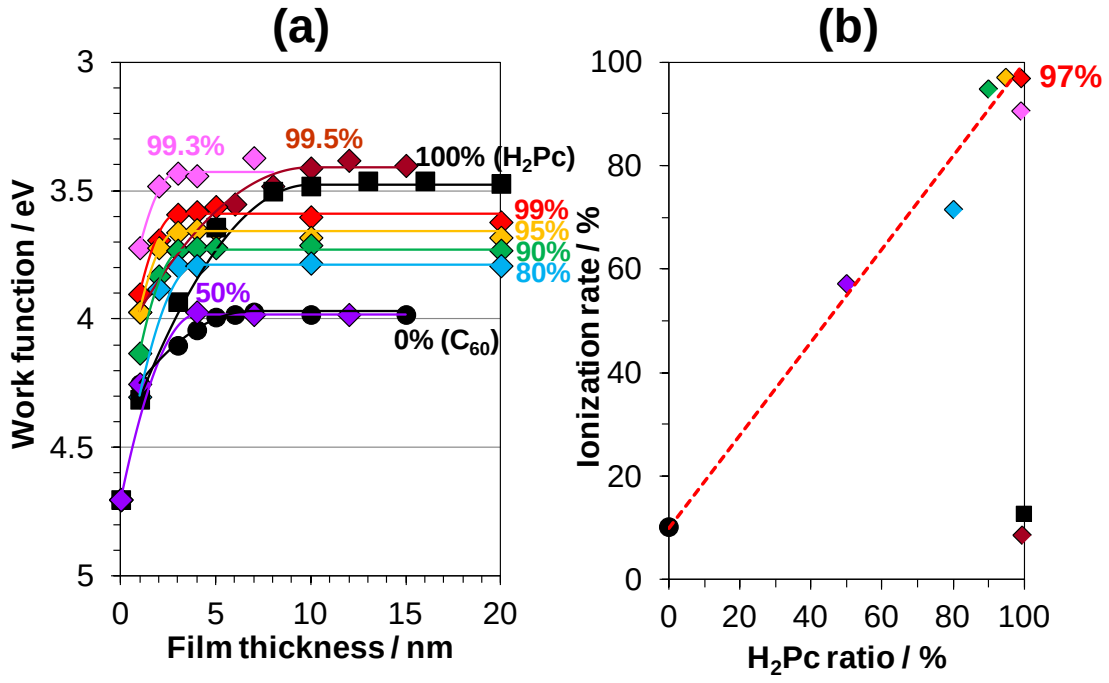


Fig. 6.5 (a) Dependence of work function on the film thickness for various ratios of $H_2Pc$ in $H_2Pc$:$C_{60}$ co-deposited films doped with $Cs_2CO_3$ (MR=0.02). (b) Ionization rate for various ratios of $H_2Pc$ in $H_2Pc$:$C_{60}$ co-deposited films. Calculated ionization rate is shown by the broken red line.

Direct ionization processes might occur when the ionized donor is located just at the $C_{60}/H_2Pc$ molecular interface (Fig. 6.6). For donors in the single $C_{60}$ and $H_2Pc$ regions, the activation energy, i.e., the binding energy of an electron around a positively ionized donor ($Cs_2CO_3^+$) ($\Delta E_D$) is 0.12 eV (Fig. 6.4(a)) [27], which corresponds to an electron orbital radius of 1.6 nm (Fig. 6.6, blue circles).[31] This situation resembles CT exciton. The only difference is that the positive charge of the ionized donor is fixed. For donors just on the $H_2Pc$ side of the $C_{60}/H_2Pc$ molecular interface (Fig. 6.6, center), a cascade-like second electron transfer from the LUMO of the $H_2Pc$ molecule to that of the $C_{60}$ molecule occurs (see Fig. 6.1). Compared to the binding energy ($\Delta E_D$) of 0.12 eV, the relaxation energy of 0.58 eV[32] is sufficient to liberate electrons by increasing the electron orbital radius to over 6.5 nm which has a binding energy comparable to the thermal energy of room temperature (kT = 0.026 eV) (Fig. 6.6, red semicircle).[33] This situation resembles Wanner exciton. It should be noted that a similar electron transfer from $H_2Pc$ (D) to $C_{60}$ (A) (Fig. 6.1), is utilized in organic solar cells to increase exciton dissociation, i.e., so-called donor/acceptor (D/A) sensitization. Thus, the present doping sensitization phenomenon can be regarded as analogous to D/A sensitization for dopant ionization.

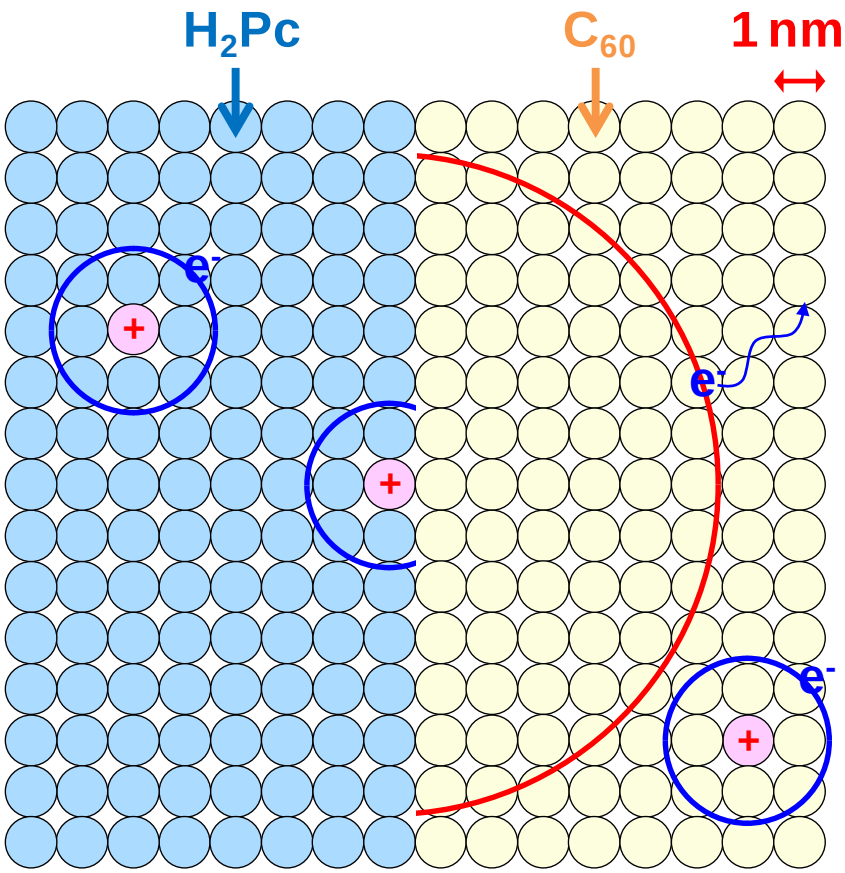


Fig. 6.6 Schematic illustration of electron orbits around a positive ionized donor. The blue circles are those for donors in single $C_{60}$ and $H_2Pc$ regions. The red semicircle is that for a donor just on the $H_2Pc$ side of the $H_2Pc/C_{60}$ molecular interface.

## *6.4 Conclusion*

In conclusion, sensitization of the ionization for both *n*- and *p*-type doping in organic semiconductor co-deposited films was observed. A significantly high ionization efficiency of 97%, comparable to that for silicon (100%), was achieved. The present phenomenon can be reasonably explained based on the charge separation superlattice model.

## 6.5 References

1) Y. Lin, Y. Li, and X. Zhan, *Chem. Soc. Rev*., **41**, 4245 (2012).

2) H. Spanggaard and F. C. Krebs, *Sol. Energy Mater. Sol. Cells*, **83**, 125 (2004).

3) H. Hoppe and N. S. Sariciftci, *J. Mater. Res*., **19**, 1924 (2004).

4) C. W. Tang, *Appl. Phys. Lett.*, **48**, 183 (1986).

5) M. Hiramoto, H. Fujiwara, and M. Yokoyama, *Appl. Phys. Lett.*, **58**, 1062 (1991).

6) M. Hiramoto, M. Kubo, Y. Shinmura, N. Ishiyama, T. Kaji, K. Sakai, T. Ohno, and M. Izaki, *Electronics*, **3**, 351 (2014).

7) B. Lüssem, M. Riede, and K. Leo, *Phys. Status Solidi A*, **210**, 9 (2013) and references therein.

8) C.K. Chan, W. Zhao, A. Kahn, and I. G. Hill, *Appl. Phys. Lett.*, **94**, 203306 (2009).

9) K. Walzer, B. Maennig, M. Pfeiffer, and K. Leo, *Chem. Rev.*, **107**, 1233 (2007) and references therein.

10) M. Kubo, K. Iketaki, T. Kaji, and M. Hiramoto, *Appl. Phys. Lett.*, **98**, 073311 (2011).

11) M. Kubo, T. Kaji, and M. Hiramoto, *AIP Adv*., **1**, 032177 (2011).

12) N. Ishiyama, M. Kubo, T. Kaji, and M. Hiramoto, *Appl. Phys. Lett*., **101**, 233303 (2012).

13) Y. Shinmura, M. Kubo, N. Ishiyama, T. Kaji, and M. Hiramoto, *AIP Adv.*, **2**, 032145 (2012).

14) N. Ishiyama, M. Kubo, T. Kaji, and M. Hiramoto, *Appl. Phys. Lett*., **99**, 133301 (2011).

15) N. Ishiyama, T. Yoshioka, T. Kaji, and M. Hiramoto, *Appl. Phys. Express*, **6**, 012301 (2013).

16) M. Kubo, T. Kaji, and M. Hiramoto, *Appl. Phys. Lett*., **103**, 263303 (2013).

17) M. Kubo, Y. Shinmura, N. Ishiyama, T. Kaji, and M. Hiramoto, *Mol. Cryst. Liq. Cryst*., **581**, 13 (2013).

18) H. Ishii, N. Hayashi, E. Ito, Y. Washizu, K. Sugi, Y. Kimura, M. Niwano, Y. Ouchi, and K. Seki, *Phys. Status Solidi A*,**201**, 1075 (2004).

19) M. Hiramoto and K. Sakai, *Mol. Cryst. Liq. Cryst*., **491**, 284 (2008).

20) M. Hiramoto, *Proc. SPIE*, **7052**, 70520H (2008).

21) Y. Shinmura, T. Yoshioka, T. Kaji, and M. Hiramoto, *Appl. Phys. Express*, **7**, 071601 (2014).

22) H. Yoshida, Anal. Bioanal. Chem. **406**, 2231 (2014) and H. Yoshida (private communication).

23) H. Yoshida, *Chem. Phys. Lett*., **539**-**540**, 180 (2012).

24) H. Ishii, K. Sugiyama, E. Ito, and K. Seki, *Adv. Mater*., **11**, 605 (1999).

25) Ionization rates were calculated under the assumption that $FeCl_3$ formed a chemically stable dimer molecule ($Fe_2Cl_6$) and doped molecularly.

26) There is no sign of $Cs_2CO_3$ dissociation during vacuum evaporation since single $Cs_2CO_3$ film is completely transparent.

27) $\Delta E_D$= 0.12 eV is calculated from the ionization rate of 0.1 which is expressed by $\exp(-\Delta E_D/2kT)$.

28) $W_{dep}$ of the $H_2Pc$ side at $H_2Pc/C_{60}$ interface (3.3 nm) was obtained by $W_{dep} = (2\varepsilon\varepsilon_0 V_{bi}/eN)^{1/2}$ with carrier concentration (N) ($2.2 \times 10^{19}$ $cm^{-3}$) under 100% ionization and $V_{bi}$, i.e., the difference of $E_F$s between single $H_2Pc$ and $C_{60}$ (0.49 V).

29) For $C_{60}$:$H_2Pc$ (9:1), 100%$\times$0.9 + 10%$\times$0.1 = 91%.

30) R. Dingle, H. L. Stormer, A. C. Gossard, and W. Wiegmann, *Appl. Phys. Lett*., **33**, 665 (1978).

31) The radius of an electron orbital around a positively ionized donor can be calculated based on the equation expressing the Bohr radius (r) including the relative permittivity ($\varepsilon$), the effective mass of an electron ($m_n$*) and quantum number (n), *i.e.*, $r = \varepsilon\varepsilon_0 h^2 n^2/\pi m_n^* e^2$. Binding energy $\Delta E_D = m_n^* e^4/8\,\varepsilon^2\,\varepsilon_0^2 h^2\,(1/n^2)$. The observed $\Delta E_D$ of 0.12 eV is obtained for n = 3 (r = 1.6 nm).

32) [Relaxation energy (0.58 eV)] = [energy difference between LUMOs for $H_2Pc$ and $C_{60}$ (0.7 eV)] – [$\Delta E_D$ (0.12 eV)].

33) $\Delta E_D$ = 0.026 eV is obtained for n = 6 (r = 6.5 nm).

# Chapter 7:

## 7.1 Summary of This Thesis

Impurity doping to control the *pn*-junction characteristics is vital for increase in the photoconversion efficiency of organic solar cells. In order to design high-efficiency organic solar cells, the author has attempted to confirm whether or not this *pn*-control can be applied to any organic semiconductor, and to evaluate the carrier concentration in doped single and co-deposited organic semiconductor films.

Following effects arising from doping single and co-deposited organic semiconductor films have been revealed.

1) Organic semiconductors can, in general, be controlled to be *p*- or *n*-type, similar to inorganic semiconductors.
2) The doping efficiency in single $C_{60}$ film is extremely low due to the strong attractive force between the small electron orbital and the positively ionized donor.
3) Ionization sensitization attributable to the charge separation occurs in the co-deposited film.

The ionization sensitization is a new knowledge which gives meaning to doping to co-deposited films, and is a unique characteristic of organic semiconductors. It now has the potential for development into organic electronic devices.

# List of Publications

1) "*pn*-Control and *pn*-Homojunction Formation of Metal-free Phthalocyanine by Doping"

   **Yusuke Shinmura**, Masayuki Kubo, Norihiro Ishiyama, Toshihiko Kaji, and Masahiro Hiramoto, *AIP Adv*., **2**, 032145 (6 pages)(2012).

2) "Improved Photovoltaic Characteristics by $MoO_3$-doping to Thick Hole Transporting Films"

   **Yusuke Shinmura**, Masayuki Kubo, Toshihiko Kaji, and Masahiro Hiramoto, *Jpn. J. Appl. Phys*., **52**, 04CR12 (4 pages) (2013).

3) "Mapping of Band-Bending for Doped $C_{60}$ Films"

   **Yusuke Shinmura**, Tadashi Yoshioka, Toshihiko Kaji, and Masahiro Hiramoto, *Appl. Phys. Express.*, **7**, 071601 (4 pages) (2014).

4) "Ionization Sensitization of Doping in Co-deposited Organic Semiconductor Films"

   **Yusuke Shinmura**, Yohei Yamashina, Toshihiko Kaji, and Masahiro Hiramoto, *Appl. Phys. Lett.*, **105**, 183306 (5 pages) (2014).

## List of Supplementary Publications

5) “Invertible Organic Photovoltaic Cells with Heavily-doped Organic/Metal Ohmic Contacts”

   Masayuki Kubo, **Yusuke Shinmura**, Norihiro Ishiyama, Toshihiko Kaji, and Masahiro Hiramoto, *Appl. Phys. Express*, **5**, 092302 (3 pages) (2012).

6) “Junction Formation by Doping in $H_2Pc$:$C_{60}$ Co-evaporated Films for Solar Cell Application”

   Masayuki Kubo, **Yusuke Shinmura**, Norihiro Ishiyama, Toshihiko Kaji, and Masahiro Hiramoto, *Mol. Cryst. Liq. Cryst.*, **581**, 13-17 (2013).

7) “Bandgap Science for Organic Solar Cells”

   M. Hiramoto, M. Kubo, **Y. Shinmura**, N. Ishiyama, T. Kaji, K. Sakai, T. Ohno, and M. Izaki, *Electronics*, **3**, 351-380 (2014).

# Oral Presentations

## *International conferences*

1) "Improved Photovoltaic Characteristics by $MoO_3$-doping to Thick Hole Transporting Films"

   **Yusuke Shinmura**, Masayuki Kubo, Toshihiko Kaji, Masahiro Hirmaoto, International Conference on Solid State Devices and Materials, Kyoto, Japan, 2012/9/25-27.

2) "Quantification of Junction Parameters of Doped Codeposited Organic Semiconductors"

   **Yusuke Shinmura**, Masayuki Kubo, Toshihiko Kaji, Masahiro Hirmaoto, The 40th International Symposium on Compound Semiconductors, Kobe, Japan, 2013/5/20-21.

## *Domestic conferences (in Japanese)*

1) "Photo-electric Conversion Characteristics of $C_{60}$ single crystals"

   **Yusuke Shinmura**, Toshihiko Kaji, Kai Iketaki, Masahiro Hiramoto, The 71st The Japan Society of Applied Physics Autumn Meeting (15a-R-3), Nagasaki University, Nagasaki, Japan, 2010/9/13-17 (Sept. 15).

2) "$MoO_3$-doping to Hole Transporting Materials and Photovoltaic Characteristics"

   **Yusuke Shinmura**, Masayuki Kubo, Toshihiko Kaji, Masahiro Hiramoto, The 72nd The Japan Society of Applied Physics Autumn Meeting (1a-L-10), Yamagata University, Yamagata, Japan, 2011/8/29-9/2 (Sept. 1).

3) “*pn*-Homojunction Formation in Phthalocyanine Film by Doping”

**Yusuke Shinmura**, Masayuki Kubo, Toshihiko Kaji, Masahiro Hiramoto, The 59th The Japan Society of Applied Physics Spring Meeting (16p-F7-1), Waseda University, Tokyo, Japan, 2012/3/15-18 (Mar. 16).

4) “Quantification of Carrier Concentration and Mobility for Doped Co-deposited Organic Semiconductor Films”

**Yusuke Shinmura**, Masayuki Kubo, Toshihiko Kaji, Masahiro Hiramoto, The 60th The Japan Society of Applied Physics Spring Meeting (27p-G18-8), Kanagawa Institute of Technology, Kanagawa, Japan, 2013/3/27-30 (Mar. 27).

5) “Sensitization of Ionization Rate by Doping for Co-deposited Films”

**Yusuke Shinmura**, Yohei Yamashina, Toshihiko Kaji, Masahiro Hiramoto, The 74th The Japan Society of Applied Physics Autumn Meeting (18p-C16-4), Doshisya University, Kyoto, Japan, 2013/9/16-20 (Sept. 18).

6) “Relationship between Cell Thickness and Electron Mobility”

**Yusuke Shinmura**, Yohei Yamashina, Toshihiko Kaji, Takahiro Kono, Yuji Yoshida, Masahiro Hiramoto, The 61st The Japan Society of Applied Physics Spring Meeting (19p-E9-6), Aoyama Gakuin University, Kanagawa, Japan, 2014/3/17-20 (Mar. 19).

## Poster Presentations

### *International conferences*

1) “Improved Photovoltaic Characteristics by $MoO_3$-doping to Thick Hole Transporting Films”

   **Yusuke Shinmura**, Masayuki Kubo, Toshihiko Kaji, Masahiro Hirmaoto, Materials Research Society Spring Meeting, San Francisco, USA, 2012/4/10-15

2) “Sensitization of Doping in Organic Co-deposited Films”

   **Yusuke Shinmura**, Yohei Yamashina, Toshihiko Kaji, Masahiro Hirmaoto, The 6th World Conference on Photovoltaic Energy Conversion, Kyoto, Japan, 2014/11/23-27 (Nov. 26).

### *Domestic conferences (in Japanese)*

1) “Sensitization of Ionization Rate of Doping in Organic Semiconductors”

   **Yusuke Shinmura**, Yohei Yamashina, Toshihiko Kaji, Masahiro Hiramoto, The 75th The Japan Society of Applied Physics Autumn Meeting (17a-PA2-9), Hokkaido University, Hokkaido, Japan, 2014/9/17-20 (Sept. 17).

## List of Books (in Japanese)

“Formation of pn-homojunction for single phthalocyanine film” Masahiro Hiramoto, **Yusuke Shinmura**, O plus E, Vol.35, No.4, 2013, pp.413-417 (Advanced Communication Media Co., Ltd.)

## Acknowledgement

I greatly appreciate to Professor Masahiro Hiramoto at the Institute for Molecular Science, National Institute of Natural Science for a lot of meaningful discussions, advices, and teaching. I learned a lot of things from his enthusiastic attitude to study.

I express my sincere gratitude to Prof. Satoshi Kera, Associate Prof. Toshiyasu Suzuki, Associate Prof. Donglin Jiang at The Graduated University for Advanced Studies, and Ph.D. Yuji Yoshida at Advanced Industrial Science and Technology (AIST) for the review of this thesis.

I gratefully appreciate Dr. Yuji Yoshida and his group researchers at AIST, and Prof. Masanobu Izaki and his group researchers at Toyohashi University of Technology for helpful discussions in the Core Research for Evolutional Science and Technology (CREST) project work.

I would like to thanks our group member; Assistant Prof. Toshihiko Kaji, Mr. Masayuki Kubo, Mr. Kazuya Yokoyama, Mr. Tadashi Yoshioka, Mr. Yohei Yamashina, Mr. Mitsuru Kikuchi, Mr. Kenichi Abe, Ms. Chika Ohashi, Mr. Mikimasa Katayama and Ms. Hidemi Sugihara, for helpful discussion, a lot of advices, and encouragement.

I gratefully appreciate to WORLD INTEC CO., LTD. for a lot of supports.

Financial support from Core Research for Evolutional Science and Technology (CREST) of the Japan Science and Technology Agency (JST) is gratefully acknowledged.

Finally, I would like to express my sincere gratitude to everyone contributed to this my study.